

UNIVERSITY OF GENOA
POLYTECHNIC SCHOOL

DICCA

Department of Civil, Chemical and Environmental Engineering



MASTER OF SCIENCE THESIS

IN

CHEMICAL ENGINEERING

**Microparticle production by spray dryer and
validation with CFD simulation**

SUPERVISORS:

Chiar.^{ma} Prof. Ing. Patrizia Perego

Chiar.^{mo} Prof. Ing. Jan Oscar Pralits

CO SUPERVISORS:

Dott.ssa Ing. Margherita Pettinato

Dott. Alessandro Alberto Casazza

Dott. Ing. Matteo Colli

Marco Atzori (KTH-Royal Institute of Technology)

CANDIDATE:

Emanuela Drago

ACADEMIC YEAR 2017-2018

Abstract

The work presented in this thesis is integrated in a well started project that Dott. Ing. Giovanni Beati presented as his master thesis. His work concerned the implementation of a Lagrangian solver in OPENFOAM[®] that is able to consider the liquid phase as well as the solid phase in a two stage drying model using a simplified geometry. The aim of this project has been to use this Lagrangian solver in OPENFOAM[®], to model the kinetics of drying liquid drops containing insoluble solids and soluble ones, re-adapting it to the real geometry of the Spray Dryer used for the experimental tests, present in the laboratory of the University of Genoa (DICCA). The main assumptions for the first stage of the drying is that the mixing inside the drop is considered to be ideal without re-circulation, and the critical moisture content is evaluated through a simplified approach based on a critical averaged solid-liquid ratio. A simplified model of the second drying stage has been also used, when the critical moisture content is reached, the drop is considered to be completely solid and the wet core is neglected. Simulations for mixtures with calcium carbonate suspensions, as well as maltodextrin solutions were carried out by varying the feed flow rate and solid concentration; the two parameters found most significant during the laboratory tests. The resulting mass flow rate from numerical simulations and experiments were of the same order of magnitude. From the numerical simulations detailed results were obtained, for the first time ever, regarding the turbulent flow structures, the temperature field and the particle temperature, diameter and age, all as a function of space and time.

Acknowledgements

I would really like to thank my relators, Prof. Patrizia Perego and Prof. Jan Oscar Pralits, for proposing this thesis and making me discover a very interesting field. I thank them for following me to the last and always advised me in the best way what to do. I would also to thank Matteo Colli and Marco Atzori for all the help they gave me right away despite all their commitments. I thank Matteo for introducing me to the world of OpenFOAM and providing me with all the necessary material. I thank Marco who despite being in Sweden has always been available for Skype calls and for have helping me on his rare days back home. A big thank you goes to Margherita Pettinato and Alessandro Alberto Casazza who taught me so much. There are no words to describe the kind of help that came from my family. My mother, my father, my brother and my grandparents always gave me support during this long period of studies where there were very difficult moments and without them I would not be able to overcome. Last but not least I have to thank Jacopo. I am sure that without his presence everything would have been much less tolerable. I also have to thank him for having endured me for all this time, alone it would have been much more difficult.

We have obtained part of the results presented in this thesis by employing resources of the KTH - Royal Institute of Technology (Stockholm, Sweden), in particular, the computational time provided by Swedish National Infrastructure for Computing (SNIC), allocation SNIC 2017/12-20. We gratefully acknowledge Prof. Philipp Schlatter for this opportunity.

Contents

1	Introduction	1
2	Description of a Spray Dryer	3
2.1	Stages of spray drying	4
2.1.1	Atomisation	4
2.1.2	Drying chamber	7
2.1.3	Separation of dried product	8
2.2	Types of spray dryer	9
2.3	Spray drying parameters	9
3	Fundamental concepts in fluid mechanics	12
3.1	Conservation laws	12
3.1.1	Continuity equation	12
3.1.2	Conservation of Linear Momentum	13
3.1.3	Conservation of Energy	14
3.2	Turbulence modelling	17
3.2.1	General principles	20
3.2.2	Smagorinsky closure	24
3.2.3	Spallart-Allmaras equation models	25
3.3	Near the wall treatment	28
3.4	Flow with particles	30
3.4.1	Particle equations	31
3.4.2	Kinetic of drying process	32
3.4.3	Mass transfer: diffusion and convection	33

3.4.4	Heat transfer: diffusion and convection	36
3.4.5	Two-stage evaporation model	38
3.4.6	First stage	39
3.4.7	Second stage	42
4	Numerical modeling with OpenFOAM	44
4.1	About OpenFOAM	44
4.2	OpenFOAM case structure	46
4.3	Simulation workflow: global view	47
4.3.1	Mesh generation	47
4.3.2	Mesh quality assessment	48
4.3.3	Standard solvers	49
4.3.4	Post-Processing	52
5	Methods and equipments	53
5.1	Design of Experiments	53
5.2	Spray drying procedure	58
5.3	Product recovery	59
5.4	Moisture measurement	59
5.5	Particle size distribution	60
6	Case Study	62
6.1	Geometry	62
6.2	Case with only the flow	65
6.3	Particle implementation in OpenFOAM	71
6.3.1	Background fluid flow field	71
6.3.2	OpenFOAM solver: <i>ReactingParcelFoam</i>	72
6.3.3	<i>MA_BuoyantKinematicParcelFoam</i>	73
7	Results	76
7.1	Design of Experiment Results	76
7.1.1	Optimization tests Results	109
7.2	Flow case	112

7.3 Particle flow	116
7.4 Comparison with experimental data	127
Conclusions and Future Developments	132

Chapter 1

Introduction

The topic of this thesis concerns the area of spray drying which is one of the oldest and most common methods used for the production of a large variety of particulate products in the chemical, food, household products and pharmaceutical industries. It involves drying of droplets of a fluid feedstock into particles by a hot gaseous medium. The aim of spray drying process is to produce dried powder of required characteristics (size distribution, moisture content etc.). Operating and design parameters can be varied to determine the optimum conditions for the desired product. This is carried out mainly by expensive and time consuming experimental investigations. Mathematical modelling of spray drying process can reduce the time and costs associated with the determination of optimized parameters. The complexity of gas flows patterns and interacting transport processes in spray dryer poses challenges in the modeling of spray dryers. The trajectories and hence the residence times of the particles in the drying chamber are dependent on the gas flow patterns, therefore it is important to have a reliable prediction of gas flow profiles [41] [35]. Computational Fluid Dynamics (CFD) is considered as the perfect choice to model the spray drying process. In particular this work is using a recent implementation of a two stage drying model for liquid droplets containing insoluble solids and on the comparison with experimental data obtained in laboratory. This model has been implemented in OPENFOAM[®], a CFD open-source software. A number of studies have been published in the recent decades utilizing CFD for modeling spray dryers. In most cases the spray dryer modelling is performed using a mixed

Eulerian/Lagrangian approach, in which the single phase Reynolds Averaged Navier Stokes (RANS) or Unsteady Reynolds Averaged Navier-Stokes (URANS) equations are solved to determine the flowfield and the droplets are modelled using the Lagrangian technique [16]. A large amount of literature exists about this topic, and very detailed studies have been carried out by many research groups. For example in [24] and in [26] it is presented a study of the air flow inside a tall form spray dryer, including the effect of different turbulence models and their influence on particle trajectories and their residence time; in [28] there are studies on the interaction of droplets with the spray dryer walls, modelling the rebound as a function of droplets moisture content; also particles agglomeration can be important and it determines the character of the final product as well described in [16]; moreover in [34], [32], [30], [31] the description of accurate drying models are found both for insoluble or dissolved solids with particular attention paid on the second stage, that is the one related to the formation of a solid shell around a wet core. Computational Fluid Dynamics analysis involves following three main steps. The first step is Pre-Processing, which includes problem definition, geometry, meshing and generation of a computational model. The second step is Processing, which uses a computer to solve the mathematical equations of the fluid flow. The final step of Post-Processing is used to evaluate and visualize the data generated by the CFD analysis and validate the simulation results with experimental data [3]. Although the origin of CFD can be found in many industries, it is only in the recent years that CFD has been applied to the food processing area. The ability of CFD to predict the performance of new designs or processes before they are ever manufactured or implemented make them an integral part of engineering design and analysis [40]. Our goal has been to use the Lagrangian solver in OPENFOAM[®], implemented in the previous thesis of Giovanni Beati at the University of Genoa, to model the kinetics of drying liquid drops containing insoluble solids, re-adapting it to the real geometry of the Spray Dryer used for the experimental tests, present in the laboratory of the University of Genoa (DICCA). Experimental tests were initially carried out which were used to collect data to be included in the model and thanks to which it was possible to see which quantities could still be used to improve the model.

Chapter 2

Description of a Spray Dryer

Spray drying is a well-established method, used to convert a liquid feed, usually solution, emulsion or suspension, into a dry powder form by spraying the feed into a hot gas medium, generally air or nitrogen [4]. Used since the late 1850s in the dairy industry, this technology is used today in many sectors, from food industry to the agro-chemical, biotechnology, heavy and fine chemicals, mining, metallurgical and also pharmaceutical sector [49]. Normally, the spray dryer is located at the end-point of the processing line, as it is an important stage for controlling the final product quality. It has advantages such as fast drying rates, a wide range of operating temperatures and short residence times [4] [6]. Furthermore, the spray dryer has the great advantage of being suitable for the treatment of heat-sensitive materials, thanks to the short contact time. Therefore the product can be dried without any loss or alteration of the volatile compounds of the product (proteins, vitamins, organoleptic characteristics). In this regard, spray drying helps to preserve the product, guaranteeing stability and an extended shelf life by reducing the moisture content to levels where microbiological growth is not possible. In addition to this, the spray dryer is able to handle materials in aseptic and hygienic drying condition which makes it applicable in the pharmaceutical industry. It has also demonstrated its value in the protection of the environment as it is able to evaporate organic solvents that are potentially explosive or toxic. Thus, spray dryers have a wide variety of industrial and commercial uses [41].

2.1 Stages of spray drying

As shown in Fig.2.1, the spray drying process can be divided into three operating phases: (1) atomisation of the liquid feed in a spray chamber, (2) contact between the spray and the drying medium, stage in which the solvent evaporates, and (3) separation of the dried products from air flow [3]. The choice of spray drying configuration, which includes the design of the drying chamber, the atomizer, the air flow characteristics, affects the size of the product and how the product reacts to the existing temperature and humidity profiles in the dryer due to the selected operating conditions. In addition to the design of the spray dryer and its equipment, the chemical composition of the solid affects the shape of the particles [41].

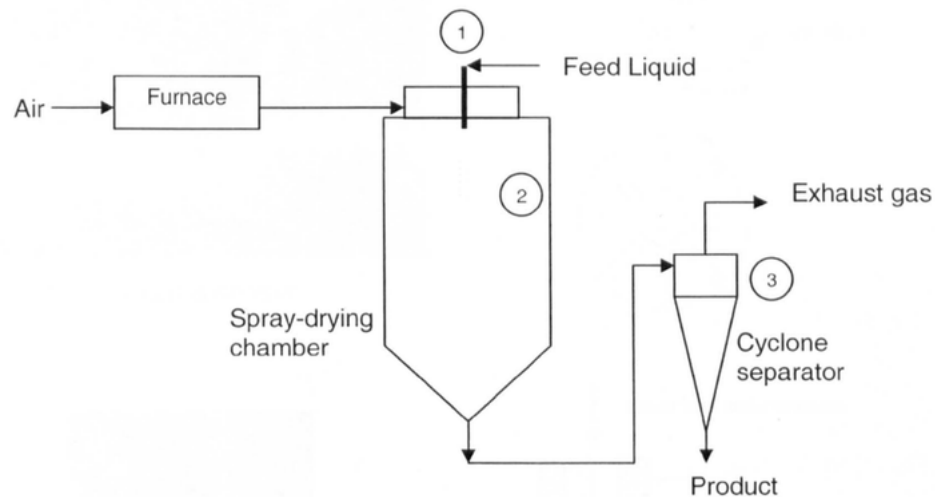


Figure 2.1: *The process stages of spray drying [4].*

2.1.1 Atomisation

At the first stage the feed is pumped from the tank to the atomizer. Atomisation is a process in which the feed liquid breaks up into a large number of small drops to form a spray for action of the air flow that impacts on the liquid feed flow. The atomizer is the most important equipment in the spray drying process, and it is located at the ceiling of the chamber. The main functions of the atomizer are to create a high surface to mass ratio to facilitate evaporation and to produce

particles with the desired shape, size and density [49]. The choice of atomizer is very important to obtain an economic production of high quality products [20]. There are several types of atomizers that can be used in spray drying processes:

Centrifugal atomizer: the liquid is fed into the centre of a rotating wheel with a peripheral speed of 90-200 m/s. The droplets produced are typically in the range of 30-120 μm . The size of droplets produced by the nozzle varies directly with feed rate and feed viscosity and inversely with wheel speed and wheel diameter, as seen in Fig.2.2 [3]. The main advantage of the centrifugal atomizer is the ability to produce an homogeneous spray and the desired droplet size can be obtained by adjusting wheel speed. However, the operational costs are high compared to the other atomizers. They are not suitable for the atomisation of highly viscous materials [49].

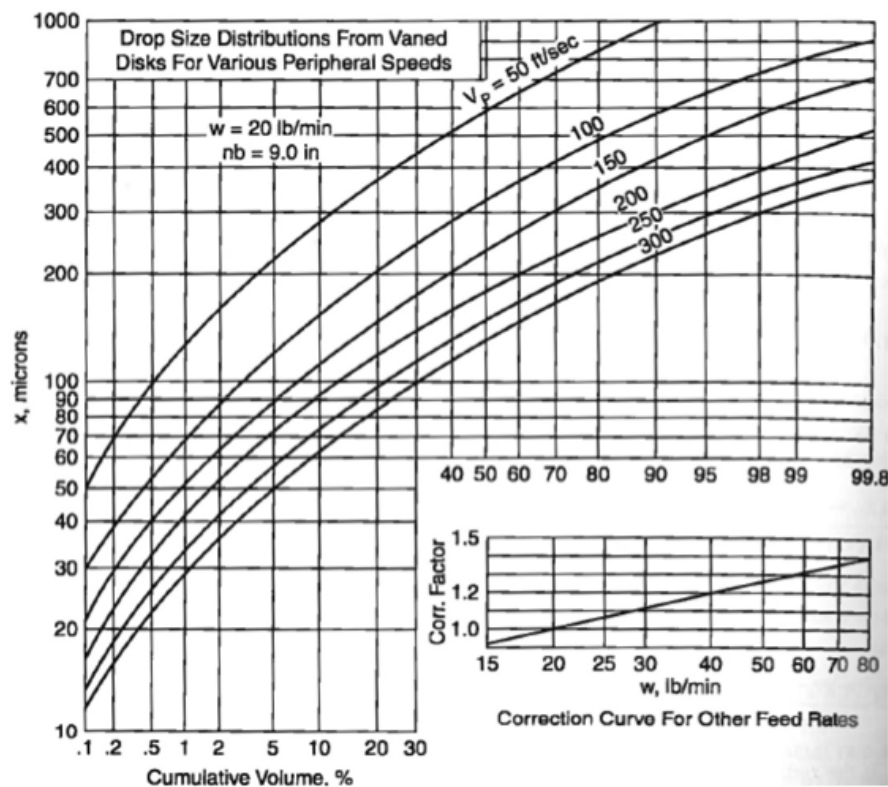


Figure 2.2: Droplet size as a function of peripheral speed of a centrifugal atomizer [23].

Pressure nozzle atomizer: the liquid is forced to pass through a small nozzle for high pressure (700-2000 kPa). Here the droplets size is typically in the range of 120-250 μm .

The size of the droplet produced by the nozzle varies directly with feed rate and feed viscosity and inversely with pressure [3]. This type of atomizer is the most used in the industry. Operating costs are lower than the other atomizers. They are also simple, easy to construct and flexible [49].

Two-fluid nozzle atomizer: liquid flow and compressed air flow are forced through a small nozzle. The operating pressure is lower than pressure nozzle atomizer one (10-200 kPa). Also in this case, as shown in Fig.2.3, the size of the drops is a function of pressure. These types of nozzles are able to atomize highly viscous fluids to produce fine particles [49].

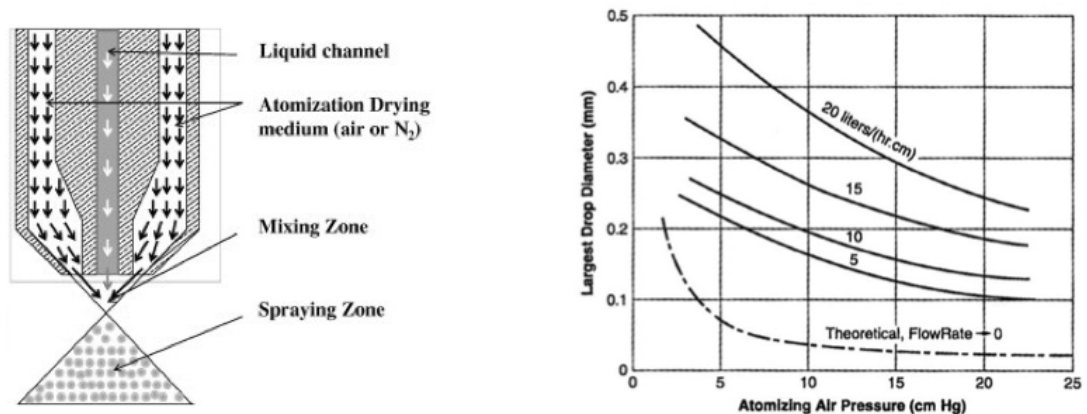
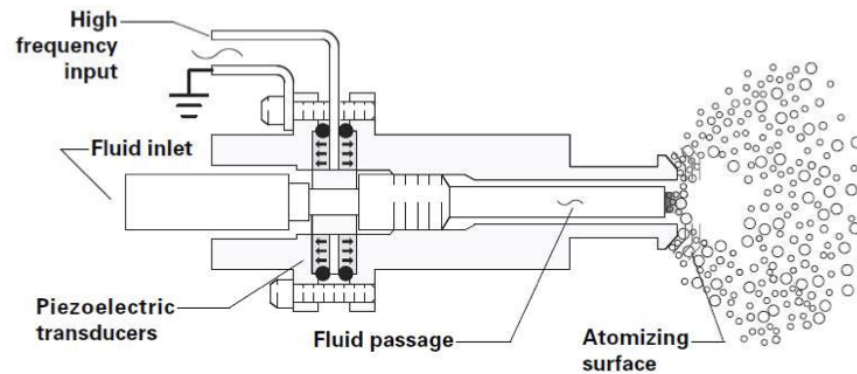
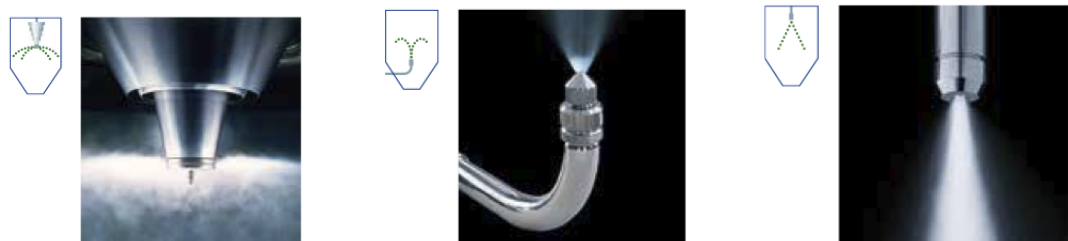


Figure 2.3: *Droplet size as a function of pressure in a two-fluid nozzle atomizer [23].*

Ultrasonic atomizer: conventional atomizers are not suitable to atomize highly viscous, non-Newtonian and long molecular chain liquids. Some of these liquids form filaments instead of spherical droplets when conventional atomizers are used. Recent studies show that ultrasonic energy and vibration obtained from a sonic resonance cup placed in front of the nozzle can be used to disintegrate highly viscous liquids and obtain droplets of desired size. Ultrasonic atomizer can be used to produce fine droplets below $50\ \mu\text{m}$. The commercial application of ultrasonic atomizers is still limited [49]. The operating scheme of an ultrasonic atomizer is shown in Fig.2.4. While Fig.2.5 shows examples of the shape of the injection cones.

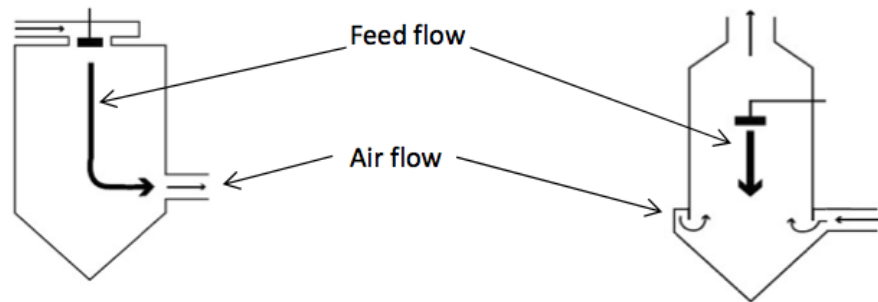
Figure 2.4: *Ultrasonic atomizer [23].*Figure 2.5: *Examples of centrifugal atomizer, pressure nozzle and two-fluid nozzle [18].*

2.1.2 Drying chamber

During spray-air contact, the hot drying gas can be blown in the same direction as the sprayed liquid: co-current flow, or it can be against the flow from the atomizer: counter-current flow Fig.2.6. With the co-current configuration, hot air and droplets are in contact from the beginning of the injection and, due to the high evaporation rate, their temperature is kept low. Along the chamber, the moisture content of the droplets decreases and also the air temperature, which results in a lower heat transfer rate from the continuous phase to the dried particles. In the counter-current, however, the spray inlet corresponds to the drying medium outlet and this causes a temperature of the final product higher than the temperature of the drying agent and that is why this configuration is used only for non heat-sensitive products [4]. Table 2.1 shows the main advantages and disadvantages of the two configurations.

Table 2.1: *Co-current VS Counter-current.*

	Co-current	Counter-current
Advantages	Ideal for thermolabile compounds Lower time in the chamber Easier product recovery	Higher time in the chamber Lower moisture content
Disadvantages	Problem with sticky product	Problems with thermolabile compounds Difficult product recovery, lower yield

Figure 2.6: *Schematic description of co-current and counter-current dryer [23].*

In the drying chamber there is a multiphase flow with heat transfer, mass and momentum between the drying gas flow (continuous phase) and the discrete phase comprising poly-disperse droplets/particles. Furthermore, there is interaction between the droplet/particles, resulting in coalescence, agglomeration and rupture, as well as droplets/particle interaction and wall with subsequent deposition on the walls, re-entrainment of the deposited material and breakage of the particles [35].

2.1.3 Separation of dried product

The powder produced is collected at the base of the chamber and removed by a screw conveyor or a cyclone separator. Other methods for collecting the dried product are bag filters or electrostatic precipitators [20]. The choice of the equipment

depends on the operating conditions such as particle size, shape, density and powder outlet position.

2.2 Types of spray dryer

The two main designs of spray dryer commonly used are the short-form and tall-form dryers shown in Fig.2.7:

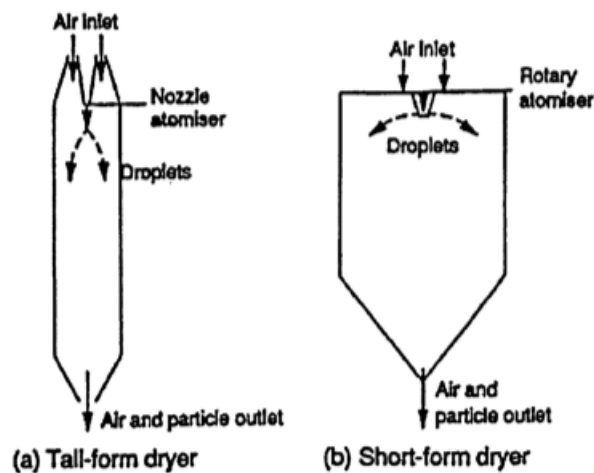


Figure 2.7: Schematic description of main types of spray dryers [13].

Short-form dryers are characterized by a restrained aspect ratio meaning that the height-diameter ratio is of around 2:1 while tall-form dryers have a height-diameter ratio greater than 5:1. In the latter case dryers have less complex flow patterns than short-form dryers, but they are afflicted by an higher percentage of particles impacting on the cylindrical wall which is a negative effect on the final product quality [4].

2.3 Spray drying parameters

Important parameters in the drying process are:

- Inlet Temperature: can be directly controlled. Low inlet temperature causes high water content, poor fluidity and easiness of agglomeration. While high

inlet temperature causes cracks in the membrane inducing premature release and degradation of encapsulated ingredients.

- Outlet Temperature: cannot be directly controlled. It depends on the inlet temperature, hot air flow, feed flow, feed solution concentration. It can be considered as the control index of the process, in particular for reproducibility.
- Feed solution viscosity: high viscosities interfere with the atomization process and lead to the formation of aggregates that adversely affect the drying rate. Viscosity is influenced by feed solution concentration and feed solution temperature.
- Hot air flow: high air flow means a higher degree of separation in the cyclone; low air flow means lower moisture content in the product.
- Feed flow: is controlled by a peristaltic pump. The higher the feed flow, the higher the energy required for drying: this means lower outlet temperature. High feed flow results in high moisture content. This parameter is also influenced by the feed solution concentration.
- Feed solution concentration: low concentration results in smaller particle size. Feed solution concentration also affects the viscosity of the feed solution.

Finally, Table 2.2 shows the dependence of the operating parameters of the spray drying process from outlet temperature, particle size, product moisture and yield.

Table 2.2: Dependence of operating parameters of the process [8].

Parameter	Dependence	Aspirator rate ↑	Air humidity ↑	Inlet temperature ↑	Spray air flow ↑	Feed rate ↑	Concentration ↑
Outlet temperature		↑↑less heat losses based on total inlet of energy	↑more energy stored in humidity	↑↑↑direct proportion	↓more cool air to be evaporated	↓↓more solvent to be evaporated	↑↑less water to be evaporated
Particle size		-	-	-	↓↓↓more energy for fluid dispersion	(↑) more fluid to disperse	↑↑↑more remaining product
Final humidity of product		↑↑lower partial pressure of evaporated water	↑↑higher partial pressure of drying air	↓↓lower relative humidity in air	-	↑↑more water leads to higher particle pressure	↓less water evaporated, lower partial pressure
Yield		↑↑better separation rate in cyclone	(↓) more humidity can lead to sticking product	(↑) eventually dryer product prevent sticking	-	(↑↓) depends on application	↑bigger particles lead to higher separation

Chapter 3

Fundamental concepts in fluid mechanics

3.1 Conservation laws

In a closed system quantities such as mass, momentum and energy are conserved. The governing equations that describe the dynamic of a fluid system (called Navier-Stokes equations) are the differential form of such conservation laws [19]. Conservation laws involving fluid flow and related transport phenomena can be mathematically formulated via a Lagrangian approach (material volume, MV) or an Eulerian approach (control volume, CV). Assuming a continuous phase, the most common method to describe the fluid flow is the fixed reference system Eulerian approach which is briefly presented below. A short description of the Lagrangian method will be introduced in the next section.

3.1.1 Continuity equation

The principle of conservation of mass indicates that, in the absence of mass sources and sinks, a region will conserve its mass on a local level [19]. Being ρ the density, by the application of the Reynolds transport theorem, the general expression for conservation of mass as applied to a control volume will be:

$$\int_V \frac{\partial \rho}{\partial t} dV + \int_S \rho \mathbf{v} \cdot \mathbf{n} dS = 0 \quad (3.1)$$

where S is the surface of the control volume V . Thanks to the divergence theorem – and noticing that the conservation of mass should be respected for every control volume – this equation can be written in a differential form, called the continuity equation:

$$\frac{\partial \rho}{\partial t} + \nabla \cdot (\rho \mathbf{v}) = 0 \quad (3.2)$$

3.1.2 Conservation of Linear Momentum

Through application of the Reynolds transport theorem and divergence theorem, the general expression for conservation of linear momentum as applied to a control volume is:

$$\frac{\partial(\rho \mathbf{v})}{\partial t} + \nabla \cdot (\rho \mathbf{V} \mathbf{v}) = \mathbf{f} \quad (3.3)$$

Where $\mathbf{f} = \mathbf{f}_s + \mathbf{f}_b$ is the sum of the external surface forces \mathbf{f}_s and body forces \mathbf{f}_b acting on the control volume.

Surface forces

The forces acting on the control volume surface are due to pressure and viscous stresses which can be expressed in terms of the total stress tensor $\boldsymbol{\sigma}$ that in Cartesian coordinates is given by:

$$\boldsymbol{\sigma} = \begin{pmatrix} \sigma_{xx} & \tau_{xy} & \tau_{xz} \\ \tau_{yx} & \sigma_{yy} & \tau_{yz} \\ \tau_{zx} & \tau_{zy} & \sigma_{zz} \end{pmatrix} = \begin{pmatrix} -P & 0 & 0 \\ 0 & -P & 0 \\ 0 & 0 & -P \end{pmatrix} + \begin{pmatrix} \tau_{xx} & \tau_{xy} & \tau_{xz} \\ \tau_{yx} & \tau_{yy} & \tau_{yz} \\ \tau_{zx} & \tau_{zy} & \tau_{zz} \end{pmatrix} = -p\mathbf{I} + \boldsymbol{\tau} \quad (3.4)$$

where \mathbf{I} is the identity tensor, p the pressure and $\boldsymbol{\tau}$ is the deviatoric stress tensor. The pressure is the negative part of the mean of the normal stresses and is given by:

$$p = -\frac{1}{3}(\sigma_{xx} + \sigma_{yy} + \sigma_{zz}) \quad (3.5)$$

Hence the surface force acting on a differential surface element dS is:

$$\int_S \mathbf{f}_s dS = \int_A \boldsymbol{\sigma} \cdot \mathbf{n} dA = \int_V \nabla \cdot \boldsymbol{\sigma} dV \Rightarrow \mathbf{f}_s = \nabla \cdot \boldsymbol{\sigma} = -\nabla p + (\nabla \cdot \boldsymbol{\tau}) \quad (3.6)$$

Body forces

Body forces are forces per unit volume and the predominant ones are given below:

- Gravitational forces $\mathbf{f}_b = \rho\mathbf{g}$, due to the presence of a gravitational field.
- Coriolis and centrifugal forces, respectively $\mathbf{f}_b = -2\rho(\boldsymbol{\omega} \times \mathbf{v}) - \rho(\boldsymbol{\omega} \times (\boldsymbol{\omega} \times \mathbf{r}))$, due to a rotating frame of reference.

Hence introducing the expressions of surface and body forces in Eq.(3.3) the general conservative form of the momentum equation is obtained as:

$$\frac{\partial(\rho\mathbf{v})}{\partial t} + \nabla \cdot (\rho\mathbf{v}\mathbf{v}) = -\nabla p + (\nabla \cdot \boldsymbol{\tau}) + \mathbf{f}_b \quad (3.7)$$

To proceed further the type of fluid should be specified in order to relate $\boldsymbol{\tau}$ with the other flow variables. For a Newtonian fluid the stress tensor is a linear function of the strain rate and is given by:

$$\boldsymbol{\tau} = \mu(\nabla\mathbf{v} + (\nabla\mathbf{v})^T) + \lambda(\nabla \cdot \mathbf{v})\mathbf{I} \quad (3.8)$$

where μ is the molecular viscosity, λ the bulk viscosity coefficient usually set equal to $\lambda = \frac{2}{3}\mu$. Taking the divergence of Eq.(3.8) and substituting in Eq.(3.7) the final conservative form of the momentum equation for Newtonian fluids becomes:

$$\frac{\partial(\rho\mathbf{v})}{\partial t} + \nabla \cdot (\rho\mathbf{v}\mathbf{v}) = \nabla \cdot (\mu\nabla\mathbf{v}) - \nabla p + \nabla \cdot (\mu(\nabla\mathbf{v}^T)) + \nabla(\lambda\nabla \cdot \mathbf{v}) + \mathbf{f}_b \quad (3.9)$$

For incompressible flows the divergence of velocity vector is zero, $\nabla \cdot \mathbf{v} = 0$, and for constant molecular viscosity the momentum equation can be further simplified:

$$\frac{\partial(\rho\mathbf{v})}{\partial t} + \nabla \cdot (\rho\mathbf{v}\mathbf{v}) = -\nabla p + \mu\nabla^2\mathbf{v} + \mathbf{f}_b \quad (3.10)$$

3.1.3 Conservation of Energy

The conservation of energy (the first law of thermodynamics) states that energy can be neither created nor destroyed during a process; it can only change from one form (mechanical, kinetic, chemical, etc.) into another one. Consequently, the sum of all forms of energy in an isolated system remains constant. Considering a material

volume MV of mass m , density ρ , and moving with a velocity \mathbf{v} the total energy E can be written as:

$$E = m(\hat{u} + \frac{1}{2}\mathbf{v} \cdot \mathbf{v}) \quad (3.11)$$

where \hat{u} is the internal energy per unit mass. The first law of thermodynamic states that the rate of change of the total energy of the material volume is equal to the rate of heat addition and work extraction through its boundaries:

$$\left(\frac{dE}{dt}\right)_{MV} = \dot{Q} - \dot{W} \quad (3.12)$$

Defining $e = \hat{u} + \frac{1}{2}\mathbf{v} \cdot \mathbf{v}$ as the total energy per unit mass and considering that:

$$\dot{W} = \dot{W}_s + \dot{W}_b \quad (3.13)$$

$$\dot{W}_s = - \int_S (\mathbf{f}_s \cdot \mathbf{v}) dS = - \int_S (\boldsymbol{\sigma} \cdot \mathbf{v}) \cdot \mathbf{n} dS = - \int_V -\nabla \cdot (p\mathbf{v}) + \nabla \cdot (\boldsymbol{\tau} \cdot \mathbf{v}) dV \quad (3.14)$$

$$\dot{W}_b = - \int_V (\mathbf{f}_b \cdot \mathbf{v}) \quad (3.15)$$

$$\dot{Q} = \dot{Q}_s + \dot{Q}_v \quad (3.16)$$

$$\dot{Q}_s = - \int_S \dot{q}_s \cdot \mathbf{n} dS = - \int_V \nabla \cdot \dot{q}_s dV \quad (3.17)$$

$$\dot{Q}_v = \int_V \dot{q}_v dV \quad (3.18)$$

Using the Reynolds transport theorem Eq.(3.12) becomes:

$$\begin{aligned} \left(\frac{dE}{dt}\right)_{MV} &= \dot{Q} - \dot{W} = \int_V \left(\frac{\partial}{\partial t}(\rho e) + \nabla \cdot (\rho \mathbf{v} e) \right) dV = \\ &= - \int_V \nabla \cdot \dot{q}_s dV + \int_V -\nabla \cdot (p\mathbf{v}) + \nabla \cdot (\boldsymbol{\tau} \cdot \mathbf{v}) dV + \int_V (\mathbf{f}_b \cdot \mathbf{v}) dV + \int_V \dot{q}_v dV \end{aligned} \quad (3.19)$$

Collecting terms within the volume integral and setting the integrand equal to zero gives:

$$\frac{\partial}{\partial t}(\rho e) + \nabla \cdot (\rho \mathbf{v} e) = -\nabla \cdot \dot{q}_s - \nabla \cdot (p\mathbf{v}) + \nabla \cdot (\boldsymbol{\tau} \cdot \mathbf{v}) + \mathbf{f}_b \cdot \mathbf{v} + \dot{q}_v \quad (3.20)$$

In order to write the energy equation with temperature as the main variable some constraints have to be imposed [19]. Denoting with h the specific enthalpy and assuming a Newtonian fluid it's possible to express $h = f(p, T)$ the variation of enthalpy dh can be written as:

$$dh = \left(\frac{\partial h}{\partial T}\right)_p dT + \left(\frac{\partial h}{\partial p}\right)_T dp \quad (3.21)$$

Using the thermodynamic relation:

$$\left(\frac{\partial h}{\partial p}\right)_T = v - T\left(\frac{\partial v}{\partial T}\right)_p \quad (3.22)$$

where v is the specific volume, the expression for dh can be modified to

$$dh = c_p dT + \left[v - T\left(\frac{\partial v}{\partial T}\right)_p\right] dp \quad (3.23)$$

After some manipulation, in order to express Eq.(3.20) in terms of specific enthalpy h and introducing Eq.(3.23), the energy equation with T as the main variable can be written as:

$$c_p \left[\frac{\partial}{\partial t}(\rho T) + \nabla \cdot (\rho \mathbf{v} T) \right] = -\nabla \cdot \dot{q}_s - \left(\frac{\partial(\ln \rho)}{\partial(\ln T)}\right)_p \frac{Dp}{Dt} + (\boldsymbol{\tau} : \nabla \mathbf{v}) + \dot{q}_v \quad (3.24)$$

The heat flux $\nabla \cdot \dot{q}_s$ represents heat transfer by diffusion, which is a phenomenon occurring at the molecular level and is governed by Fourier's law according to:

$$\dot{q}_s = -(k \nabla T) \quad (3.25)$$

where \ln is the natural logarithm and k is the thermal conductivity of the substance. The above equation states that heat flows in the direction of temperature gradient and assumes that the material has no preferred direction for heat transfer with the same thermal conductivity in all directions (the medium is isotropic). Introducing Eq.(3.25) in Eq.(3.24), defining Ψ and Φ as:

$$\Psi = \left(\frac{\partial u}{\partial x} + \frac{\partial v}{\partial y} + \frac{\partial w}{\partial z}\right)^2 \quad (3.26)$$

$$\Phi = 2 \left[\left(\frac{\partial u}{\partial x}\right)^2 + \left(\frac{\partial v}{\partial y}\right)^2 + \left(\frac{\partial w}{\partial z}\right)^2 \right] + \left(\frac{\partial u}{\partial y} + \frac{\partial v}{\partial x}\right)^2 + \left(\frac{\partial u}{\partial z} + \frac{\partial w}{\partial x}\right)^2 + \left(\frac{\partial v}{\partial z} + \frac{\partial w}{\partial y}\right)^2 \quad (3.27)$$

and expanding the double dot product the energy equation in terms of T becomes:

$$\begin{aligned} \frac{\partial}{\partial t}(\rho c_p T) + \nabla \cdot (\rho c_p \mathbf{v} T) = & \nabla \cdot (k \nabla T) \\ & + \rho T \frac{Dc_p}{Dt} - \left(\frac{\partial(\ln \rho)}{\partial(\ln T)}\right)_p \frac{Dp}{Dt} + \lambda \Psi + \mu \Phi + \dot{q}_v \end{aligned} \quad (3.28)$$

This equation is rarely solved in its full form and depending on the physical situation several simplified versions can be developed. For example the dissipation term Φ is negligible except for supersonic speed with large velocity gradient [19].

For incompressible fluids both Ψ and $\left(\frac{\partial(\ln \rho)}{\partial(\ln T)}\right)_p$ are equal to zero and Eq.(3.28) is reduced to

$$\frac{\partial}{\partial t}(\rho c_p T) + \nabla \cdot (\rho c_p \mathbf{v} T) = \nabla \cdot (k \nabla T) + \dot{q}_v + Q^T \quad (3.29)$$

For the case of a solid, the density is constant, the velocity is zero, and if changes in temperature are not large then the thermal conductivity may be considered constant and the equation of energy becomes:

$$\rho c_p \frac{\partial T}{\partial t} = k \nabla^2 T + \dot{q}_v \quad (3.30)$$

3.2 Turbulence modelling

Most of industrial applications involve turbulent flows. It is difficult to give a precise definition of turbulence, but it is possible to list its most prominent features. Firstly, turbulence is a flow feature, not a fluid feature [44]. Turbulent flows appear chaotic, presenting strong fluctuations of pressure and velocity both in time and space, which makes difficult to describe them via a full deterministic approach. Related to the presence of intense fluctuations, turbulent flows present and high effective diffusivity and, consequently, higher transfer rates for mass, heat and momentum than laminar flows. Furthermore, turbulence is a full three-dimensional phenomenon, and it is characterised by the activation of a wide range of scales through a cascade process whereby the kinetic energy is transferred from larger eddies to smaller eddies and the latter dissipate into heat due to molecular viscosity. It is possible to estimate the magnitude of the smallest scale through dimensional analysis. As stated above the cascade process involves a transfer of turbulent kinetic energy k (associated to fluctuating turbulent velocity) from larger eddies to smaller ones. The smaller eddies should be in a state where the rate at which they receive energy from larger eddies is very nearly equal to the rate at which the smallest eddies dissipate the energy to heat [48]. Hence the motion at the smallest scales should depend only upon the rate at which the larger eddies supply energy, $\epsilon = -\frac{dk}{dt}$ and the kinematic viscosity ν . Having established appropriate dimensional quantities for ϵ and ν one can derive the *Kolmogorov* scales of length, time and velocity

$$\eta = \left(\frac{\nu^3}{\epsilon}\right)^{\frac{1}{4}}, \quad \tau = \left(\frac{\nu}{\epsilon}\right)^{\frac{1}{2}}, \quad v = (\nu\epsilon)^{\frac{1}{4}} \quad (3.31)$$

With dimensional analysis the dissipation rate ϵ could be related with k through:

$$\epsilon \sim \frac{k^{\frac{3}{2}}}{l} \quad (3.32)$$

where l is the integral length scale of the largest eddies. Hence the ratio

$$\frac{l}{\eta} \sim Re_t^{\frac{3}{4}} \quad (3.33)$$

with Re_t being the turbulence Reynolds number based on l and k . Thus, the energy cascade involves a number of scales proportional to N :

$$N = Re_t^{\frac{9}{4}} \quad (3.34)$$

It is now clear that in order to ensure that a numerical simulation can predict correctly all the features of a turbulent flow, the grid onto which the governing equations are discretised may require an exceptionally high number of points. To describe exactly (up to the precision of the numerical methods) all the degree of freedom of the system means to employ the *DNS* (direct numerical simulation) approach and it is not affordable for industrial applications because of the need to obtain results within a reasonable time and because of the great request of computational resources. Hence a mathematical model is required to predict turbulent flow properties considering only an subset of the degree of freedom of the system. Modelling turbulence involves statistical studies of the equations of fluid flow and always leads to the closure problem: more unknowns than equations. In order to make the number of equations equal to the number of unknowns, assumptions are imperative. Usually there are two approaches: filtering in space or averaging in time. The first approach called *LES* (large eddy simulation) consists on applying a spatial filter to Navier-Stokes equations with only the length scales smaller than the size of the filter modelled. However, LESs remain unfeasible as well for most of industrial applications and nowadays time averaging is still the most common approach. The strategy is to decompose the flow variables into a time-mean value component and a fluctuating one, substituting in the original equations, and time-averaging the obtained equations. Expressing the instantaneous velocity as the sum of a mean and a fluctuating part:

$$\mathbf{v}(\mathbf{x}, t) = \bar{\mathbf{v}}(\mathbf{x}) + \mathbf{v}'(\mathbf{x}, t) \quad (3.35)$$

The time-averaging properties lead to the following expression for the incompressible continuity, momentum, energy equations:

$$\nabla \cdot (\rho \bar{\mathbf{v}}) = 0 \quad (3.36)$$

$$\frac{\partial \rho \bar{\mathbf{v}}}{\partial t} + \nabla \cdot \{\rho \bar{\mathbf{v}} \bar{\mathbf{v}}\} = -\nabla \bar{p} + \nabla \cdot (\bar{\boldsymbol{\tau}} - \rho \overline{\mathbf{v}' \mathbf{v}'}) + \rho \mathbf{g} \quad (3.37)$$

$$\frac{\partial}{\partial t} (\rho c_p \bar{T}) + \nabla \cdot (\rho c_p \bar{\mathbf{v}} \bar{T}) = \nabla \cdot (k \nabla \bar{T} - \rho c_p \overline{\mathbf{v}' T'}) + \bar{S}^T \quad (3.38)$$

These equations are usually denoted as Reynolds Averaged Navier Stokes (RANS) equations. Keeping the unsteady term $\frac{\partial \rho \bar{\mathbf{v}}}{\partial t}$ in the momentum equation usually brings to the definitions of *URANS* (unsteady Reynolds averaged Navier-Stokes), but attention should be maintained for those turbulent flows where there is no clear distinction between timescale characteristic of slow variations of the mean flow and that related to turbulent fluctuations. Indeed, the approximation

$$\frac{\partial \overline{\mathbf{v}(\mathbf{x}, t)}}{\partial t} \approx \frac{\partial \bar{\mathbf{v}}(\mathbf{x})}{\partial t} \quad (3.39)$$

is true if $|\mathbf{v}'| \ll |\bar{\mathbf{v}}|$. This is always questionable, however using time averaging in this manner is useful for analysis especially for time marching numerical methods implemented for solving fluid dynamics problems but a degree of caution must be exercised when fluctuations are not too small. Comparing Eq.(3.37) with Eq.(3.7) and Eq.(3.29) with Eq.(3.38), one can note the appearance of new terms on the right-hand-side. These terms are called *Reynolds Stresses Tensor* and *turbulent heat fluxes*. So what Reynolds-averaging does is to introduce 9 new variables and to solve the *RANS* equations, together with new equations for the the unknown just introduced.

Here comes into play the *Boussinesq Hypothesis* which makes an analogy with Newtonian fluids by assuming that the *Reynolds stresses* are a linear function of the *mean velocity gradients*

$$-\overline{\rho \mathbf{v}' \mathbf{v}'} = \mu_T [\nabla \mathbf{v} + (\nabla \mathbf{v})^T] - \frac{2}{3} \rho k \mathbf{I} \quad (3.40)$$

This assumption reduces the number of unknown from 6 to 2: the *turbulent eddy viscosity* μ_T and the *turbulent kinetic energy* k .

For incompressible flows, the equations can be rearranged by defining a *turbulent pressure* p [19]:

$$p \leftarrow p + \frac{2}{3}\rho k \quad (3.41)$$

In this manner, the only unknown that remains to compute is the *turbulent eddy viscosity* μ_T . The great variety of turbulence models derive from different ways of evaluating μ_T . In a similar way, the turbulent thermal fluxes are calculated in analogy with Fourier's law such that

$$-\rho c_p \overline{\mathbf{v}'T'} = \alpha_t \nabla T \quad (3.42)$$

where α_t is the turbulent thermal diffusivity.

The RANS approach proves often sufficient to estimate integrated quantities, such as the pressure distribution over a surface, but it is less reliable for cases when the instantaneous fluctuations affect directly the quantities of interest. This is the case for particle dynamics and therefore we will focus on the LES approach in the following.

3.2.1 General principles

To introduce the *Large Eddy Simulations* (LES), it is useful to quote Ferziger [45]:

“ The idea is to simulate the larger scales of motions of the turbulence while approximating the smaller ones. One can think of it as applying DNS to the large scales and RANS to the small scales [...]. The justification for such a treatment is that the larger eddies contain most of the energy, do most of the transporting of the conserved properties, and vary most from flow to flow; the smaller eddies are believed to be more universal and less important and should be easier to model.”

From a formal point of view, all the terms in the Navier-Stokes equation are substituted by filtered terms:

$$\tilde{U}_i(x) = \int G(x, r) U_i(r) dr \quad (3.43)$$

Where the function G represents the *filter*. The cut-off scale of the filter will be denoted as $\tilde{\Delta}$. Applying the filtering to the Navier-Stokes equations obtained are:

$$\tilde{U}_i + \widetilde{U_i U_j} = \nu \frac{\partial^2 \tilde{U}_i}{\partial x_j \partial x_j} - \frac{1}{\rho} \tilde{p}_i \quad (3.44)$$

Since $\widetilde{U_i U_j} \neq \tilde{U}_i \tilde{U}_j$, we will have a closure issue which is different but analogous to what appears in the RANS case. If we defined the *residual stress tensor* τ_{ij}^R we obtain:

$$\tau_{ij}^R = \widetilde{U_i U_j} - \tilde{U}_i \tilde{U}_j \quad (3.45)$$

we can write the *filtered Navier-Stokes equation*:

$$\frac{\tilde{D} \tilde{U}_i}{\tilde{D} t} = \nu \frac{\partial^2 \tilde{U}_i}{\partial x_j \partial x_j} - \frac{\partial \tau_{ij}^R}{\partial x_j} - \frac{1}{\rho} \tilde{p}_i \quad \frac{\tilde{D}(\dots)}{\tilde{D} t} = \frac{\partial(\dots)}{\partial t} + \tilde{U}_i \frac{\partial(\dots)}{\partial x_i} \quad (3.46)$$

where the τ_{ij}^R is unknown.

As in the RANS case, a huge number of different strategies has been proposed, as well as different choices of the filter function. A brief summary is presented by Pope [43], for a general treatment we refers to Ferziger in [21], [45] and Pope in [42]. Here we only present the most fundamental concepts.

First of all, we should discuss what is the goal of a Large Eddy Simulation. Interpreting the definition that we have reported at the beginning of the section, we can state that the aim is to solve *enough* turbulent scales, in the sense that the unsolved part of the energy spectrum should be limited at the scales which have negligible effect in the specific case. Let us consider the energy spectrum where there is a clear subdivision between the production, the inertial and the dissipative range (Figure 3.1). While a DNS solves all the scales and a RANS simulation treats directly only the larger ones, a LES solves the scale up to the cut-off imposed by the filter. In this very idealise case, the cut-off frequency is chosen in the inertial range: as previously mentioned, the larger scales are explicitly solved, and a model is adopted to describe the small ones, where the turbulence can be reasonably treated as isotropic. This concepts are depicted in Figure 3.2.

We shall notice that it can be difficult to apply *pure* LES on complex flows where the range of scales is particular wide, for instance due to the geometry. Thus, structures such as the boundary layers, which does not contains *large eddies* by

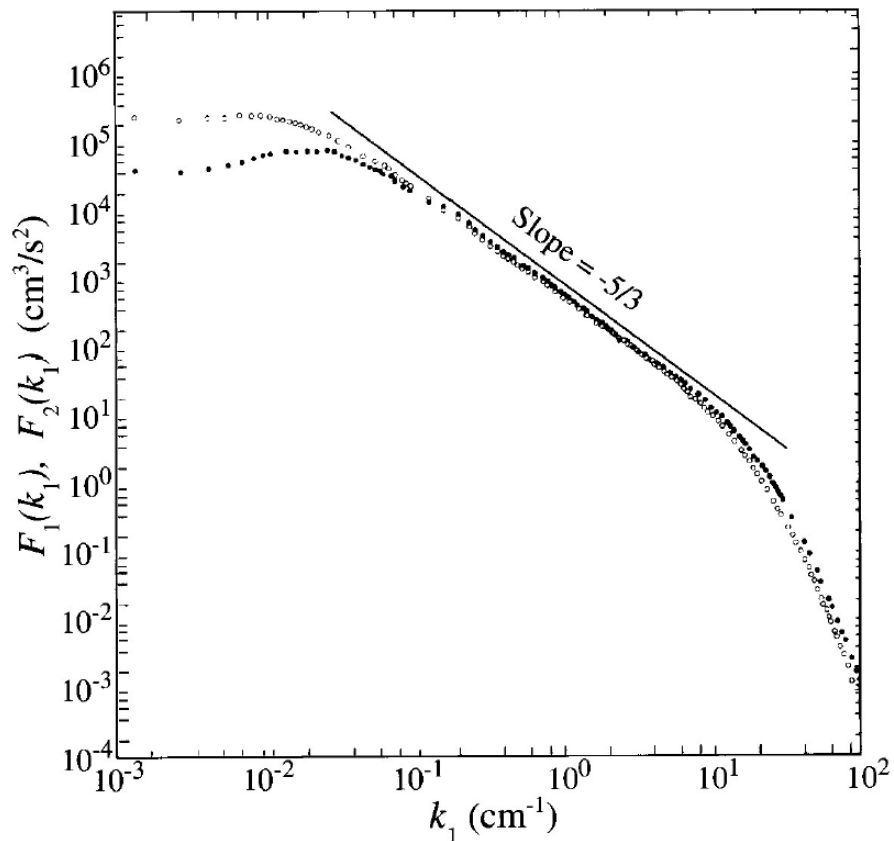


Figure 3.1: Energy cascade: log-log plot of the energy spectra of the streamwise and lateral components of the velocity fluctuations in a jet [46].

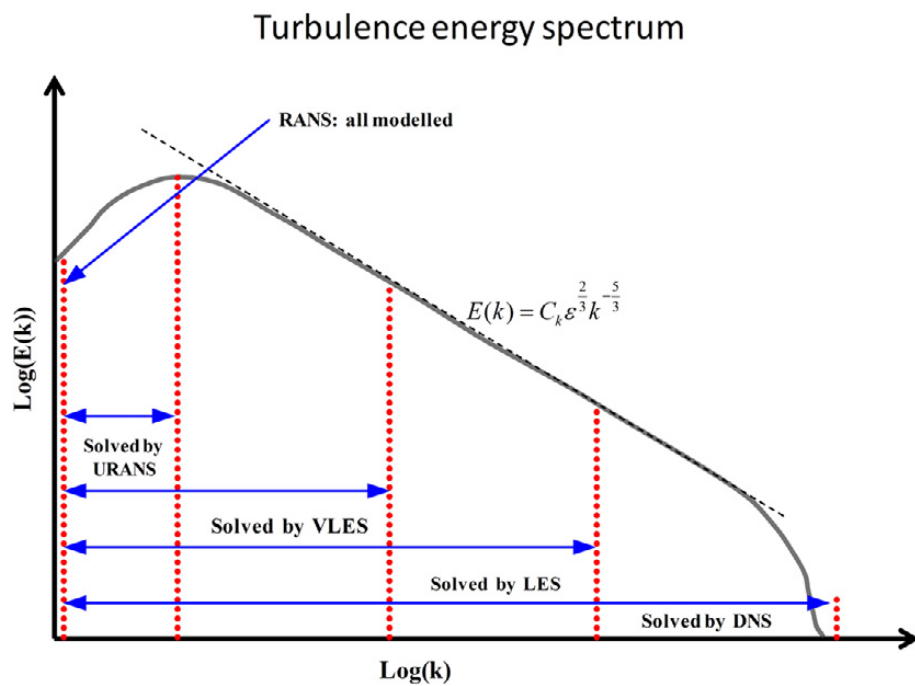


Figure 3.2: Simulation strategies and energy spectrum [9].

definition, are usually described via models ad hoc, often based on approximations of the analytical solution.

Another important point is how to apply the filtering. We will adopt models in which the filtering is directly related to the discretization in space. Intuitively, a significance drawback is a possible strong dependency on the discretization: more precisely, if the filters depends on the spacing, the model will be never *complete* [43]. To accept this choice is important to consider the *intermediate* nature of LES, and the consequence need of balancing three different aspects:

- the practise limit of computational power: the main scope of an LES is to obtain a result *good enough*, without performing a DNS;
- the errors related to the unsolved physics: saving resource means, crudely, to avoid to solve all the turbulent scales, and it will always introduce an error – this is the typical flaw of a RANS simulation;
- the errors related to the numerical approximation – which is usually the critically point in a DNS.

At fixed computational time, with a filter cut-off which is bigger than the discretization spacing, the numerical errors are small but less scales can be solved [43]: in the ideal case, numerical errors and physical errors are of the same order of magnitude. However, it is worth to note that the best advantage of an LES, if compared to a RANS, is the fact that it is less dependent on the specific choice of the closure: the most important parameter is *supposed to be* the number of solved scales – i.e.: the discretization.

Finally, we can make a couple of comments about the closure strategies. It is possible to decompose the unknown residual stress tensor τ_{ij}^R in three terms which represent the different interaction between coherent structures larger and smaller than the filtering scale $\tilde{\Delta}$, but this decomposition is not of great help in modelling. Instead, the most common choice is to use again the turbulent viscosity hypothesis for the anisotropic terms:

$$\tau_{ij}^R = -\nu_T \left(\tilde{U}_{ij} + \tilde{U}_{ji} \right) = -2\nu_{sgs} \tilde{S}_{ij} \quad (3.47)$$

Due to the similarity between the RANS equation and the filtered Navier-Stokes equation, it is not surprising to find a sort of relationship between the closure strategies as well: the difference is that the effective viscosity in this case does not represent the influence of the all turbulence scales but of the smaller coherent structures. It reflects in the notation, where ν_T is substituted by the *sub-grid scale* viscosity: ν_{sgs} . A significant consequence of this difference is that the cut-off scale $\tilde{\Delta}$ becomes a natural choice for the length scale l^* of the modelled turbulence. Thus we have the *return* of incomplete models, which have been judged not general enough for RANS simulations because they require l^* as input, while two equations model are not needed.

Two different closure strategies will be described in the next paragraphs.

3.2.2 Smagorinsky closure

First proposed by Smagorinsky in the 1963 [22] and then justified by Lilly [14], the so called *Smagorinsky closure* is directly linked with the Kolomogorov theory. It has been derived from several different points of view, due to its popularity: we will refer here to the notes of Ferziger in [45].

Being \mathcal{L} and \mathcal{U} the integral scale and the velocity scale of the larger coherent structures, let us defined \tilde{u} a characteristic velocity for the structure smaller than the filtering scale $\tilde{\Delta}$. According to the Kolmogorov theory, in the approximation of very high Reynolds number, the rate of energy transfer from the larger scales to the smaller ones is constant in the inertial range (see again Figure 3.2). Thus we can write:

$$\approx \mathcal{U}^3 \mathcal{L}^{-1} \approx \tilde{u}^3 \tilde{\Delta}^{-1} \quad (3.48)$$

The energy transfer to scales smaller than $\tilde{\Delta}$ can be described via the effective viscosity:

$$= \nu_{sgs} \tilde{u}^2 \tilde{\Delta}^{-2} \quad (3.49)$$

Considering these relations and because via dimensional analysis $\nu_{sgs} \propto \tilde{u} \tilde{\Delta}$, we can write:

$$\nu_{SGS} \approx \mathcal{U} \tilde{\Delta}^{4/3} \mathcal{L}^{-1/3} \quad (3.50)$$

The most critic passages in the model are required to eliminate the dependency on the large scale values \mathcal{U} and \mathcal{L} , which would be impossible to estimate a priori. The standard assumptions are:

$$\mathcal{U} \approx \mathcal{L} \left(\tilde{S}_{ij} \tilde{S}_{ij} \right)^{1/2} \quad \tilde{\Delta}^{4/3} \mathcal{L}^{2/3} \approx (C_S \tilde{\Delta})^2 \quad (3.51)$$

Where it can be proved that $C_S \simeq 2.1$ in the Kolmogorov theory.

$$\nu_{sgs} = (C_S \tilde{\Delta})^2 \cdot \mathcal{S} \quad \mathcal{S} \equiv \left(\tilde{S}_{ij} \tilde{S}_{ij} \right)^{1/2} \quad (3.52)$$

A weak point of the Smagorinsky model, in its original implementation, is that it can overestimate ν_{sgs} in the near-wall regions, because the proportional relation between \mathcal{L} and $\tilde{\Delta}$ is true only in the homogeneous case. The most linear solution is to include in the definition of C_S a damping function. As for the RANS models, several improvements have been implemented but it is not our purpose to delve into them in this work.

3.2.3 Spallart-Allmaras equation models

One of the alternatives to the Smagorinsky model comes from an opposite approach to the closure problem. In 1992 P. Spallart and S. Allmaras [37] proposed a one-equation model aimed to aerodynamic flows. Instead of starting from theoretical considerations, they directly developed a transport equation for the effective viscosity ν_t via empirical consideration, which is currently known as the Spallart-Allmaras equation.

$$\frac{D\nu_t^*}{Dt} = \mathcal{P}_\nu + T_\nu - \mathcal{D}_\nu \quad (3.53)$$

The star (...) variables are the standard ones plus a correction, needed to improve the behaviour of the model near the wall at low Reynolds number:

$$\nu_t = \nu_t^* f_{v1} \quad \mathcal{S}^* = \mathcal{S} + \frac{\nu_t}{\kappa^2 d^2} f_{v2} \quad (3.54)$$

κ is the Karman constant, which appears in the expression for the logarithmic velocity profile in the boundary layer and f_{v1} and f_{v2} can be considered as damping functions.

- The production term for \mathcal{P}_ν is:

$$\mathcal{P}_\nu = c_{b1}(1 - f_t)\mathcal{S}^*\nu_t^* + f_{t1}\Delta U \quad (3.55)$$

Where c_{b1} is a constant, ΔU is the norm of the difference between the velocity near the wall and in the free stream region and f_{t1} is an empirical function which describes the transition between the laminar and the turbulent regime in the boundary layer.

- The transport term T_ν is actually not *only* a transport term:

$$T_\nu = \frac{1}{\sigma_\nu} (i((\nu + \nu_t^*)\nu_t^*i) + c_{b2}(\partial\nu_t^*i\partial\nu_t^*i)) \quad (3.56)$$

indeed, the integral of $\partial_i\nu_t^*\partial_i\nu_t^*$ does not vanish so that T_ν works also as a destruction term in the free shear flows. The choice of including a destruction term in the diffusive term has been due to the fact that it is not possible to write an exact destruction term for the turbulent viscosity. The calibration of the constant c_{b2} controls the behaviour in homogeneous turbulence.

- The *pure* destruction term \mathcal{D}_ν is responsible just for the reduction of ν_t near the walls:

$$\left(c_{w1}f_w - \frac{c_{b1}}{\kappa^2}f_{t2}\right) \left(\frac{\nu_t^*}{d}\right)^2 \quad (3.57)$$

d is the distance to the wall, the constant c_{w1} is derived by imposing the equilibrium with the production and the dissipative part of the diffusive term in the free shear region, the function f_{w2} allows a better description of the boundary layers and f_{t2} has the same aim of f_{t1} .

For the sake of clarity, we report the form of the Spalart-Allmaras equation for high Reynolds number, which appears a little bit more friendly:

$$\frac{D\nu_t}{Dt} = c_{b1}\mathcal{S}\nu_t + \frac{1}{\sigma_\nu} (i(\partial\nu_t\partial\nu_t i) + c_{b2}(\partial\nu_t i\partial\nu_t i)) - c_{w1}f_w \left(\frac{\nu_t}{d}\right)^2 \quad (3.58)$$

The complexity of the model and its strong dependency on the calibration make it reliable in the specific applications for which it has been developed, but for general cases the two-equation models are preferred in RANS simulations. Nevertheless, its good performance in the boundary layer regions gave it a *new life*.

Considering the difficulties of the more “classical” Smagorinsky model in the boundary layers, in the 1997 [39] it has been proposed to adapt the Spalart-Allmaras equation to a LES to compute ν_{sgs} . In practise (3.58) has been turned into (we focus on the high Re form for simplicity):

$$\frac{D\nu_{sgs}}{Dt} = c_{b1}S\nu_{sgs} + \frac{1}{\sigma} (i(\partial\nu_{sgs}\partial\nu_{sgs}i) + (\dots)) - c_{w1}f_w \left(\frac{\nu_{sgs}}{\tilde{d}} \right)^2 \quad (3.59)$$

Where the distance to wall d has been substituted by \tilde{d} , which is the minimum between the d itself and a characteristic length:

$$\tilde{d} \equiv \min[d, C_{des}\Delta] \quad (3.60)$$

The length Δ has been defined based on the spacial discretisation Δ_x (not accidentally), it is somehow analogous to (3.52).

The new simulation strategy has been named *Detached Eddy Simulation* (DES), referring to the idea that the *attached* eddies, in the boundary layers, would be modelled and the *detached* ones would be solved.

The crucial point in the DES is the choice of \tilde{d} , which physically means the choice on where the destruction term *swaps* from the RANS to the LES behaviour. At the time of the first formulation non homogeneous meshes have been widely use to save computational time and the most complex cases are still relatively simple: so, it could be reasonably to chose Δ directly based on the grid spacing Δ_x , because it has been chosen accordingly to shape of the flow. The behaviour of the model in this case is explained by Figure 3.3.

To allow a more general use, in [38] the definition of \tilde{d} has been modified as well as the blending functions $f(\dots)$. Because the improvements consists in the capability of *postponing* the swap from the RANS to the LES mode, so that the boundary layers are treated in RANS model also in homogeneous meshes, the authors named the new model *Delayed Detached Eddy Simulation* (DDES).

At last, further developments, aimed to improve the connecting between the RANS and the LES regime, led to the *Improved Delayed Detached Simulation* (IDDES) [29].

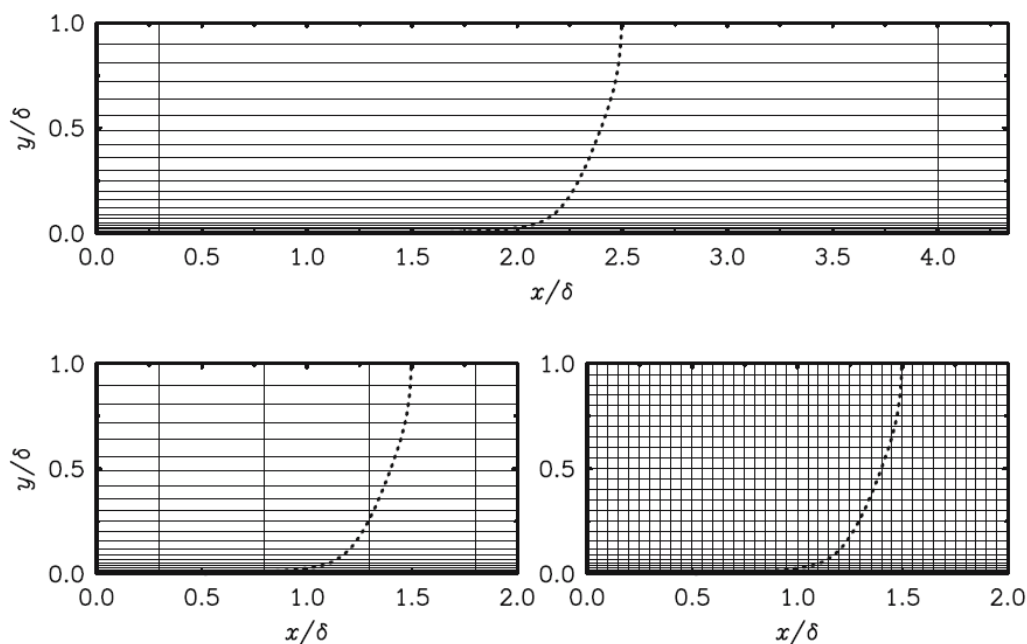


Figure 3.3: The natural frame of the original Detached Eddy Simulation is the grid on the top while the grid on the right is typical for pure LES. The example on the left represents the ambiguous spacing which requires the development of the DDES [38].

3.3 Near the wall treatment

On every solid surface, due to the fluid viscosity, a boundary layer develops. This layer of fluid can be divided in three regions:

- *viscous sub-layer* ($0 < y^+ < 5$), where the effect of viscosity dominates;
- *buffer sub-layer* ($5 < y^+ < 30$), where viscous and inertial effects are equal;
- *inertial (log-law) sub-layer* ($30 < y^+ < 500$), where the effect of inertia dominates.

These three sub-layers can be identified by the value of y^+ that is the adimensionalized normal distance (d_{\perp}) from the wall:

$$y^+ = \frac{d_{\perp} u_{\tau}}{\nu} \quad (3.61)$$

where $u_{\tau} = \sqrt{\tau_w/\rho}$ is the velocity scale.

This subdivision of the boundary layer is schematized in *Figure 3.4*.

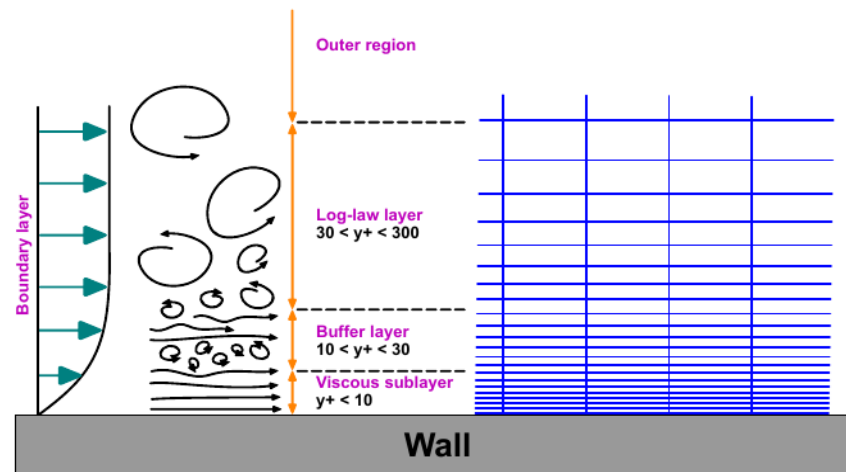


Figure 3.4: *Boundary layer subdivision and correspondent y^+ ranges (courtesy of Wolf Dynamics srl [1]).*

Turbulence models avoid the *buffer sub-layer*, because the high turbulent production, by placing the first cell center in the *viscous sub-layer* or in the *inertial sub-layer*.

The first option leads to accurate prediction of the boundary layer, but requires a very fine discretization near the wall, usually leading to unaffordable costs.

The second, combined by the definition an appropriate wall-value to each new variable introduced, significantly reduces computational costs while giving a good accuracy. This velocity profile is called *wall function* and its action is schematized in *Figure 3.5*.

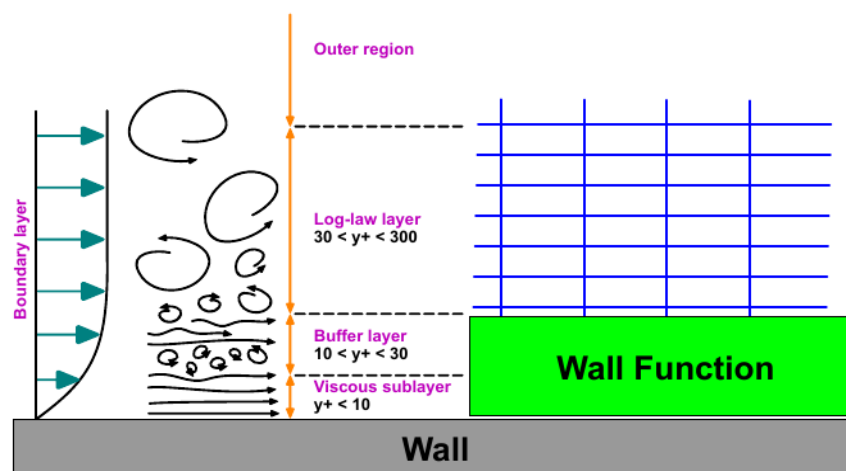


Figure 3.5: *Representation of the wall function approach [1].*

3.4 Flow with particles

To numerically model a multiphase flow, it is often important to use separate formulations for the different phases. The *particle phase* consists of bubble, particle, or drops and the *continuous phase* is the fluid in which these particles are generally immersed. The particle can be composed of solid, liquid, or gas, and the continuous fluid can be a liquid or a gas. The coupling between the particle motion and its surroundings can be used to classify the character of the multiphase flow, and thus help determine appropriate numerical techniques. The broadest division is between dispersed and dense flows, and refers to which coupling mechanism primarily determines the particle motion. A multiphase flow can be considered dispersed if the effect of particle–fluid interactions dominates the overall transport of the particles, while it is said to be dense if particle-particle interaction dominates particles motion. Dispersed flows includes one-way coupling (where the dispersed-phase motion is affected by the continuous phase, but not vice versa) and two-way coupling (where the dispersed phase also affects the continuous phase through the interphase coupling). Dense flows usually have four-way coupling where mutual interactions between particles become significant and the effects of the particles on the continuous fluid are weak and often neglected. As well described in [17] volume fraction of particles is the main parameter to make the division between one, two or four way coupling and therefore between dispersed and dense. The volume fraction is defined as $\Phi_p = \frac{MV_p}{V}$ where M is the number of particles, V_p is the volume of a single particle and V is the volume occupied by particles and fluid:

- for $\Phi_p < 10^{-6}$ there will be one-way coupling;
- for $10^{-6} < \Phi_p < 10^{-3}$ there will be two-way coupling and the particles can also increase or dump turbulence;
- for $\Phi_p > 10^{-3}$ there will be four-coupling and the flow will be considered as dense.

Another important parameter that may contribute to the selection of the appropriate model is the particle momentum *Stokes number* defined as the ratio between the

particle response time τ_p and that of the system τ_s :

$$St = \frac{\tau_p}{\tau_s}, \quad (3.62)$$

$$\tau_p = \frac{\rho_p d^2}{18\rho_f \nu} \quad (\text{only for Stokes flows}), \quad (3.63)$$

$$\tau_s = \frac{L_s}{v_s} \quad (3.64)$$

If $St \rightarrow 0$, the particle behaves as a fluid tracer (momentum one-way coupling) and if $St \rightarrow \infty$ is unresponsive to the flow variations. One would define a Stokes number not only for momentum but also for mass and temperature in order to evaluate with more precision the mass coupling and energy coupling of particles with the continuous phase. If two-way coupling is considered, it simply involves some source terms in the continuous phase equations (momentum, energy, turbulence models...) that are generally described in an Eulerian reference frame. For the sake of simplicity, we have limited our interest to the one-way coupling.

3.4.1 Particle equations

Various treatments of the particle field can be employed. Particles could be described in an Eulerian or Lagrangian reference frame and, as suggested by E. Loth [27], distinctions could be done about the treatment of particle surface forces. In this work only the Lagrangian approach will be discussed. With this reference frame the particles are treated as individual and properties are updated along the path of each particle. For the treatment of the surface forces, the point-force treatment represents the flow over the particle with empirical and theoretical treatments (specifying a drag or lift coefficient) to obtain the force on the particle. For the resolved surface treatment, the fluid dynamics (e.g. pressure and shear stress distributions) are fully resolved over the entire particle surface and then integrated to obtain the overall hydrodynamic forces. Following the point-surface approach and defining \mathbf{x}_p as the particle centroid and m_p the particle mass, the Lagrangian particle equation of motion is:

$$m_p \frac{d\mathbf{v}}{dt} = \mathbf{F}_{body} + \mathbf{F}_{surf} \quad (3.65)$$

The left hand side represents the particle mass inertia and the right hand side represents the sum of body forces and surface forces on the particle. Body forces are those related to gravitational effects:

$$\mathbf{F}_{body} = \frac{(\rho_p - \rho)\pi d_p^3}{6} \mathbf{g} \quad (3.66)$$

Where d_p are ρ_p are respectively the droplet diameter and droplet density. Surface forces can be seen as the sum of different terms: drag, virtual mass, a term related to pressure gradient and one to the “history” of particle (Basset term). The expressions for all these terms are listed below without a rigorous derivation:

- The drag force is:

$$F_{D,i} = \frac{1}{2} \frac{\pi d_p^2}{4} \rho_f C_d |\mathbf{u} - \mathbf{u}_p| (u_i - u_{p,i}), \quad C_d = \frac{24}{Re_p} \left(1 + \frac{3}{16} Re_p\right) \quad (3.67)$$

- The pressure gradient force is:

$$F_{P,i} = \frac{1}{6} \pi d_p^3 \rho_f \frac{Du_i}{Dt} \quad (3.68)$$

- The added mass force (virtual force) is:

$$F_{A,i} = \frac{\pi d_p^3}{12} \rho_f \left(\frac{Du_i}{Dt} - \frac{du_{p,i}}{dt} \right) \quad (3.69)$$

- The Basset force is:

$$F_{B,i} = \frac{3}{2} d_p^2 \rho_f \sqrt{\pi \nu} \int_{-\infty}^t \frac{d}{d\tau} (u_i - u_{p,i}) \frac{d\tau}{\sqrt{t - \tau}} \quad (3.70)$$

where Re_p is the particle Reynolds number based on relative velocity:

$$Re_p = \frac{\rho d_p (\mathbf{u} - \mathbf{u}_p)}{\mu} \quad (3.71)$$

where ρ is the density of the continuous phase. A better description of all these terms can be found in [27] and in [12].

3.4.2 Kinetic of drying process

The dispersed phase can exchange not only momentum but also mass and heat with the continuous phase. Such phenomena are discussed below in a complete description of the entire drying kinetics for a single droplet. Before introducing the model, a brief introduction to mechanism of mass and heat transfer involved in that process is provided.

3.4.3 Mass transfer: diffusion and convection

Fick's law of diffusion

Diffusion is the process by which molecules, ions, or other small particles spontaneously mix, moving from regions of relatively high concentration into regions of lower concentration. This process can be analyzed through the Fick's law of diffusion that states that the rate of diffusion of a chemical species at a location in a gas mixture (liquid or solution) is proportional to the concentration gradient of that species at that location. The following notation is coherent with [10] where the concentration of a species can be expressed in a mass basis or mole basis way. On a mass basis, concentration is expressed in terms of density ρ or in dimensionless form in terms of mass fraction w :

$$\rho_i = \frac{m_i}{V} \quad (3.72)$$

$$\rho = \sum \rho_i \quad (3.73)$$

$$w_i = \frac{\rho_i}{\rho} \quad (3.74)$$

On a mole basis, concentration is expressed in terms of molar concentration C or in dimensionless form in terms of mole fraction y :

$$C_i = \frac{N_i}{V} \quad (3.75)$$

$$C = \sum C_i \quad (3.76)$$

$$y_i = \frac{C_i}{C} \quad (3.77)$$

The mass m and the mole number N are related by $m = NM$ where M is the molar mass. Therefore for the i th species i :

$$C_i = \frac{\rho_i}{M_i} \quad (3.78)$$

$$w_i = y_i \frac{M_i}{M} \quad (3.79)$$

Following the Dalton's law of pressure according to which the total pressure of a gas mixture P is equal to the sum of the partial pressures P_i and reminding that for ideal gas $PV = NR_uT$, the mole fraction y_i may be written as:

$$\frac{P_i}{P} = \frac{N_i R_u T / V}{N R_u T / V} = y_i \quad (3.80)$$

The linear relationship between the rate of diffusion and the concentration gradient was proposed by Fick in 1855. Considering a *stationary* binary mixture composed by specie A and B the diffusive mass flux of species A , j_A , in the specified direction x is given by:

$$j_A = -\rho D_{AB} \frac{d(\rho_A/\rho)}{dx} = -\rho D_{AB} \frac{dw_A}{dx} \quad (3.81)$$

$$\bar{j}_A = -CD_{AB} \frac{d(C_A/C)}{dx} = -CD_{AB} \frac{dy_A}{dx} \quad (3.82)$$

If $\rho = \rho_A + \rho_B$ and $C = C_A + C_B$ is constant through the mixture:

$$j_A = -D_{AB} \frac{d\rho_A}{dx} \quad (3.83)$$

$$\bar{j}_A = -D_{AB} \frac{dC_A}{dx} \quad (3.84)$$

$$(3.85)$$

For two three-dimensional cases, Fick's law can conveniently be expressed in vector form:

$$\mathbf{j}_A = -\rho D_{AB} \nabla w_A \quad (3.86)$$

$$\bar{\mathbf{j}}_A = -CD_{AB} \nabla y_A \quad (3.87)$$

where D_{AB} is the diffusion coefficient usually determined experimentally.

Convection

Mass transfer problems usually involve diffusion in a moving medium, therefore species are transported both by molecular diffusion and by the bulk motion of the medium; that means by convection. Usually when dealing with this kind of problems it is common to refer to some experimental correlations in such a way very similar to the well known heat transfer convective correlations. Also, mass convection is usually analyzed on a mass basis approach and for the sake of simplicity the attention will be focused on fluids that are or can be treated as binary mixtures. The *Schmidt* number is a dimensionless number that expresses the ratio between the momentum diffusivity and the mass diffusivity, hence it is a useful parameter to compare the velocity boundary layer and concentration boundary layer. The Schmidt number is

written

$$Sc = \frac{\nu}{D_{AB}} \quad (3.88)$$

It is important to stress that the real physical mechanism of mass transfer is controlled by Fick's law of diffusion because of the no slip boundary condition for the bulk flow. However it is common to define a convective mass transfer coefficient h_{mass} in order to express the rate of mass convection as follow:

$$\dot{m}_{conv} = h_{mass}A(\rho_{As} - \rho_{A\infty}) \quad (3.89)$$

Where ρ_{As} , $\rho_{A\infty}$ are respectively the density of species A on the surface and out of the concentration boundary layer. The h_{mass} coefficient is expressed in terms of correlations through the *Sherwood* number, a dimensionless parameter that represents the effectiveness of mass convection at the surface. Defining a characteristic length L_c the Sherwood number is:

$$Sh = \frac{h_{mass}L_c}{D_{AB}} \quad (3.90)$$

For a given geometry and for a flow type, Sh is a function of the Reynolds number and Schmidt number Eq.(3.88). A well known example is given by the Ranz-Marshall correlation for mass transfer:

$$Sh = 2 + 0.6Re^{\frac{1}{2}}Sc^{\frac{1}{3}} \quad 0 \leq Re < 200 \quad (3.91)$$

The use of Eq.(3.89) is valid only for low mass flux because of the no slip boundary condition. This condition is still verified only if the rate of mass transfer of a species is small relative to the flow rate of that species. However it is possible to use with good approximation Eq.(3.89) for evaporation of water into air unless the water temperature reaches the saturation temperature for the external pressure condition. This for examples implies that Eq.(3.89) can't be used for evaporation of droplets in combustion chambers or generally speaking to mass transfer in boilers and condensers.

3.4.4 Heat transfer: diffusion and convection

Conduction

Heat transfer due to conduction takes place in solids and quiescent fluids. The heat is transferred by diffusion and collisions between particles, without any mass flow [36]. Heat transfer conduction is controlled by Fourier's law (see Eq.(3.25)) that states the relationship between the heat flow and the temperature gradient through the constant of proportionality k_c that is the thermal conductivity that in general varies with temperature. The 1D version of Eq.(3.30) without heat generation is:

$$\rho c_p \frac{\partial T}{\partial t} = \frac{\partial}{\partial x} \left(k_c \frac{\partial T}{\partial x} \right) \quad (3.92)$$

If k_c is constant with temperature then Eq.(3.92) reduces to:

$$\frac{1}{\alpha} \frac{\partial T}{\partial t} = \frac{\partial^2 T}{\partial x^2} \quad (3.93)$$

where $\alpha = \frac{k_c}{\rho c_p}$ is the thermal diffusivity and it's a measure of how much heat is conducted with respect to the heat stored within the body. For transient heat conduction problems, α , together with a reference length L_c , is used to make the distinction between "early" regime and "late" regime. Denoting with t the time associated with the process involved, and with Fo the respective dimensionless time it is possible to say:

$$Fo = \frac{\alpha t}{L_c^2} \ll 1 \quad (\text{Early regime}) \quad (3.94)$$

$$Fo = \frac{\alpha t}{L_c^2} \sim 1 \quad (\text{Transition}) \quad (3.95)$$

$$Fo = \frac{\alpha t}{L_c^2} \gg 1 \quad (\text{Late regime}) \quad (3.96)$$

For the "late regime" the lumped approximation is suitable if the dimensionless Biot number $Bi = \frac{hL_c}{k_c} \leq 0.1$, therefore it is possible to assume a uniform temperature distribution throughout the body. Hence Eq.(3.93) can be simplified:

$$m c_p \frac{dT}{dt} = hA(T_\infty - T) \quad (3.97)$$

where h is the convective heat transfer coefficient described in the next section. The Biot number could be seen as the ratio between the heat convected to the

body and the heat conducted within the body. The smaller the Biot number the more accurate the lumped approximation. For the “early regime” and “transition” regime Eq.(3.93) should be solved with appropriate boundary conditions; analytical solutions exist also in cylindrical and spherical problems, but they involve infinite series which are difficult to deal with. For $Fo > 0.2$ the one term approximation leads to small errors and solutions are also available in graphical form (Heisler’s chart [10]).

Convection

Heat transfer with the presence of bulk fluid motion is usually called convection, and the analogy with convection mass transfer will be clear at the end of this section. The bulk fluid motion increases heat transfer since it brings hotter and cooler fluid layers into contact and the higher the fluid velocity, the higher the rate of heat transfer. Usually the rate of convection heat transfer is expressed through the Newton’s law:

$$\dot{q}_{conv} = hA(T_s - T_\infty) \quad (3.98)$$

where h is the convection heat transfer coefficient. Because of the no slip boundary condition for fluid flow, heat is always transferred by conduction in the fluid layer near the surface, and then convected away because of the fluid motion. Therefore a rigorous definition of h is:

$$h = \frac{-k_{fluid} \frac{\partial T}{\partial y} |_{y=0}}{T_s - T_\infty} \quad (3.99)$$

The complete energy equation was presented in section 3.1.3, the resolution of which could bring the information about temperature distribution. If the temperature distribution is unknown, h is determined through correlations very similar to those described in mass convection section depending on the nature of fluid flow motion (laminar, turbulent, external, internal, forced or natural convection). Correlations usually involve adimensional numbers, such as the Prandtl’s number $Pr = \frac{\nu}{\alpha}$ and Nusselt’s number $Nu = \frac{hL_c}{k_{fluid}}$. Prandtl’s number is the ratio between momentum diffusivity and thermal diffusivity and provides information about the thickness of velocity and thermal boundary layers. The Nusselt number represents the enhancement of heat transfer through a fluid layer as a result of convection relative to

conduction across the same fluid layer. The larger the Nusselt number, the more effective the convection. Nu is a function of Re and Pr , for example the Ranz-Marshall correlation for convective heat transfer is:

$$Nu = 2 + 0.6Re^{\frac{1}{2}}Pr^{\frac{1}{3}} \quad (3.100)$$

3.4.5 Two-stage evaporation model

The overall drying process of droplets inside the spray dryer can be divided in two stages. During the first stage droplets containing solids and great amount of liquid enters the drying volume, gets sensible heat and evaporation occurs on the surface resulting in droplet diameter shrinking. During this first stage the liquid excess envelops the entire droplet volume and evaporation is very similar to the evaporation of pure water droplets [32]. When the droplet moisture content reaches a critical value, according to the model adopted, a solid crust surrounding a wet core is formed. At this point the droplet diameter is considered to be constant and only the wet core shrinks until the droplet reaches the final moisture content. During the second drying stage water vapour diffuses through the solid crust, and the rate at which it reaches the droplet surface depends on the crust porosity. The entire drying process is summarized in Fig.(3.6), where all features previously introduced are stressed.

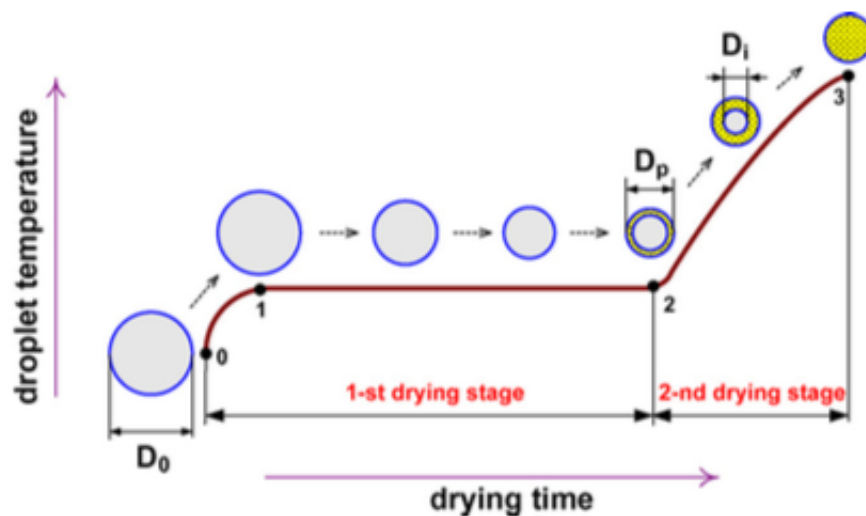


Figure 3.6: *Two stage model of droplet drying* [31].

3.4.6 First stage

Figure (3.6) shows that the first stage of evaporation can be considered as the sum of two additional steps:

- Droplet initial heating, where the droplet temperature rises, the rate of evaporation is very low, and the droplet radius is approximately constant;
- Constant temperature evaporation period, where the rate of evaporation (and therefore the rate at which heat is lost due to vaporization enthalpy) is enough to balance the heat transfer rate from the surrounding hot air;

If both conditions for a lumped approximation are satisfied, (see section 3.4.4) that means both $Fo \gg 1$ and $Biot < 0.1$, the equation of energy conservation for the droplet is:

$$h_{fg}\dot{m}_v + c_{p,d}m_d \frac{dT_d}{dt} = h(T_{air} - T_d)4\pi R_d^2 \quad (3.101)$$

where h_{fg} is the specific heat of evaporation, \dot{m}_v the vapour mass transfer rate, $m_d, c_{p,d}, T_d$ and R_d corresponding to mass, specific heat, temperature and radius of the dried droplet and h is the heat transfer coefficient [30]. The rate of moisture evaporation is controlled by Eq.(3.89) here specified for the specific case of single droplet:

$$\dot{m}_v = -\frac{dm_d}{dt} = 4\pi R_d^2 h_{mass}(\rho_{v,s} - \rho_{v\infty}) \quad (3.102)$$

where $\rho_{v,s}$ is the saturation density of water at droplet surface and it is a function of $T_{d,s}$. $\rho_{v\infty}$ is the vapour density in the surrounding air depending on its relative humidity and h_{mass} is the convective mass transfer coefficient. According to [15], the water vapour densities of the droplet and the gas are given by the following expressions:

$$\rho_{v,s} = \frac{M_w p_{sat}}{R_u T_{d,s}} \quad (3.103)$$

$$\rho_{v\infty} = \frac{M_w p_{v,air}}{R_u T_{air}} \quad (3.104)$$

where M_w is the water molecular weight, P_{sat} is the saturation pressure of water at droplet surface temperature, $P_{v,air}$ is the vapour partial pressure in the surrounding air and R_u is the universal gas constant. The convective mass transfer coefficient is

evaluated through the modified Ranz-Marshall correlation for spherical evaporating droplets:

$$Sh = \frac{d_d h_{mass}}{D_v} = (2 + 0.6 Re^{\frac{1}{2}} Sc^{\frac{1}{3}})(1 + B)^{-0.7} \quad (3.105)$$

The factor $(1 + B)^{-0.7}$ takes into consideration Stefan flow in the droplet boundary layer and $B = c_{p,v} \frac{(T_g - T_d)}{h_{fg}}$ is the Spalding number [31]. The diffusion coefficient of vapour in air in atmospheric conditions is evaluated as follows:

$$D_v = 3.564 \cdot 10^{-10} (T_{d,s} + T_g)^{1.75} \quad (3.106)$$

For the convective heat transfer coefficient in Eq.(3.101) a correlation very similar to Eq.(3.105) is used:

$$Nu = \frac{d_d h}{k_{air}} = (2 + 0.6 Re^{\frac{1}{2}} Pr^{\frac{1}{3}})(1 + B)^{-0.7} \quad (3.107)$$

where k_{air} is the air thermal conductivity. The expression for droplet specific heat $c_{p,d}$ in Eq.(3.101) takes into account the properties of the water and the solid fraction:

$$c_{p,d} = (1 - c)c_{p,w} + cc_{p,s} \quad (3.108)$$

Where c is the mass concentration of solid that is connected to the droplet moisture content, by:

$$x = \frac{m_w}{m_s} = \frac{m_d}{m_{d,0}}(1 + x_0) - 1 \quad (3.109)$$

$$c = \frac{1}{1 + x} \quad (3.110)$$

where x_0 and $m_{d,0}$ are the droplet initial moisture content and initial mass. The droplet diameter is shrinking due to evaporation and, for the mass conservation, it can be computed from:

$$\frac{dR_d}{dt} = -\frac{\dot{m}_v}{\rho_w 4\pi R_d^2} \quad (3.111)$$

Integrating Eq.(3.111) it is possible to follow also the evolution of the droplet mass:

$$m_d = m_{d,0} - \pi \rho_w \frac{8}{6} (R_{d,0}^3 - R_d^3) \quad (3.112)$$

Usually a lumped approximation is acceptable for small droplets since $Fo \sim \frac{1}{R_d^2}$ and $Biot \sim R_d$. However, if the droplets radius isn't small enough, the Fo number at

the end of the initial heating period does not satisfy the lumped condition, therefore the transient is too fast and the effect of temperature rise do not have interested all the characteristic length of the droplet (radius), and the temperature profile within the droplet may be considered. In this case the equation of energy conservation for the initial heating is:

$$\rho c_{p,d} \frac{\partial T_d(r,t)}{\partial t} = \frac{1}{r^2} \frac{\partial}{\partial r} \left(k_d r^2 \frac{\partial T_d}{\partial r} \right) \quad (3.113)$$

and the corresponding boundary conditions are:

$$\begin{cases} \frac{\partial T_d}{\partial r} = 0 & \text{for } r = 0 \\ h(T_g - T_d) = k_d \frac{\partial T_d}{\partial r} & \text{for } r = R_d \end{cases}$$

At the end of the initial heating stage, when evaporation is considerable and the droplet radius starts to shrink significantly, the droplet Fourier and Biot numbers could rapidly exceed the lumped approximation limits and, for the subsequent evaporation stage at constant temperature, both radial and temporal variations of the droplet can be neglected. From this point on this approach will be called “Uniform temperature approach”. This results in the following equation of energy conservation:

$$h_{fg} \dot{m}_v = h(T_g - T_d) A_d \quad (3.114)$$

Combining Eq.(3.114) with Eq.(3.89) and introducing Eq.(3.107), Eq.(3.105) and Eq.(3.103) the following equation is obtained:

$$\frac{T_g - T_d}{h_{fg}} = \frac{2 + 0.6 Re_d^{\frac{1}{2}} Sc^{\frac{1}{3}} D_v M_w}{2 + 0.6 Re_d^{\frac{1}{2}} Pr^{\frac{1}{3}} k_{air} R_u} \left(\frac{p_{v,s}}{T_d} - \frac{p_{v,\infty}}{T_{air}} \right) \quad (3.115)$$

Solving for T_d the equilibrium evaporation temperature is obtained and droplet properties could be tracked with Eq.(3.109), Eq.(3.111) and with Eq.(3.112). In the case when lumped conditions are not satisfied, the fully transient approach is needed and the energy conservation equation is applied to a time dependent spatial domain:

$$\rho c_{p,d} \frac{\partial T_d(r,t)}{\partial t} = \frac{1}{r^2} \frac{\partial}{\partial r} \left(k_d r^2 \frac{\partial T_d(r,t)}{\partial r} \right) \quad (3.116)$$

and the corresponding boundary conditions are:

$$\begin{cases} \frac{\partial T_d}{\partial r} = 0 & \text{for } r = 0 \\ h(T_g - T_d) = k_d \frac{\partial T_d}{\partial r} + h_{fg} \frac{\dot{m}_v}{A_d} & \text{for } r = R_d \end{cases}$$

3.4.7 Second stage

When the droplet moisture content falls below a certain critical value, a solid crust starts to develop on the entire droplet surface. A wet core still exists but, from now on, vapour diffuses through the crust that is considered to be porous [34]. For this stage the fully transient approach is considered and both temperature variation with time and radius are evaluated.

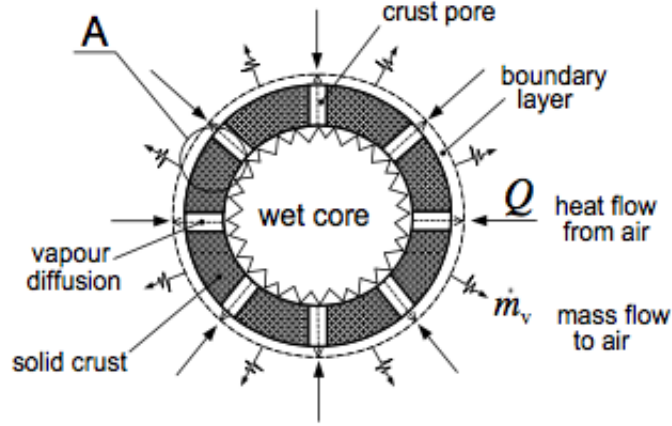


Figure 3.7: Details of the second stage [33].

During the second stage of evaporation the external diameter is constant while the wet core shrinks because of evaporation and, as a result, the crust thickness increases. This problem is classified as a problem with internal moving evaporating interface [34]. Therefore two energy equations are required: one for the crust and one for the wet core. With respect to the crust region, the assumption of temperature independent crust thermal conductivity leads to:

$$\frac{\partial T_{cr}(r, t)}{\partial t} = \frac{\alpha_{cr}}{r^2} \frac{\partial}{\partial r} \left(r^2 \frac{\partial T_{cr}(r, t)}{\partial r} \right) \quad R_i(t) \leq r \leq R_p \quad (3.117)$$

and the corresponding boundary conditions are:

$$\begin{cases} k_{cr} \frac{\partial T_{cr}}{\partial r} = k_{wc} \frac{\partial T_{wc}}{\partial r} + h_{fg} \frac{\dot{m}_v}{A_i} & \text{for } r = R_i(t) \\ T_{wc} = T_{cr} & \text{for } r = R_i(t) \\ h(T_g - T_{cr}) = k_{cr} \frac{\partial T_{cr}}{\partial r} & \text{for } r = R_p \end{cases}$$

where R_P is the fixed external radius, and h is the convective heat transfer coefficient evaluated with Eq.(3.107). The wet core the energy conservation equation is:

$$\rho_{wc}c_{p,wc}\frac{\partial T_{wc}(r,t)}{\partial t} = \frac{1}{r^2}\frac{\partial}{\partial r}\left(k_{wc}r^2\frac{\partial T_{wc}(r,t)}{\partial r}\right) \quad 0 \leq r \leq R_i(t) \quad (3.118)$$

The corresponding boundary conditions are:

$$\begin{cases} \frac{\partial T_{wc}}{\partial r} = 0 & \text{for } r = 0 \\ k_{cr}\frac{\partial T_{cr}}{\partial r} = k_{wc}\frac{\partial T_{wc}}{\partial r} + h_{fg}\frac{\dot{m}_v}{A_i} & \text{for } r = R_i(t) \\ T_{cr} = T_{wc} & \text{for } r = R_i(t) \end{cases}$$

The rate of interface receding is given by [15]:

$$\frac{dR_i}{dt} = -\frac{\dot{m}_v}{\varepsilon\rho_w4\pi R_i^2} \quad (3.119)$$

where ε is the crust porosity. The mass transfer rate from the spherical wet core can be evaluated through the Stefan's flow approximation [15] which leads to:

$$\dot{m}_v = -\frac{8\pi\varepsilon D_v M_w p_g}{R(T_{cr,s} + T_{wc,s})} \frac{R_P R_i}{R_P - R_i} \ln\left(\frac{p_g - p_{v,i}}{p_g - T_{cr,s}\left(\frac{R_u \dot{m}_v}{4\pi M_w h_{mass} R_P^2} + \frac{p_{v,\infty}}{T_g}\right)}\right) \quad (3.120)$$

The diffusion coefficient D_v is evaluated with Eq.(3.105). The particle moisture content and mass are given by:

$$x = m_p \frac{1 + x_0}{m_{d,0}} - 1 \quad (3.121)$$

$$m_p = \frac{m_{d,0}}{1 + x_0} \left(1 - \frac{\rho_w}{\rho_{solid}}\right) + \frac{4}{3}\pi\rho_w(\varepsilon R_i^3 + (1 - \varepsilon)R_P^3) \quad (3.122)$$

According to the lumped approximation described for the first drying stage, also here it is possible to track the droplet temperature with a simpler approach. When the critical moisture content is reached, the wet particle turns into a non evaporating dry particle. This non-evaporating particle and the drying gas continue their interaction by convective heat transfer until thermal equilibrium. The particle temperature is determined from the following heat balance equation:

$$m_p c_p \frac{\partial T_p}{\partial t} = 4\pi R_p^2 h (T_g - T_p) \quad (3.123)$$

Because there is no more evaporation, the particle mass during this period remains invariable as well as its radius and its moisture content. This is a great simplification, the wet core is neglected and the crust does not grow, but this can provide some preliminary informations about the wet particle temperature rise.

Chapter 4

Numerical modeling with OpenFOAM

4.1 About OpenFOAM

OPENFOAM[®] (*Open source Field Operation And Manipulation*) is an open source finite volume software for computational fluid dynamics (CFD), owned by the OPENFOAM[®] Foundation and it is licensed exclusively under the GNU General Public Licence (GPL)[2]. That means it is freely available and distributed with the source code. Generally speaking OPENFOAM[®] is a *C++* library that can create executable files, so-called “applications”. Its main task is to solve partial differential equations (PDEs), and ordinary differential equations (ODEs). The applications fall into two categories: solvers and utilities.

- Solvers: created to solve specific problems of continuous mechanics.
- Utilities: created to perform data manipulations.

One of OPENFOAM[®]'s greatest potential is that users have complete access to the source code and they have total freedom to modify existing solvers and share their source code [11] [5]. Furthermore, OPENFOAM[®] is supplied with pre-processing and post-processing environments, for example paraFOAM for the analysis of the data obtained from the simulations. The overall structure of OPENFOAM[®] is shown in Fig.4.1:

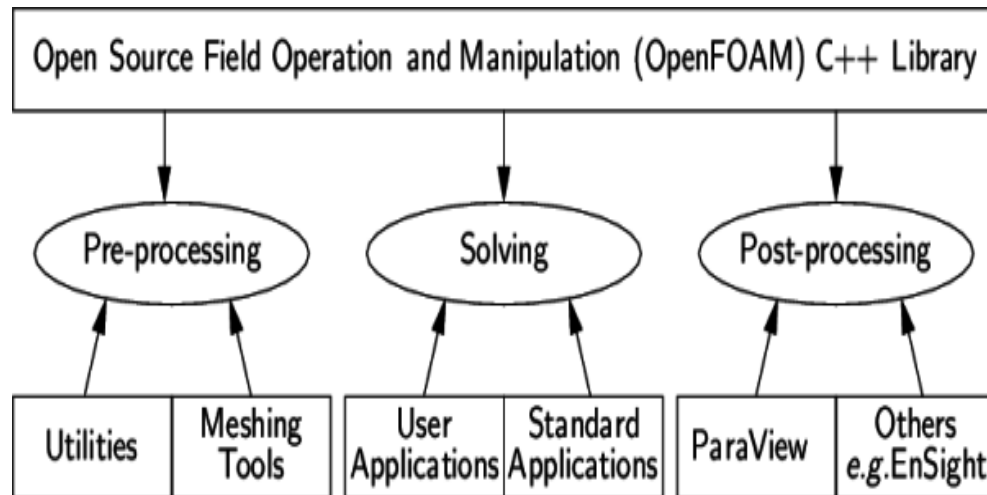


Figure 4.1: *Overview of OpenFOAM structure [2].*

OpenFOAM has extensive multi-physics capabilities, among others:

- Computational fluid dynamics (compressible and incompressible flows);
- Computational heat transfer and conjugate heat transfer;
- Combustion and chemical reactions;
- Multiphase flows and mass transfer;
- Particle methods and lagrangian particle tracking;
- Arbitrary mesh interface, dynamic mesh handling, and adaptive mesh refinement;
- Computational aero-acoustics, computational electromagnetics, computational solid mechanics, etc.

OpenFOAM comes with many physical models, for example:

- Thermophysical models and physical properties for liquids and gases;
- Transport models. Newtonian and non-Newtonian viscosity models;
- Extensive turbulence modeling capabilities (RANS, LES, etc.);
- Lagrangian particle methods;

- Discrete particle modeling;
- VOF (Volume Of Fluid) and Euler-Euler methods for multiphase flows;
- Interphase momentum transfer models for multiphase flows.

4.2 OpenFOAM case structure

The basic directory structure for a OPENFOAM[®] case is reported in *Fig. 4.2*. The roles of the main directories, contained in the case folder, are listed below:

- **System:** it contains the dictionaries to set up the entire solution procedure (from meshing to solving); at least it must contain three files:
 - `fvSchemes` to specify (run-time) the numerical schemes to discretize the equations;
 - `fvSolution` to set equation solvers, tolerances and other algorithm controls;
 - `controlDict` to control (run-time) the simulation run (start/end time, time-step, function objects etc.)
- **Constant:** it contains a folder (`polyMesh`) with the full description of the case mesh and files that specify the physical properties involved (transport and turbulence properties, gravity, dynamic properties etc.)
- **0:** it contains the boundary conditions and the initial conditions of all the primitive variables.

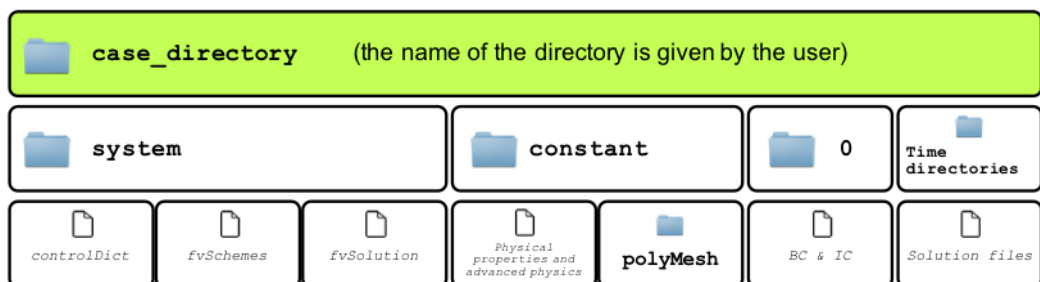


Figure 4.2: *Structure of an OPENFOAM[®] case [2].*

- **Time directories:** it contains the solution and derived fields (these directories are created by the solver based on the saving frequency set initially).

4.3 Simulation workflow: global view

4.3.1 Mesh generation

The mesh generation consists in dividing the physical domain into a finite number of discrete regions, called control volumes or cells, in which the solution is sought (discretization of the domain). It requires three steps:

1. Geometry generation: we first generate the geometry that we are going to feed into the meshing tool;
2. Mesh generation: the mesh can be internal or external. We also define surface and volume refinement regions;
3. Boundary surfaces definition: we define physical surfaces where we are going to apply the boundary conditions (patches).

Fig.4.3 shows a generic and schematic simulation workflow.

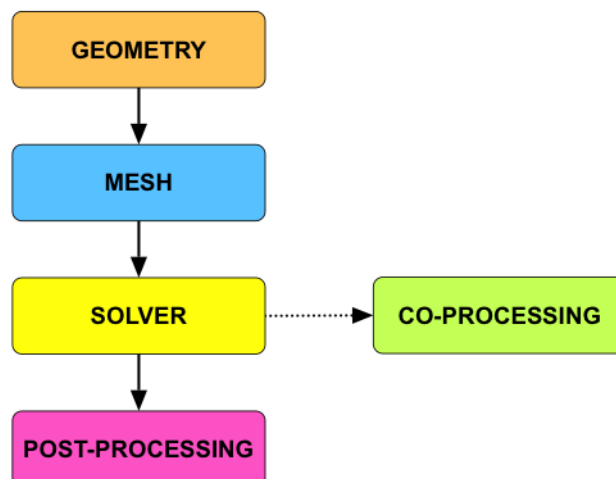


Figure 4.3: *Generic simulation workflow case [2].*

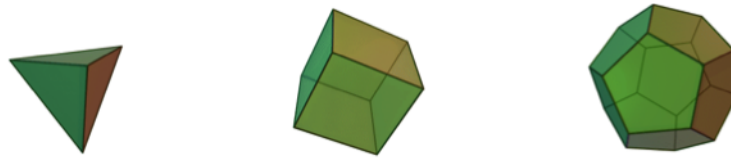


Figure 4.4: *Example of different cell-types [2].*

The most used meshing applications are: blockMesh and SnappyHexMesh. Meshes used in the finite volumes method (FVM) can consist of tetrahedras, pyramids, prisms, hexes, or any mix of these. Each cell type has its very own properties when it comes to approximate the gradients and fluxes. In general, hexahedral meshes will give more accurate solutions. Fig.4.4 shows examples of cells with different geometries:

The cell type depends on the mesh type. The meshes can be structured (meshes are made of hexahedra) or unstructured (meshes are made of mix of all polyhedra). A structured mesh requires as input the blocking definition. For complicated geometries, it can be extremely difficult to arrive to the right blocking and the mesh generation time is quite fast, in the order of second or minutes. Instead, unstructured meshes, only requires as input the element size on the lines and surfaces that define the geometry and the meshing process can be quite time consuming and memory expensive, in order of hours, even days [2].

4.3.2 Mesh quality assessment

No single standard metric exists that can effectively assess the quality of a mesh. A common mesh quality metrics are:

- Orthogonality;
- Skewness;
- Aspect ratio;
- Smoothness.

That, generally, we must keep to a minimum.

Mesh orthogonality: is the angular deviation of the vector \mathbf{S} (located at the face center f) from the vector \mathbf{d} connecting the two cell centers P and N (Fig.4.5). It adds diffusion to the solution and it mainly affects the diffusive terms.

Mesh skewness: is the deviation of the vector \mathbf{d} that connects the two cells P and N , from the face center f . The deviation vector is represented with Δ and f_i is the point where the vector \mathbf{d} intersects the face f (Fig.4.6). It adds diffusion to the solution and affects the convective terms.

Mesh aspect ratio: is the ratio between the longest side Δx and the shortest side Δy (Fig.4.7).

Smoothness: or expansion rate, defines the transition in size between contiguous cells (Fig.4.8). Large transition ratios between cells adds diffusion to the solution. Ideally, the maximum change in mesh spacing should be less than 20%.

In OPENFOAM[®] the mesh quality control is done with the utility checkMesh that look for: mesh stats and overall number of cells of each type; check topology (boundary conditions definitions); check geometry and mesh quality. The utility automatically write the failed sets and saved them in the directory constant/PolyMesh/sets [2].

4.3.3 Standard solvers

The choice of the solver depends on the characteristics of the phenomenon that the user wants to investigate. All the solvers with the OPENFOAM[®] distribution are in the FOAM-SOLVERS directory that us subdivided into several directories by category of continuum mechanics. Some examples of solvers are reported below [2]:

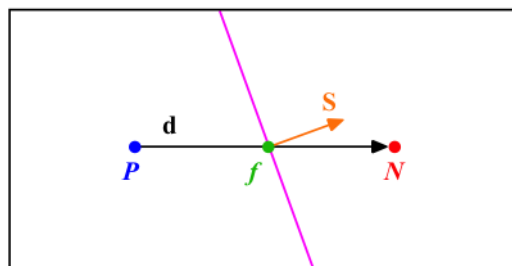


Figure 4.5: *Mesh orthogonality* [2].

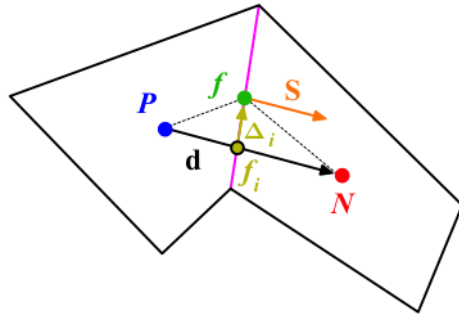


Figure 4.6: *Mesh skewness* [2].

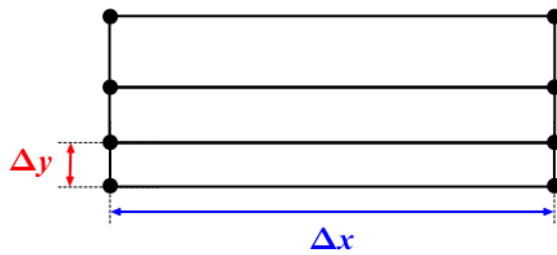


Figure 4.7: *Mesh aspect ratio* [2].

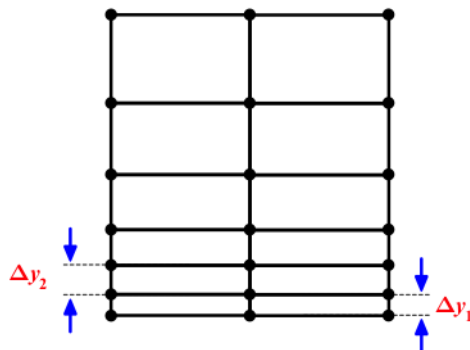


Figure 4.8: *Smoothness* [2].

Incompressible flow:

- icoFoam: transient solver for incompressible, laminar flow of Newtonian fluids.
- nonNewtonianIcoFoam: for non-Newtonian fluids.
- pimpleFoam: large time-step transient solver for incompressible, turbulent flow.
- pisoFoam: transient solver for incompressible, turbulent flow.
- simpleFoam: steady-state solver for incompressible, turbulent flow.

Compressible flow:

- rhoPimpleFoam: transient solver for turbulent flow of compressible fluids.
- rhoSimpleFoam: steady-state solver for turbulent flow of compressible fluids.

Multiphase flow:

- compressibleInterFoam: solver for two compressible, non-isothermal immiscible fluids.
- interFoam: solver for two incompressible, isothermal immiscible fluids.
- twoLiquidMixingFoam: solver for mixing two incompressible fluids.
- twoPhaseEulerFoam: solver for a system of two compressible fluid phases with one phase dispersed.

Heat transfer and buoyancy-driven flows:

- buoyantPimpleFoam: transient solver for buoyant, turbulent flow of compressible fluids for ventilation and heat-transfer.
- buoyantSimpleFoam: steady-state solver for buoyant, turbulent flow of compressible fluids, including radiation, for ventilation and heat-transfer.

Particle-tracking flows:

- `icoUncoupledKinematicParcelFoam`: transient solver for the passive transport of a single kinematic particle cloud.
- `reactingParcelFoam`: transient solver for compressible, turbulent flow with a reacting, multiphase particle cloud.
- `uncoupledKinematicParcelFoam`: transient solver for the passive transport of a particle cloud.

4.3.4 Post-Processing

OPENFOAM[®] is supplied with a post-processing utility, `paraFoam`, that uses ParaView, an open source visualisation application. ParaView uses a tree-based structure in which data can be filtered from the top-level of case module to create sub-modules sets. The strong point is that the user can create a number of sub-modules and display whichever ones they feel to create the desired image or animation. For example, they may add some solid geometry, mesh and velocity vectors, a cutting plane by using different filters [2].

Chapter 5

Methods and equipments

5.1 Design of Experiments

Design of Experiment (DOE) is a set of techniques useful to optimize the number of experiments for the study of the influence of different parameters on the target output variables. Generally, the first step is to identify the independent variables or “input variables” that influence the process, and then study its effects on the dependent variables or “output variables”. For the realization of the experimental planning, the statistical software Design Expert (Stat-Ease, Inc., Minneapolis, United States) was used. In this work the variables identified as inputs were: inlet temperature (indicated with T in or T_{inlet}), feed flow rate, aspiration rate, maltodextrins concentration (Table 5.1); while the parameters considered as output variables were: product recovery, moisture, outlet temperature (indicated with T out or T_{outlet}) and average particle size which definition is reported in the paragraphs 5.2 to 5.5. Response Surface Modeling was employed for data elaboration and the Box-Behnken design was used as logic for the experimental plan. The Fig.5.1 shows an example of a Box-Behnken design with three factors coded into three levels (-1; 0; +1).

Tables 5.2–5.3 show the resulting set of the first experiments (22 runs) that were carried out, reporting the values of the input variables for each test.

Table 5.1: *Input variables values according to the Box-Behnken logic.*

Box- Behnken levels	Temperature inlet [°C]	Maltodextrins concentration [g/L]	Feed flow rate [mL/min]	Aspiration rate [m^3/h]
-1	130	100	5	20
0	145	300	7,5	26
+1	160	500	10	33

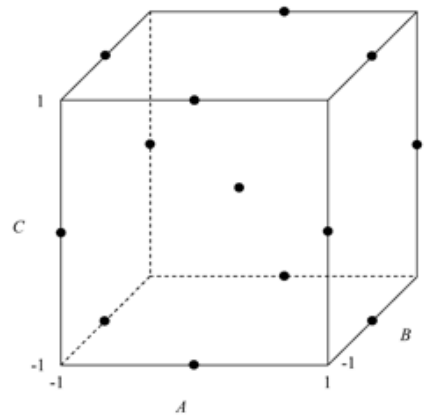
Figure 5.1: *An example of the Box-Behnken design depiction in the design space.*

Table 5.2: Values of the input variables for each test of the experimental plan from run 1 to 10.

Runs	T inlet [°C]	Maltodextrins [g/L]	Feed flow rate [mL/min]	Feed flow rate [%]	Aspiration rate [m^3/h]	Aspiration rate [%]
1	130	100	5	17	20	50
2	160	100	5	17	33	80
3	145	300	7.5	25	26	65
4	130	300	7.5	25	26	65
5	145	300	7.5	25	20	50
6	130	500	5	17	33	80
7	145	500	7.5	25	26	65
8	145	300	7.5	25	26	65
9	130	500	10	33	33	80
10	160	500	5	17	20	50

Note: on the spray dryer, feed flow rate and aspiration rate are expressed in percentage. Above are reported the converted value of rates.

Table 5.3: Values of the input variables for each test of the experimental plan from run 11 to 22.

Runs	T inlet [°C]	Maltodextrins [g/L]	Feed flow rate [mL/min]	Feed flow rate [%]	Aspiration rate [m^3/h]	Aspiration rate [%]
11	145	300	7.5	25	26	65
12	130	100	10	33	20	50
13	160	100	10	33	33	80
14	145	300	7.5	25	33	80
15	160	500	10	33	20	50
16	145	300	5	17	26	65
17	145	300	7.5	25	26	65
18	145	100	7.5	25	26	65
19	160	300	7.5	25	26	65
20	145	300	10	33	26	65
21	145	300	7.5	25	26	65
22	160	100	7.5	25	33	80

The yellow lines indicate the central point of the design space, which was experimentally repeated 5 times, in order to estimate the experimental error.

Statistical significance of the response variables, as functions of the input ones, was established with ANOVA (Analysis of variance). The software determines the main effects of each factor as well as their interactions. Since the relationship that binds the response to the independent variables is unknown, the first step of the RSM consists in the determination of a suitable approximation of the true relationship among the variables. Some example are reported in the equations (5.1),(5.2),(5.3):

$$\text{Linear model: } Y = \beta_0 + \beta_1 X_1 + \beta_2 X_2 + \epsilon \quad (5.1)$$

$$\text{Factorial model: } Y = \beta_0 + \beta_1 X_1 + \beta_2 X_2 + \beta_{12} X_1 X_2 + \epsilon \quad (5.2)$$

$$\text{Quadratic model: } Y = \beta_0 + \beta_1 X_1 + \beta_2 X_2 + \beta_{12} X_1 X_2 + \beta_{11} X_1^2 + \beta_{22} X_2^2 + \epsilon \quad (5.3)$$

Where ϵ represents the noise or error observed in the Y response. By indicating the expected value of the response with $E(Y)$, then the surface represented by $E(Y) = f(X_1, X_2)$ is called the response surface. The parameters β are estimated by the least squares method. Once all the values of the output variables were obtained, a statistical analysis was performed to identify the most significant parameters for the process. Explicating the desire to maximize product recovery and minimize the moisture content, we have seen that the most significant parameters are the concentration of solid and the feed flow rate; if only the humidity was optimized, the recovery of the product would have been too low. From this analysis a new set of experiments was obtained, shown in Table 5.4, testing three values of the two most significant parameters for a total of 9 combinations. The tests, in this second part of the work, were carried out both with the maltodextrin solution in water and with the suspension of calcium carbonate in water.

The green line in the table, corresponding to experiment number 7, has been identified by statistical analysis as the optimal condition. As can be seen from Table 5.4, the inlet temperature and the aspiration rate, which were not found to be significant parameters, were set at a constant value for all the experiments, i.e. $T_{inlet} = 160 \text{ }^\circ\text{C}$, aspiration rate = $27 \text{ m}^3/\text{h}$ (= 68 %).

Table 5.4: *New experimental plan obtained after the optimizing statistical analysis.*

Runs	T inlet [°C]	Solid conc. [g/L]	Feed flow rate [mL/min]	Aspiration rate [m^3/h]
1	160	100	5	27
2	160	100	7,5	27
3	160	100	10	27
4	160	300	5	27
5	160	300	7.5	27
6	160	300	10	27
7	160	500	5	27
8	160	500	7.5	27
9	160	500	10	27

5.2 Spray drying procedure

The Mini Spray Dryer B-290 (BÜCHI-Switzerland), reported in Fig.5.2, was used to perform the drying of the samples. The fed solutions were prepared by adding the maltodextrins (Sigma-Aldrich Chemistry, USA, dextrose equivalent 16.5-19.5) in 50 mL of deionized water (solvent); the sample was stirred until the complete dissolution of maltodextrin was reached. For very concentrated samples the plate was heated for a few seconds to facilitate solubilization. Also as concerns the preparation of calcium carbonate suspension, a final volume of 50 mL of deionized water was used. To avoid carbonate sedimentation, the suspension was continuously stirred during tests.

The factorial plan reported in Tables 5.2-5.3 was performed only on maltodextrin solution, while operating parameters reported in Table 5.4 were used, as described in the previous section 7.1 both for the solution, and the suspension.

The nozzle cleaner value of the spray dryer was set equal to 4 for the tests involving maltodextrins and equal to 7 for calcium carbonate suspension, to avoid nozzle obstruction. Once the drying chamber reached the imposed T_{inlet} , the spray dryer

was started by opening the flow-meter and activating pump. At the end of the test, the T_{outlet} was checked and recorded and the chamber was allowed to cool down to 60 °C before switching off the system.



Figure 5.2: *BÜCHI Mini Spray Dryer B-290.*

5.3 Product recovery

The spray-dried powders were collected from the spray dryer and weighed to calculate the product recovery using equation 5.4:

$$\eta(\%) = \frac{g_{(product)out}}{g_{(product)in}} \cdot 100 \quad (5.4)$$

Where $g_{(product)out}$ = grams of product obtained; $g_{(product)in}$ = grams of product fed.

5.4 Moisture measurement

Capsules were stabilized by putting them in a oven at 110 °C for 1 hour and then, letting them cool in a glass borosilicate desiccator for 25 minutes. After cooling, each capsule was tared and 0,5 g of spray-dried powder were added. After putting the capsules in the oven for 24 hours at 110 °C and then in the desiccator until room temperature was reached, they were weighed to measure the final gross mass. The

test was repeated twice for each sample. The moisture of the sample was expressed as grams of removed water per grams of wet sample, as reported in the equation 5.5:

$$\text{Moisture} \left(\frac{g}{g_{WS}} \right) = \frac{m_{INITIAL} - m_{FINAL}}{m_{INITIAL}} \quad (5.5)$$

where $m_{INITIAL}$ is the net mass (g) of the sample at the beginning, m_{FINAL} is the net mass (g) of the sample after 24 h, and the subscript WS indicate the calculation is based on the initial mass of wet sample.

5.5 Particle size distribution

In order to study the particle size distribution of the sample obtained after the spray drying process, an optical microscope (Olympus IX51) was used. Since the maltodextrins could not be analyzed as such, they were suspended in ethanol and immediately placed on the slide. Ten photos were taken for each sample, which were analyzed by means of ImageJ, an open source software, version 1.51s (National Institute of Health, USA) from which the number of particles for each image and their Feret diameters were obtained. The data were reported on Excel for the determination of the average diameter of each sample. The measurements of the diameters were ordered in ascending order to know the size range. This range was then divided into intervals with constant amplitude and the number of particles included in each size interval was calculated. Fractions based on particle number (x_i) were calculated as in equation 5.6:

$$x_i = \frac{n_i}{n} \quad (5.6)$$

Where n_i is the particles having the diameters in the interval; n is the total number of particles.

The relative frequency (f_i) was calculated dividing the fraction (x_i) by the amplitude of each diameter interval ($d_{i+1}-d_i$), as shown in equation 5.7:

$$f_i = \frac{x_i}{(d_{i+1} - d_i)} \quad (5.7)$$

The corresponding diameter d , of each point of the obtained relative frequency f , was assumed equal to the arithmetic mean of the diameter of each interval. The cumulative function (F_i) was calculated as the summation of the fractions based on particle number of each interval, as expressed by the equation 5.8:

$$F_i = \sum_{j=1}^i x_j \quad (5.8)$$

The mean value of the distribution $\overline{g(d)}$ was determined graphically, being represented by the area under the curve F_i versus $g(d)$ with respect to the F_i axis, which was calculated as expressed in the discretized form of equation 5.9:

$$\overline{g(d)} = \int_0^1 g(d) dF = \sum_k [g(d_k) + g(d_{k-1})] \cdot [F(d_k) - F(d_{k-1})] \cdot \frac{1}{2} \quad (5.9)$$

Chapter 6

Case Study

6.1 Geometry

In previous thesis work on the spray dryer, the geometry chosen for the case studies was taken from the literature or was a specially simplified geometry. In this thesis, the geometry used is the real one of the Mini Spray Dryer B-290 (BÜCHI-Switzerland) used in the laboratory for experimental tests.

In Fig.6.1 the outline of the equipment and its dimensions are presented.

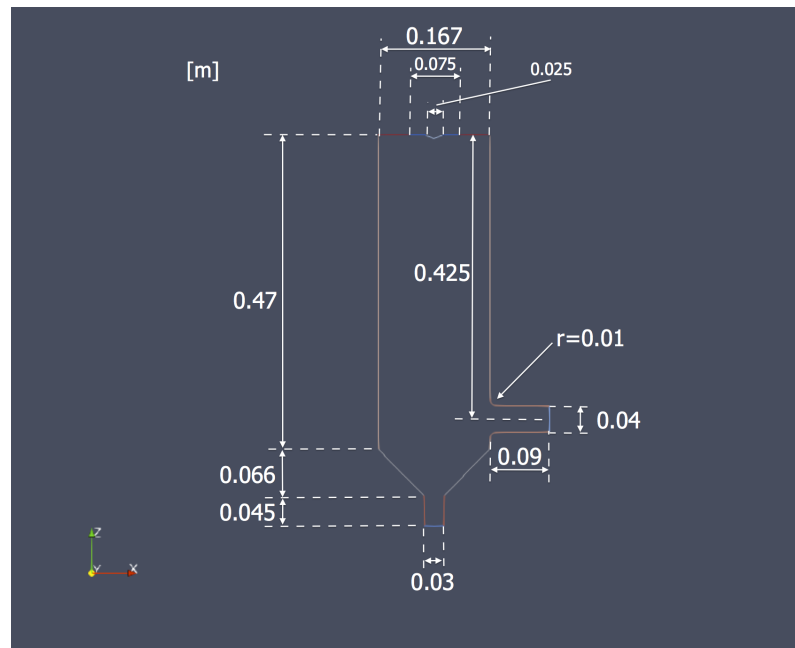


Figure 6.1: Dimension of the Mini Spray Dryer B-290 (BÜCHI-Switzerland).

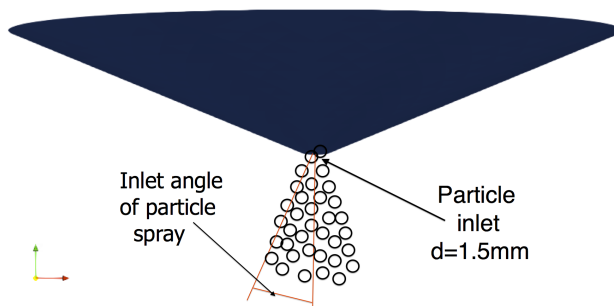


Figure 6.2: *Spraycone and inlet pipe size.*

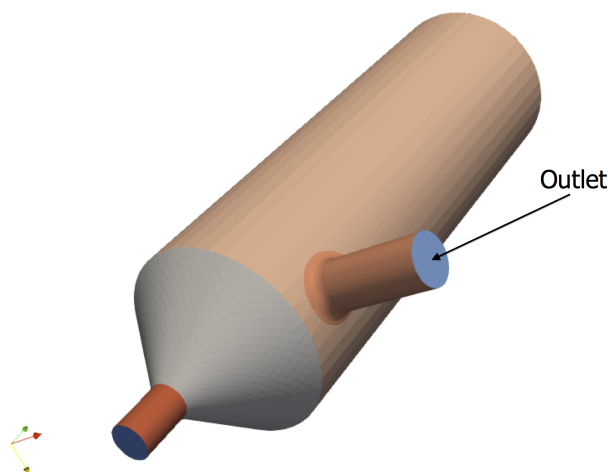


Figure 6.3: *A 3D view of the Spray Dryer's bottom.*

In Fig.6.2 is reported the spraycone with the inlet pipe size, while in Fig.6.3 and Fig.6.4 are reported 3D views of the bottom and of the spray dryer patches.

The Mini Spray Dryer B-290 (BÜCHI-Switzerland), as can be seen from the previous figures, consists of a cylindrical body and a conical bottom in borosilicate glass 3.3. In the upper part of the cylinder there is the two-fluid atomizer which injects the feed conveyed through a small silicone and tygon feeding pipe. While at the end of the cylindrical part there is the outlet pipe that connects the chamber, where the drying takes place, with a cyclone for the product recovery (Fig.5.2). The nozzle is made of stainless steel and the gaskets are made of silicone. Finally,

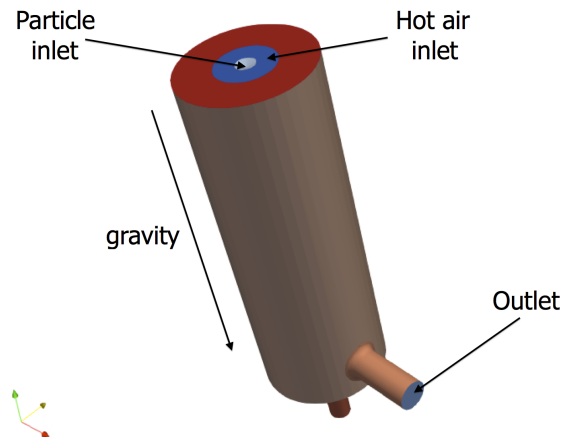


Figure 6.4: A 3D view of the Spray Dryer's patches.

Table 6.1: Geometry dimensions of case study.

Cylinder	Height = 0,47 [m] Diameter = 0,167 [m]
Cone	Height = 0,066 [m] Higher diameter = 0,167 [m] Lower diameter = 0,03 [m]
Inlet	Diameter = 0,1 [m]
Outlet	Diameter = 0,04 [m]

downstream from the process, there is a polyester fabric filter.

The dimensions of the geometry are listed in Table 6.1.

Some dimensions could not be taken directly from the Spray Dryer, therefore approximations were made based on literature data. These measures mainly concern the atomizer which has a very complicated geometry. In particular, a nozzle diameter of 1,5 mm for the particles inlet and a hot air inlet of 75 mm was assumed.

6.2 Case with only the flow

The case concerning only the air flow is here presented. The objective is to compute a statistical steady developed flow that will be the basis for simulations including particles.

The solver: *BuoyantPimpleFoam*

As described within the source code of the solver (freely distributed with the download of OPENFOAM[®]), this is a transient solver for buoyant, turbulent flow of compressible fluids for ventilation and heat transfer. This solver, in addition to the mass conservation and momentum conservation equations in the compressible form (see Chapter 3 for details), also solves the energy equation in terms of enthalpy or internal energy. Therefore, before running the case, we need to define the thermodynamical properties of the working fluid and the temperature field. As a remark about the implementation in OPENFOAM[®] of the momentum conservation equation, the pressure gradient and gravity force terms are rearranged in the following form:

$$\begin{aligned} -\nabla p + \rho \mathbf{g} &= -\nabla(p_{rgh} + \rho \mathbf{g} \cdot \mathbf{r}) + \rho \mathbf{g} \\ &= -\nabla p_{rgh} - (\mathbf{g} \cdot \mathbf{r}) \nabla \rho \end{aligned} \quad (6.1)$$

Where $p_{rgh} = p - \rho \mathbf{g} \cdot \mathbf{r}$ and \mathbf{r} is the position vector. The name of the solver suggests that the *PIMPLE* algorithm is used. *PIMPLE* is one of the pressure based solver for Navier-Stokes equations implemented in OPENFOAM[®]. It is an hybrid between the *SIMPLE* (Semi-Implicit Method for Pressure-Linked Equations) and *PISO* (Pressure Implicit with Splitting Operators) and is formulated for very large timesteps and pseudo-transient simulations [11]. The temporal discretization scheme used for this time dependent simulation is the first order accurate Euler implicit method with adjustable time-step. Implicit numerical methods are unconditionally stable hence the *CFL* number does not have to be bounded under certain low values. However using Euler implicit method doesn't mean that a time step of any size can be chosen. The timestep must be chosen in such a way that it resolves the time-dependent features, and it maintains the solver stability.

However, the maximum CFL number in this simulation was set equal to 1 in order to gain stability and to be able to capture the very transient behaviour of this flux. Moreover, this solver requires the dictionary *thermophysicalProperties* that contains the definition of the physical properties of the working fluid. Within the subdictionary *thermoType*, the thermophysical models is specified. Thermophysical models are concerned with energy, heat and physical properties and they are constructed in OPENFOAM[®] as a pressure-temperature (p - T) system from which other properties are computed. OPENFOAM[®] includes a large set of pre-compiled combinations of modelling, built within the code using C++ templates. This coding approach assembles thermophysical modelling packages beginning with the equation of state and then adding more layers of thermophysical modelling that derive properties from the previous layers [47]. The *thermoType* model used in this thesis is described in the following list:

- *heRhoThermo*: a thermophysical model based on density ρ .
- *const*: a transport model which assumes a constant dynamic viscosity μ and a Prandtl number $Pr = \frac{c_p \mu}{k}$.
- *hConst*: a thermodynamic model which assumes a constant c_p .
- *perfectGas*: it concerns the equation of state of the working fluid. In this case the perfect gas equation is used to compute the density field ρ .
- *sensibleEnthalpy*: it selects the energy variable (enthalpy in this case). The word sensible means that in the (sensible) energy heat of formation is not included

In this configuration, the calculated flow physical variables are the pressure p , the dynamic pressure p_{rgh} , the velocity components U_x , U_y , U_z , the temperature T , the turbulent viscosity ν_T (that is not a physical property), the effective turbulent thermal diffusivity α_T (that is not a physical property). The boundary and initial conditions for all these calculated variables are presented in the next section.

The linear solver, already implemented in OPENFOAM[®], for the solution of the previous variables are really standard. Depending on if the matrix is symmetric (e.g

pressure) or asymmetric (e.g velocity, turbulent kinetic energy, specific dissipation, enthalpy ...) the solvers are:

- GAMG (geometric-algebraic multi-grid) with the smoother Gauss Seidel for symmetric matrices with tolerance 10^{-8}
- SmoothSolver with the smoother symGaussSeidel for symmetric matrices with tolerance 10^{-8}

Initial and Boundary conditions

The geometry is given on *STL* format and this file is composed by different patches:

- *Inlet*: this is the patch through which the hot air enters the computational domain;
- *Outlet*: this is the patch through which the hot air goes out the computational domain;
- *Wall*: this is the patch that includes the surface of the cylinder.

According to this division inside the *STL*, Table 6.2 summarizes the initial and boundary conditions used for this simulation. The *zeroGradient* boundary condition simply extrapolates the quantity to the patch from the nearest cell value by setting the gradient equal to zero for the variable of interest in the direction perpendicular to the boundary. Concerning the dynamic pressure p_{rgh} the boundary condition applied to the wall is *fixedFluxPressure*. This boundary condition adjusts the pressure gradient such that the flux on the boundary is that specified by the velocity boundary condition.

	Walls	Inlet	Outlet
Temperature: \mathbf{T}	- <i>wallHeatTransfer</i> initial value: uniform 300 [K] $T_{ref} = 300$ [K] $\alpha_{Wall} = 1$ [$\frac{W}{m^2}$]	- <i>fixed value</i> value: uniform 433 [K]	- <i>zeroGradient</i>
Thermal diffusivity: α_T	- <i>alphanWallFunction</i> $Pr_T = 0.85$ initial value: uniform 0 [$\frac{Kg}{ms}$]	- <i>calculated</i> initial value: uniform 0 [$\frac{Kg}{ms}$]	- <i>zeroGradient</i>
Turbulent viscosity: ν_T	- <i>nutkWallFunction</i> initial value: Internal field [$\frac{Kg}{ms}$]	- <i>calculated</i> initial value: uniform 0 [$\frac{Kg}{ms}$]	- <i>calculated</i> initial value: uniform 0 [$\frac{Kg}{ms}$]
Velocity: \mathbf{U}	- <i>fixedValue</i> initial value: uniform 0 [$\frac{m}{s}$]	- <i>flowRateInletVelocity</i> volumetric flow rate 0.01 [$\frac{m^3}{s}$] $\rho_{inlet} = 1$ [$\frac{K}{m^3}$]	- <i>zeroGradient</i>
Pressure: p_{rgh}	- <i>fixedFluxPressure</i> initial value: uniform 101325 [Pa]	- <i>zeroGradient</i>	- <i>fixedValue</i> initial value: uniform 101225 [Pa]
Pressure: p	- <i>calculated</i> initial value: uniform 101325 [Pa]	- <i>calculated</i> initial value: uniform 101225 [Pa]	- <i>zeroGradient</i>

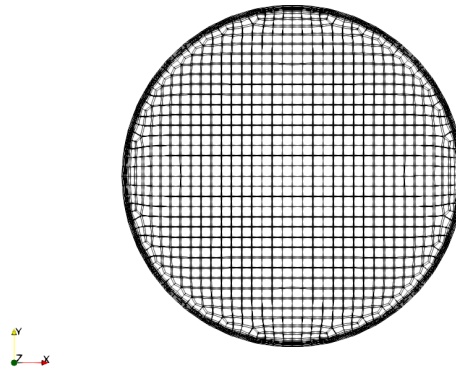
Mesh

The mesh generation utility that has been used is *snappyHexMesh* supplied with OPENFOAM[®]. The *snappyHexMesh* utility generates three-dimensional meshes containing hexahedra and split-hexahedra automatically from triangulated surface geometries, or tri-surfaces, in Stereolithography (STL). The mesh conforms to the surface by refining iteratively an initial mesh, in this case created with the basic *blockMesh* utility and transforming the resulting split-hex mesh to the surface. The mesh quality is controlled by three main parameters that can be extrapolated using the OPENFOAM[®] utility *checkMesh*:

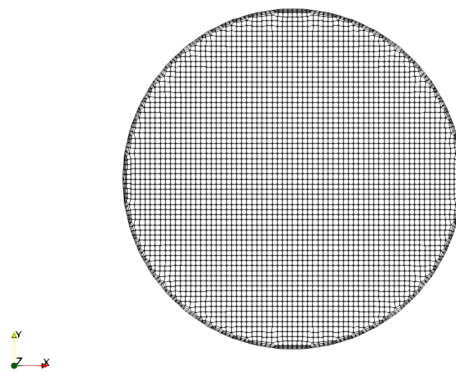
- *Mesh orthogonality*: this parameter is related to angular deviation of the cell face normal vector from the vector connecting two consecutive cell centres. Usually this parameter is kept below 70.
- *Mesh skewness*: skewness is the deviation of the vector that connects two cell centres from the face centres. Usually this parameter is kept below 8.
- *Aspect ratio*: aspect ratio AR is the ratio between the longest side Δx and the shortest side Δy of the cell. Large AR are good if gradients in the largest direction are small.

All these mesh features can be viewed in Chapter 4 in Fig.4.5-4.8.

Two different meshes have been tested in order to perform a convergence study. Fig.6.5 shows a slice of the meshes. Obviously, as the volume of control increases (fineness of the mesh), the computational cost increases and therefore the calculation time increases, but on the other hand more accurate results are obtained both from the qualitative and quantitative point of view. There are two things to keep in mind: one is the simulation Δt that, for the finer mesh is smaller (so this has to do more interactions), the second is the difference over time for the iteration that the computer, which is higher for the refined mesh because there are more cells. Δt for the two meshes is $4.9e-06$ for the refined and $6.25e-06$ for the coarse. The time for the iteration calculated with four processors is 4.65s for the fine mesh and 2s for



(a) Coarse mesh



(b) Fine mesh

Figure 6.5: *Meshes with different refinement levels.*

the coarse one, with these data it turns out that the fine mesh is about three times more expensive than the coarse one.

The main features of the mesh are reported in Tab.6.2.

Table 6.2: *Mesh features.*

	Coarse mesh	Fine mesh
Cells	249455	930438
Hexahedra	237259	918197
Prisms	4576	2840
Pyramids	1998	2732
Tetrahedra	896	1208
Polyhedra	4726	5461
Non-orthogonality	Max = 62,2 Average = 5,3	Max = 58,4 Average = 4,1
Max skewness	1	2,3
Max AR	21,8	7,9

6.3 Particle implementation in OpenFOAM

The model for the two-stage drying process have been implemented and verified in OPENFOAM[®]. In particular the first stage has been verified with the evaporation model existing in *ReactingParcelFoam*. In order to test only the behaviour of the drying process, the same velocity and temperature field have been used when running with *ReactingParcelFoam* and the newly developed version of the drying process.

6.3.1 Background fluid flow field

At this point particles are injected in the computational domain, and their properties are computed through two different Lagrangian solvers:

- *ReactingParcelFoam*: this is a transient solver for compressible, turbulent flow with a reacting, multiphase particles cloud [11].
- *MA_BuoyantKinematicParcelFoam*: this is a new transient solver that uses the model for the drying kinetic.

Let us underline that this solver continues to follow the evolution of the background flow field, hence Eulerian fields are still computed each time step through

the use of the *PIMPLE* algorithm.

6.3.2 OpenFOAM solver: *ReactingParcelFoam*

ReactingParcelFoam is a Lagrangian solver that is able to model several physical processes like combustion, radiation, chemistry reactions and with the inclusion of a Lagrangian cloud of particles. Also this solver requires a *thermophysicalProperties* dictionary that is almost the same used for the previous simulation with *buoyantPimpleFoam* but with some modifications regarding the transport and thermodynamic models which take into account for temperature dependencies of the air dynamic viscosity and specific heat. However, in this case another dictionary named *reactingCloudProperties* for evaporating droplets is required. Inside this dictionary it is possible to find the core of the Lagrangian set up and the parameters that are significant for this thesis are shown in the list below:

- *coupling*: this keyword enables or not the coupling between the continuous and the dispersed phase. For this work the coupling is always set to false and this means that a one-way coupling is performed.
- *interpolationSchemes*: this subdictionary refers to the interpolation scheme between cell centres values and particles-droplets positions. The option *cell*, that assumes cell-centre values constant over the cell, has been used for all variables except the velocity U for which the *cellPoint* option has been chosen; (*cellPoint* concerns with a linear weighted interpolation using cell values).
- *integrationSchemes*: this is related to the integration with time of particles velocity and temperature. By default these are set to Euler for velocity and analytical for temperature.
- *subModels*: In this section it is possible to specify a number of models but the only relevant for this work are those about the forces applied to the particles (*sphereDrag*), the injection inside the domain (*coneInjectionModel*) and the particles interaction with wall (*stick*).

- the *sphereDrag* model imposes a drag coefficient depending on Reynolds particle number.

$$\begin{cases} C_D = 0.424Re & Re > 1000 \\ C_D = 24(1 + \frac{1}{6}Re^{\frac{2}{3}}) & Re < 1000 \end{cases}$$

- *coneInjectionModel*: the *coneInjectionModel* is a multi-point injection model in which users specifies the time of start of injection, the list of injector positions and directions (along injection axes), parcel velocities, inner and outer spray cone angles, parcel diameters also obtained by distribution model and number of parcel to inject per injector. Please, note that parcel means a group of particles, but in this thesis they are imposed as the same.

Table 6.3 summarizes the choices about the main injection parameters. Also in this case, to know some parameters, we had to base on the data found in the literature because it was not possible to obtain them from the experimental tests. For the initial size distribution of the droplets we were able to obtain the granulometric distribution of the initial solid, but it was not possible to obtain a precise measurement of the diameter of the drop that includes the solvent and the solid inside, because we did not have sufficient data in particular the speed of the air entering into the atomizer and its pressure. We hypothesize that the total solid is perfectly mixed with the liquid and therefore, with this hypothesis, supposing that this ratio is also maintained in each drop, we can calculate the size of the solid in each drop.

As a final remark the interactions, such as the collisions between the particles in the dispersed phase, are not taken into account in any cases tested in this thesis.

6.3.3 *MA_BuoyantKinematicParcelFoam*

This solver is a new OPENFOAM[®] application implemented with the purpose to add to the already existing *BuoyantPimpleFoam* solver for the solution of the Eulerian fields, the evolution of a Lagrangian cloud of particles. This allowed us to include the specific evaporation model. OPENFOAM[®] handles the simulation

Table 6.3: *Injection parameters.*

Start of injection (SOI)	0
ParcelPerInjector used in the model	100000/s
ParcelPerInjector calculated for different feed flow rate	5mL/min: $1,273 \cdot 10^6/s$ 7,5mL/min: $1,909 \cdot 10^6/s$ 10mL/min: $2,546 \cdot 10^6/s$
Umag	10 m/s
PositionAxis	(0, 0, 0.579) (0, 0, -1)
thetaInner	0
thetaOuter	76
sizeDistribution	type: fixedValue value = $50 \mu m$

of the particles dynamics reducing as much as possible the interactions with the solution of the fluid equations: the advantage of this choice is that the kind of the underlying fluid simulation has a very little influence on how the particles-classes work. Let us consider now the general case of a time dependent simulation, we can identify these different steps:

- the governing equations of the fluid are solved in a standard way with a given Eulerian time step Δt .
- here the Lagrangian loop starts. To evaluate the new particle position the given Eulerian time step is divided in a certain number of Lagrangian time steps δt . For each Lagrangian time step an interpolation of the Eulerian fields (stored in cell centres) is made in the position of the particle. Then, considering the list of forces acting on the particle, the particle velocity \mathbf{u}_p is evaluated.
- knowing the particle velocity and a given Lagrangian time step an estimation is made for the new particle position \mathbf{x}^* .

$$\mathbf{x}^* = \mathbf{x}(t) + \delta t \mathbf{u}_p(t) \quad (6.2)$$

Here the code checks if the particle crosses a cell boundary. If not, the new

particle position is actually the previous estimation and the Lagrangian time step is definitely fixed.

$$\mathbf{x}(t + \delta t) = \mathbf{x}^* \quad (6.3)$$

If yes, the code performs a series of additional checks (for examples if it is a domain boundary or a partition between different parallel domains) and the effective Lagrangian time step is a fraction of the initial one.

$$\delta t \rightarrow \delta t^* \quad (6.4)$$

$$\mathbf{x}^* = \mathbf{x}_n + \delta t^* \mathbf{u}_p \quad (6.5)$$

- for the new position, the new particle velocity is computed according to the steps described at the beginning of the loop (interpolation of Eulerian fields, evaluation of forces acting on particle).
- until the particle has moved for a time equal to a Eulerian time step (that is the sum of all Lagrangian time steps) the loop is repeated.

The evaporation model is integrated within the Lagrangian loop, precisely after the interpolation of the Eulerian fields to the particle position, when the Lagrangian timestep is fixed. This timestep is used for the time integration of the droplets energy and radius shrinking equations resulting in the evaluation of new droplets diameter, temperature and moisture content.

Here we must make a reference to the equations solved in the two stages drying process. For the first stage the equations solved are from eq.(3.101) to eq.(3.112) (lumped approximation), for the second stage the equation solved is eq.(3.123) (lumped approximation).

Chapter 7

Results

7.1 Design of Experiment Results

The first step of this thesis was, as already mentioned in the paragraph 5, to build the experimental plan using Design-Expert[®] for the study of the influence of the input variables on the output ones.

Tables 7.1 and 7.2 show the first part of experiments that were carried out only with maltodextrins, reporting the values of the output variables for each test.

In particular, the first table shows the value of product recovery and T_{outlet} , while the second table shows the moisture content and the mean diameter of the particles produced.

The results presented in the Tables 7.1 and 7.2 follow what is shown in Table 2.2 regarding the parameter dependencies found in literature. A more precise analysis of the relations between the parameters of the process will be discuss in the following section 7.1.

Once all the values of the output variables were obtained, a statistical analysis with Design-Expert[®] for response surface methodology (RSM) was performed. This class of design is aimed at process optimization and to identify the most significant parameters for the process and their relationship.

The following is the results of the statistical analysis conducted on the maltodextrins solution.

Table 7.1: *Product recovery and T out obtained as functions of the input variables.*

Runs	T in [°C]	Maltodextrin [g/L]	Feed flow rate [mL/min]	Aspiration rate [m³/h]	Product Recovery [%]	T out [°C]
1	130	100	5	50	73,6	66
2	160	100	5	80	84,2	89
3	145	300	7,5	65	54	101
4	130	300	7,5	65	40,13	60
5	145	300	7,5	50	21,53	53
6	130	500	5	80	27,56	64
7	145	500	7,5	65	43,56	58
8	145	300	7,5	65	44,13	58
9	130	500	10	80	32,04	62
10	160	500	5	50	65,48	62
11	145	300	7,5	65	50,6	69
12	130	100	10	50	22,8	40
13	160	100	10	80	67,2	58
14	145	300	7,5	80	67,93	58
15	160	500	10	50	38,52	56
16	145	300	5	65	48,13	61
17	145	300	7,5	65	60,33	56
18	145	100	7,5	65	70	49
19	160	300	7,5	65	58	61
20	145	300	10	65	49,73	49
21	145	300	7,5	65	52,13	56
22	160	100	7,5	80	76,2	66

Table 7.2: *Moisture content and Mean diameter obtained as functions of the input variables.*

Runs	T in [°C]	Maltodextrin [g/L]	Feed flow rate [mL/min]	Aspiration rate [m³/h]	Moisture content [%]	Mean diameter [μm]
1	130	100	5	50	8,07	3,32
2	160	100	5	80	6,19	2,50
3	145	300	7,5	65	5,25	2,77
4	130	300	7,5	65	4,36	2,72
5	145	300	7,5	50	5,18	3,54
6	130	500	5	80	2,99	2,78
7	145	500	7,5	65	3,62	2,23
8	145	300	7,5	65	4,87	4,04
9	130	500	10	80	4,08	2,99
10	160	500	5	50	4,25	3,12
11	145	300	7,5	65	6,06	2,26
12	130	100	10	50	8,20	2,29
13	160	100	10	80	5,47	2,72
14	145	300	7,5	80	5,11	2,95
15	160	500	10	50	5,74	3,16
16	145	300	5	65	3,93	2,66
17	145	300	7,5	65	4,95	2,98
18	145	100	7,5	65	5,09	1,90
19	160	300	7,5	65	4,10	2,46
20	145	300	10	65	5,54	3,36
21	145	300	7,5	65	4,69	3,03
22	160	100	7,5	80	4,41	2,66

- **Response 1: Product recovery**

Table 7.3: ANOVA for Response Surface Reduced two factors interaction model, analysis of variance.

Source	Sum of Squares	df	Mean Square	F Value	p-value Prob > F
Model	5265,06	7	752,15	16,01	<0,0001
A-Tinput	1375,23	1	1375,23	29,27	0,0002
B-Concentration MD	1224,12	1	1224,12	26,05	0,0003
C-Feed flow rate	786,41	1	786,41	16,74	0,0015
D-Aspiration rate	1076,48	1	1076,48	22,91	0,0004
AB	765,63	1	765,63	16,30	0,0016
BC	256,74	1	256,74	5,46	0,0376
CD	532,03	1	532,03	11,32	0,0056
Residual	563,82	12	46,99	-	-
Lack of Fit	430,68	9	47,85	1,08	0,5337
Pure Error	133,14	3	44,38	-	-
Cor Total	5828,88	19	-	-	-

From the Table 7.3 we can see that the “Model F-value” of 16,01 implies the model is significant. There is only a 0,01 % chance that a “Model F-Value” this large could occur due to noise. Values of “Prob > F” less than 0,0500 indicate model terms are significant. In this case A, B, C, D, AB, BC, CD are significant model terms. Values greater than 0,1000 indicate the model terms are not significant. The “Lack of Fit F-value” of 1,08 implies the “Lack of Fit” is not significant relative to the pure error. There is a 53,37 % chance that a “Lack of Fit F-value” this large could occur due to noise. Non-significant “Lack of Fit” is good to fit the model.

As reported in Table 7.4 the “R-Squared” statistics are very good near to 1. The “Pred R-Squared” of 0,7127 is in reasonable agreement with the “Adjusted R-Squared” of 0,8468. “Adeq Precision” measures the signal to noise ratio. A ratio greater than 4 is desirable. So, this model can be used to navigate the design space.

Table 7.4: *Post-ANOVA statistics for Response 1.*

Standard Deviation	6,85	R-Squared	0,9033
Mean	50,88	Adjusted R-Squared	0,8468
C.V.%	13,47	Predicted R-Squared	0,7127
PRESS	1674,88	Adeq. Precision	13,128

Table 7.5: *Model's coefficients for Response 1.*

Factor	Coefficient Estimate	df	Standard Error	95% CI Low	95% CI High	VIF
Intercept	50,88	1	1,53	47,54	54,22	-
A-T input	11,73	1	2,17	7,00	16,45	1
B-Concentration MD	-11,06	1	2,17	-15,79	-6,43	1
C-Feed flow rate	-8,87	1	2,17	-13,59	-4,15	1
D-Aspiration rate	23,20	1	4,85	12,64	33,76	5
AB	21,88	1	5,42	10,07	33,68	5
BC	5,67	1	2,42	0,38	10,95	1
CD	8,15	1	2,42	2,87	13,44	1

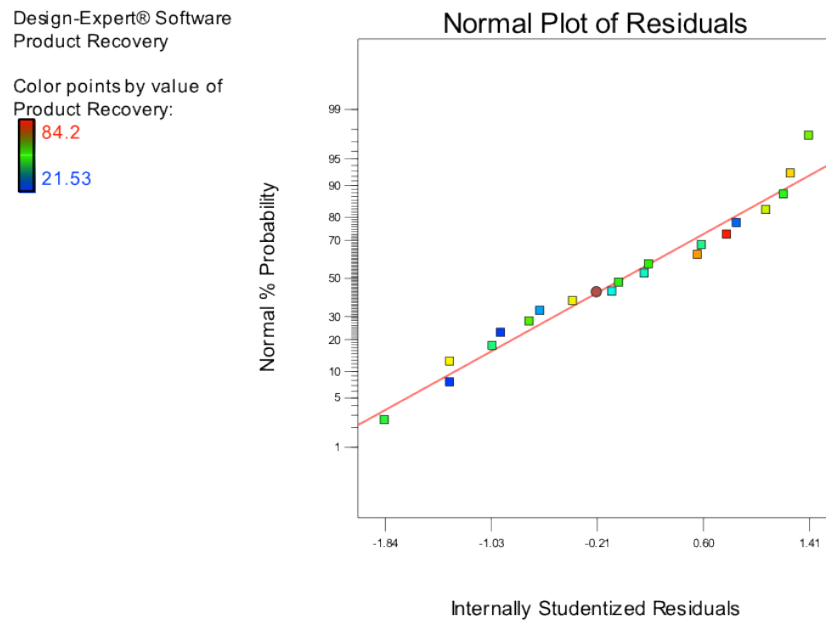


Figure 7.1: Normal probability plot of the residuals for Response 1.

The terms reported in Table 7.5 can be used to interpolate the results of the experiments.

The final equation in terms of Coded Factors is the following:

$$\begin{aligned}
 \text{Product Recovery} = & +50,88 + 11,73 \cdot A - 11,06 \cdot B - 8,87 \cdot C + 23,20 \cdot D + \\
 & + 21,88 \cdot A \cdot B + 5,67 \cdot B \cdot C + 8,15 \cdot C \cdot D.
 \end{aligned}
 \tag{7.1}$$

The Diagnostic Plots are shown from Fig.7.2 to Fig.7.4.

Normal plot of residual is used to confirm the normality assumption. Data points should be approximately linear. A non-linear pattern (such as an S-shaped curve) indicates non-normality in the error term, which may be corrected by a transformation. In this case, data plotted in Fig.7.1 exhibits normal behavior, so it's safe to assume the normality of the phenomenon described by the experimental points.

The graph of internally studentized residuals versus predicted values reported in Fig.7.2 is used to confirm the constant variance assumption. The size of the

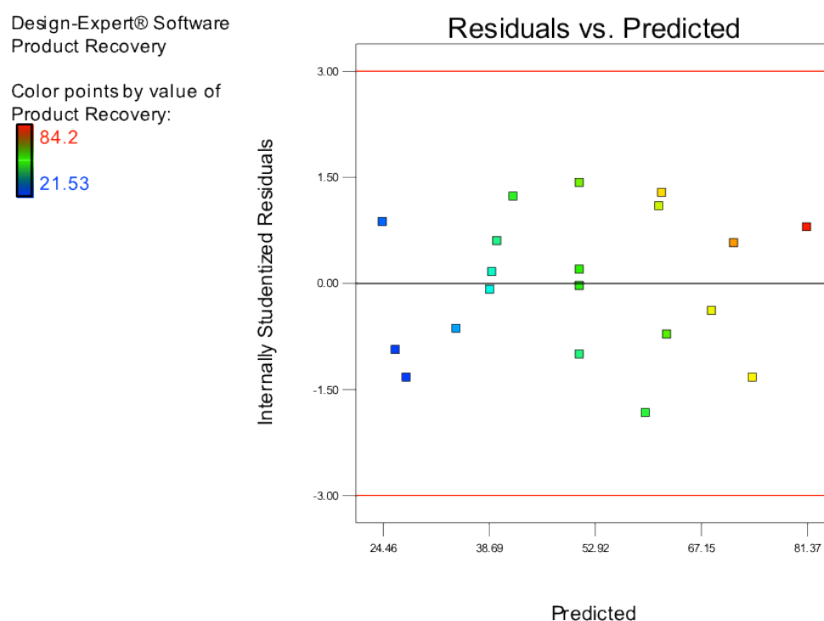


Figure 7.2: *Internally Studentized Residuals versus predicted values for Response 1.*

residuals should be independent of the size of the predicted values. The points have a random arrangement so the conditions of ANOVA are respected.

The externally studentized residuals versus run reported in Fig.7.3 is used to identify model and data problems by highlighting outliers: values outside the red limits. In this case, there aren't outliers.

The Box-Cox plot tells whether a transformation of the data may help. As reported in Fig.7.4 the recommended transform is none.

At this point, to really understand how the response varies according to the two factors chosen, the figures of the 3-D visualization of the response surfaces are reported in Fig.7.5-7.6-7.7.

From the Fig.7.5 it can be seen that the product recovery increases as the aspiration rate increases and that decreases with the increase of the feed flow rate for low aspiration rate value. This dependency of the product recovery weakens with the aspiration rate growing, becoming non-influential.

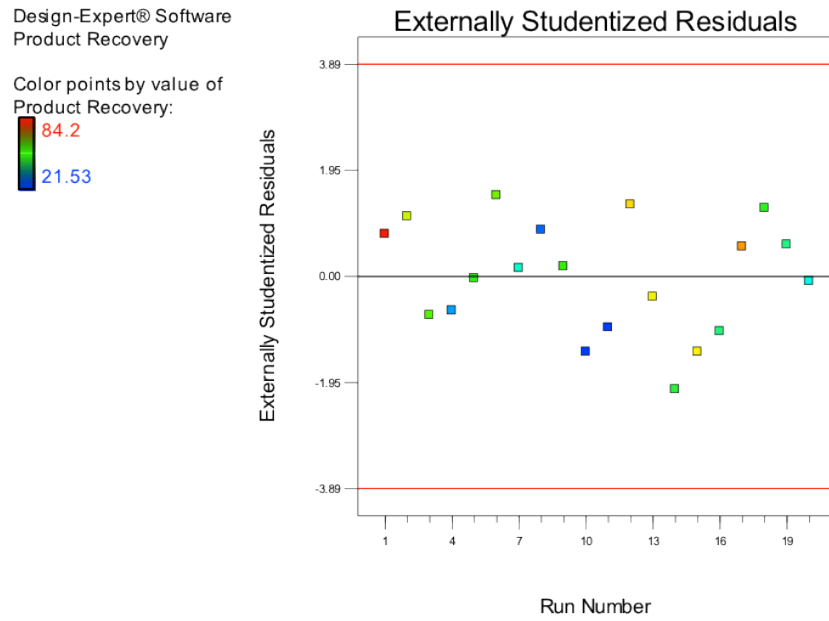


Figure 7.3: *Externally Studentized Residuals versus run for Response 1.*

As can be seen in Fig.7.6 as the variables (concentration and input temperature) are going to the extreme of the field the recovery increases, making a saddle point for variables value in the center of the experimental range.

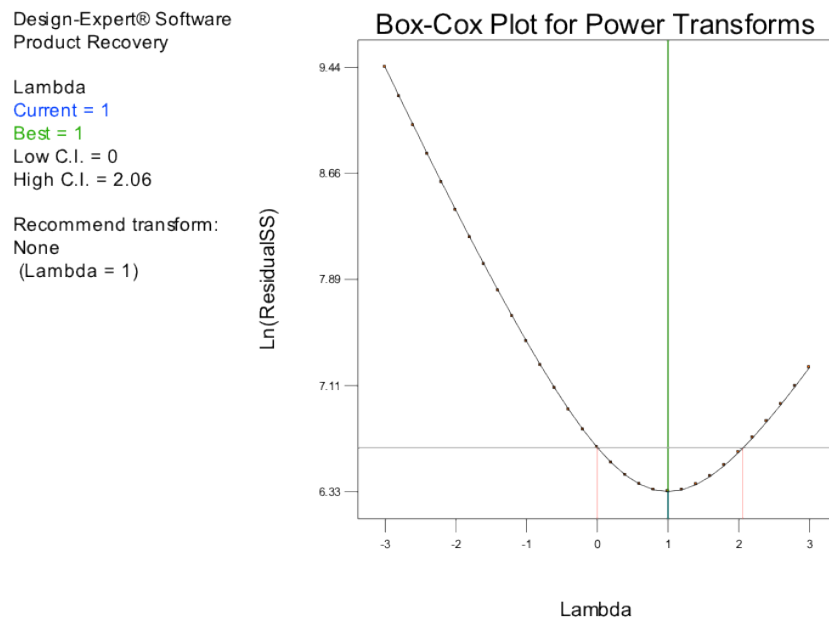


Figure 7.4: *Box-Cox plot for Response 1.*

The same trend of Fig.7.5 with respect to the concentration and feed flow rate can also be seen from Fig.7.7. The following Tables 7.6-7.7 show the diagnostic report for the product recovery obtained from the statistical analysis.

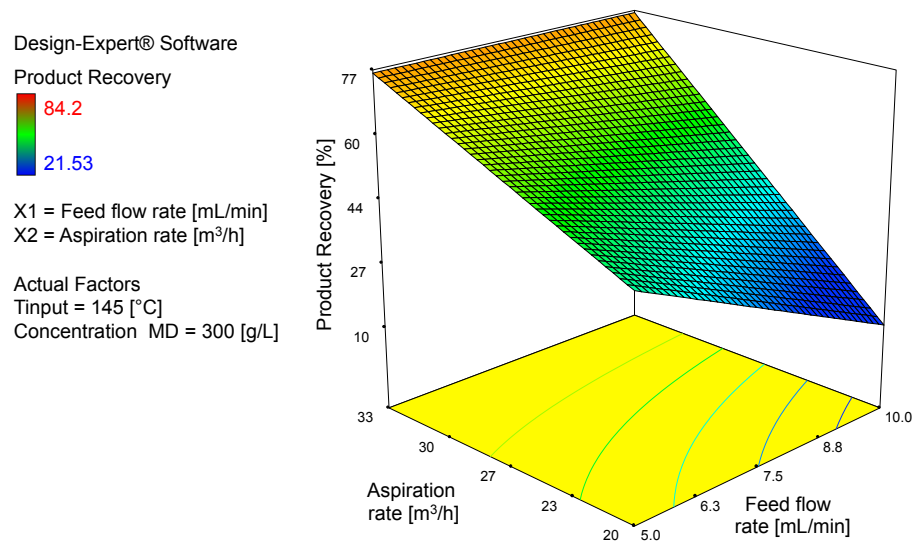


Figure 7.5: 3D response surface plot with T_{input} and Concentration fixed.

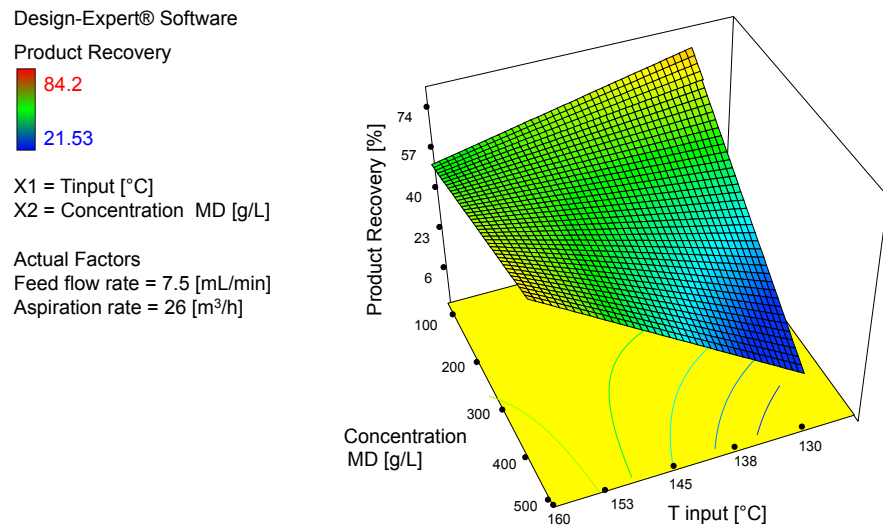


Figure 7.6: 3D response surface plot with Feed flow rate and Aspiration rate fixed.

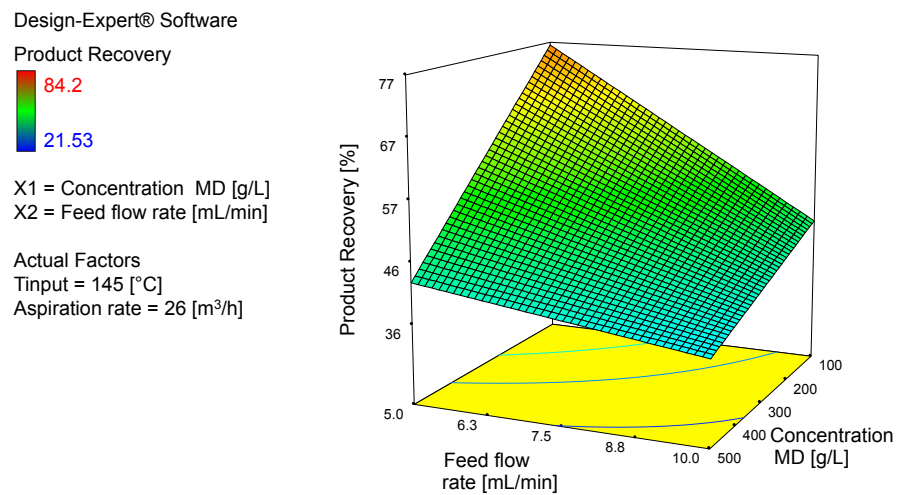


Figure 7.7: 3D response surface plot with T_{input} and Aspiration rate fixed.

Table 7.6: *Diagnostic Report for Response 1 (Run 1-10).*

Run Order	Actual Value	Predicted Value	Residual	Leverage	Internally Studentized Residual	Externally Studentized Residual	Cook's Distance	Influence on Fitted Value DFFITS	Standard Order
1	38,52	38,86	-0,34	0,725	-0,095	-0,091	-0,147	0,003	20
2	65,48	61,58	3,90	0,725	1,086	1,095	1,778	0,389	2
3	67,20	68,62	-1,42	0,725	-0,394	-0,380	-0,617	0,051	13
4	27,56	24,46	3,10	0,725	0,862	0,852	1,383	0,245	8
5	84,20	81,37	2,83	0,725	0,786	0,773	1,255	0,204	1
6	22,80	26,20	-3,40	0,725	-0,947	-0,943	-1,530	0,296	11
7	32,04	34,37	-2,33	0,725	-0,647	-0,631	-1,024	0,138	4
8	73,60	71,58	2,02	0,725	0,562	0,545	0,885	0,104	17
9	40,13	29,15	0,98	0,150	0,155	0,148	0,062	0,001	7
10	58,00	62,61	-4,61	0,150	-0,729	-0,714	-0,300	0,012	3

Table 7.7: Diagnostic Report for Response 1 (Run 11-20).

Run Order	Actual Value	Predicted Value	Residual	Leverage	Internally Studentized Residual	Externally Studentized Residual	Cook's Distance	Influence on Fitted Value DFFITS	Standard Order
11	70,00	61,94	8,06	0,150	1,275	1,313	0,551	0,036	12
12	43,56	39,82	3,74	0,150	0,592	0,576	0,242	0,008	19
13	48,13	59,75	-11,62	0,150	-1,838	-2,077	-0,872	0,075	14
14	49,73	42,01	7,72	0,150	1,221	1,250	0,525	0,033	18
15	21,53	27,68	-6,15	0,550	-1,337	-1,388	-1,535	0,273	10
16	67,93	74,08	-6,15	0,550	-1,337	-1,388	-1,535	0,273	15
17	50,60	50,88	-0,28	0,050	-0,042	-0,040	-0,009	0,000	5
18	52,13	50,88	1,25	0,050	0,187	0,179	0,041	0,000	9
19	60,33	50,88	9,45	0,050	1,414	1,484	0,340	0,013	6
20	44,13	50,88	-6,75	0,050	-1,010	-1,011	-0,232	0,007	16

- **Response 2: Moisture**

Table 7.8: ANOVA for Response Surface Reduced Quadratic Model, analysis of variance.

Source	Sum of Squares	df	Mean Square	F Value	p-value Prob > F
Model	21,43	8	2,68	28,91	<0,0001
A-Tinput	0,053	1	0,053	0,58	0,4641
B-Concentration MD	9,18	1	9,18	99,06	<0,0001
C-Feed flow rate	4,04	1	4,04	43,66	<0,0001
D-Aspiration rate	3,837e-003	1	3,837e-003	0,041	0,8425
AB	0,89	1	0,89	9,58	0,0102
AC	0,35	1	0,35	3,76	0,0785
CD	0,76	1	0,76	8,23	0,0153
D ²	2,06	1	2,06	22,23	0,0006
Residual	1,02	11	0,093	-	-
Lack of Fit	0,97	8	0,12	7,46	0,0630
Pure Error	0,049	3	0,016	-	-
Cor Total	22,45	19	-	-	-

The “Model F-value” of 28,91 implies the model is significant (Table 7.8). There is only a 0,01 % chance that a “Model F-Value” this large could occur due to noise. Values of “Prob > F” less than 0,0500 indicate model terms are significant. In this case B, C, AB, CD, D^2 are significant model terms. Values greater than 0,1000 indicate the model terms are not significant. The “Lack of Fit F-value” of 7,46 implies there is a 6,30 % chance that a “Lack of Fit F-value” this large could occur due to noise.

The “Pred R-Squared” of 0,8754 is in reasonable agreement with the “Adjusted R-Squared” of 0,9216. “Adeq Precision” measures the signal to noise ratio. A ratio of 25,384 indicates an adequate signal. Also in this case, the model choice can be used to navigate the design space.

The final equation in terms of Coded Factors is the following 7.2:

Table 7.9: *Post-ANOVA statistics for Response 2.*

Standard Deviation	0,30	R-Squared	0,9546
Mean	4,93	Adj. R-Squared	0,9216
C.V.%	6,17	Pred. R-Squared	0,8754
PRESS	2,80	Adeq. Precision	25,384

Table 7.10: *Model's coefficients for Response 2.*

Factor	Coefficient Estimate	df	Standard Error	95% CI Low	95% CI High	VIF
Intercept	4,61	1	0,096	4,40	4,82	-
A-T input	-0,073	1	0,096	-0,28	0,14	1
B-Concentration MD	-0,96	1	0,096	-1,17	-0,75	1
C-Feed flow rate	0,64	1	0,096	0,42	0,85	1
D-Aspiration rate	-0,044	1	0,22	-0,52	0,43	5
AB	0,74	1	0,24	0,22	1,27	5
AC	-0,21	1	0,11	-0,45	0,028	1
CD	-0,31	1	0,11	-0,55	-0,072	1
D²	0,64	1	0,14	0,34	0,94	1

$$\begin{aligned} \text{Moisture} = & +4,61 - 0,073 \cdot A - 0,96 \cdot B + 0,64 \cdot C - 0,044 \cdot D + \\ & + 0,74 \cdot A \cdot B - 0,21 \cdot A \cdot C - 0,31 \cdot C \cdot D + 0,64 \cdot D^2 \end{aligned} \quad (7.2)$$

In Fig.7.8-7.11 the diagnostic plots for which the same considerations apply for the product recovery are reported.

The distribution of data points in Fig.7.8 can still be considered linear.

The points in Fig.7.9 have a random arrangement so the conditions of ANOVA are respected, even if less than in the previous case of product recovery.

Also in this case reported in Fig.7.10 there aren't outliers.

As reported in Fig.7.11 the recommended transform is none as it can be seen by λ value = 1.

From Fig.7.12 it can be seen that the moisture decreases as the concentration increases. The dependence on T_{input} changes with the concentration: at low concentration the dependence is negative (i.e. high T_{input} , low moisture) that is what can be expected, while at high concentration the dependence is positive. This behavior should be caused by the developing by the maltodextrin agglomerate of a sort of shell that makes the water diffusion in the solid more difficult. Fig.7.13 shows the same behavior with the feed flow rate in place of the concentration.

Fig.7.13 shows that the moisture increases as the feed flow rate increases.

While, from Fig.7.14 it can be seen that the optimum value for aspiration rate, corresponding at the local minimum of the surface, that will be around the central value of aspiration rate. In particular for this experiment the global minimum (i.e. the best value) of moisture is for value of aspiration rate and feed flow rate of 26,5 m³/h and 5 mL/min respectively.

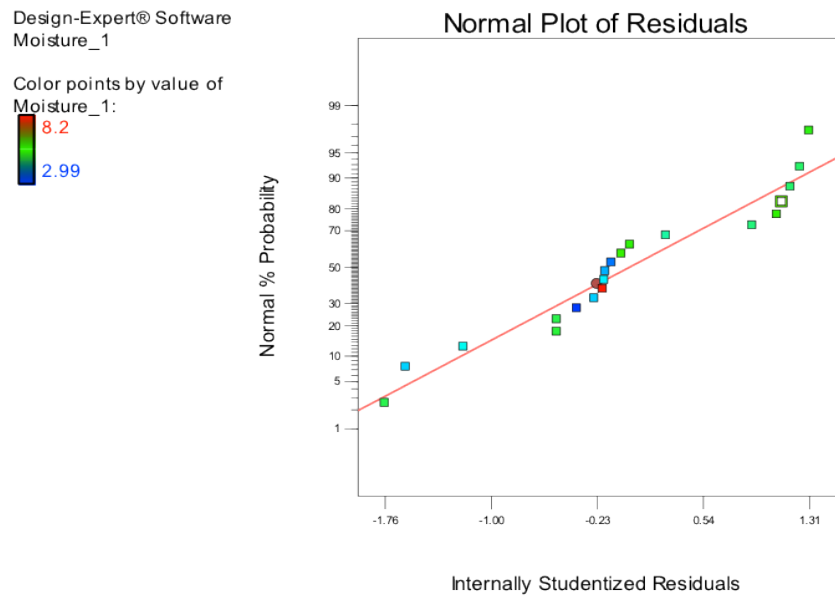


Figure 7.8: Normal probability plot of the residuals for Response 2.

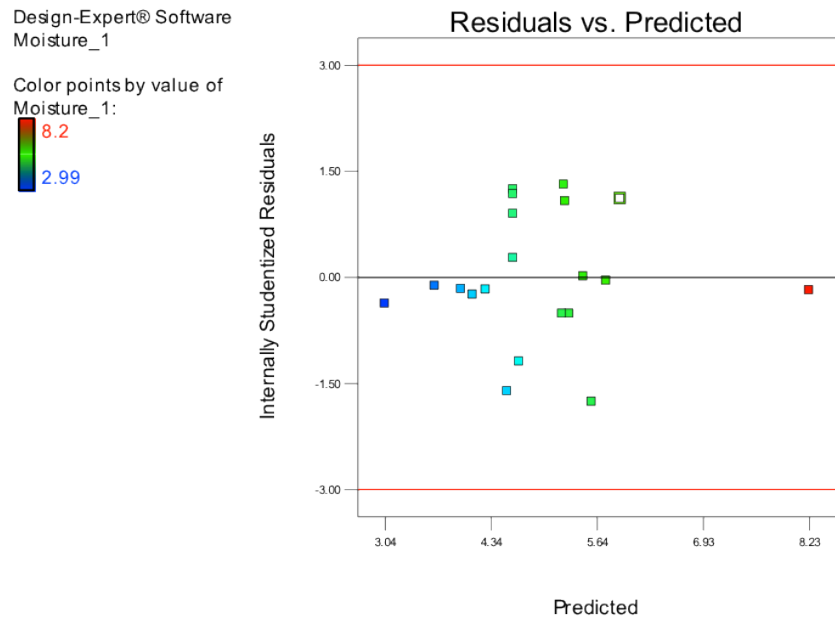


Figure 7.9: Internally Studentized Residuals versus predicted values for Response 2.

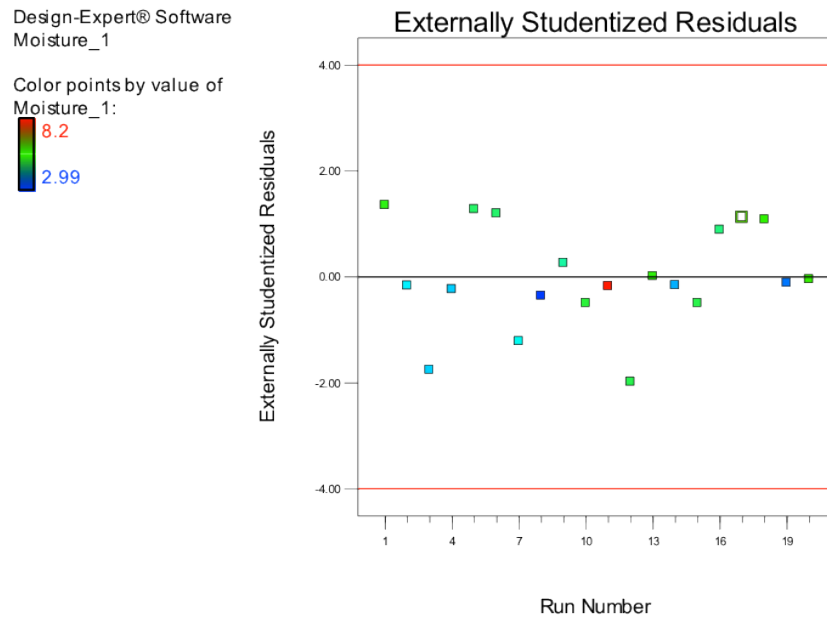


Figure 7.10: *Externally Studentized Residuals versus run for Response 2.*

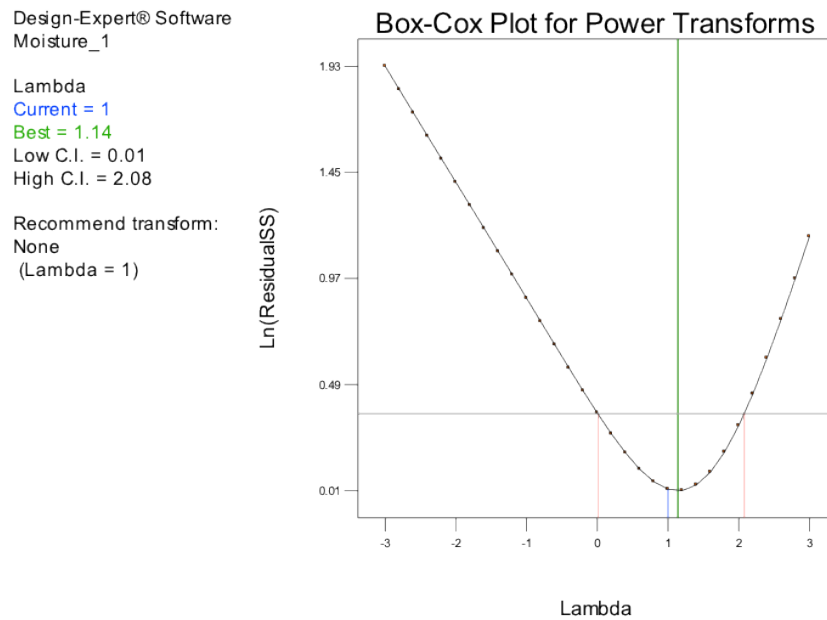


Figure 7.11: *Box-Cox plot for Response 2.*

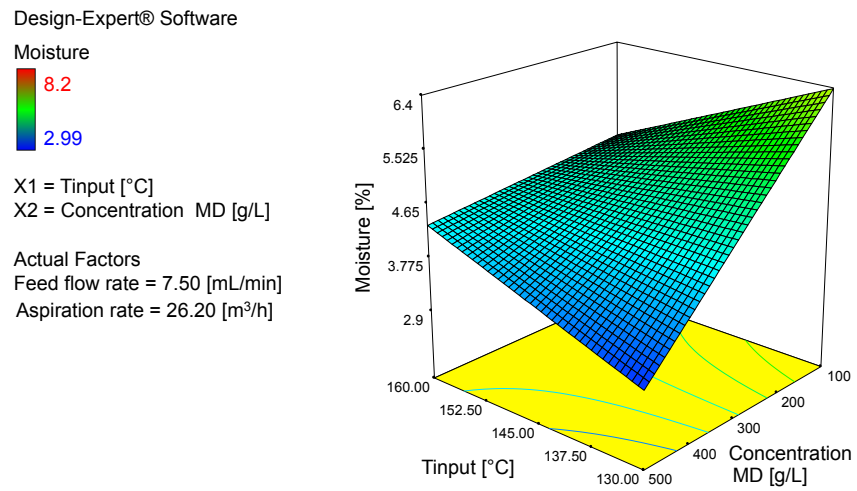


Figure 7.12: 3D response surface plot with Feed flow rate and Aspiration rate fixed.

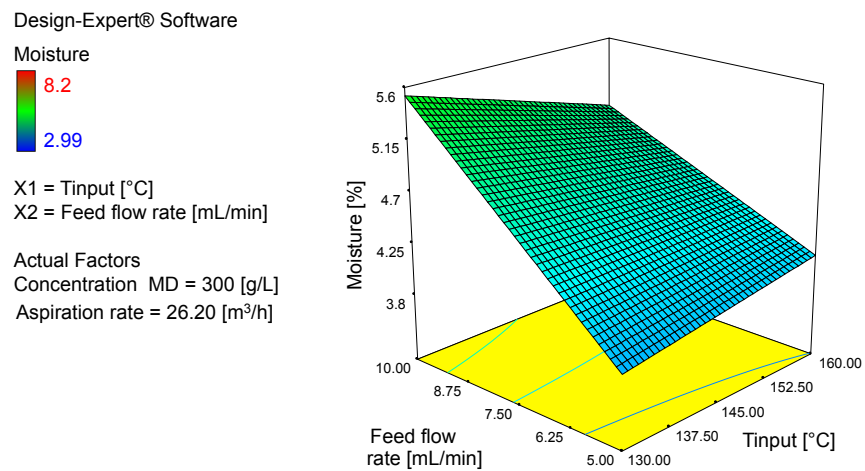


Figure 7.13: 3D response surface plot with Concentration and Aspiration rate fixed.

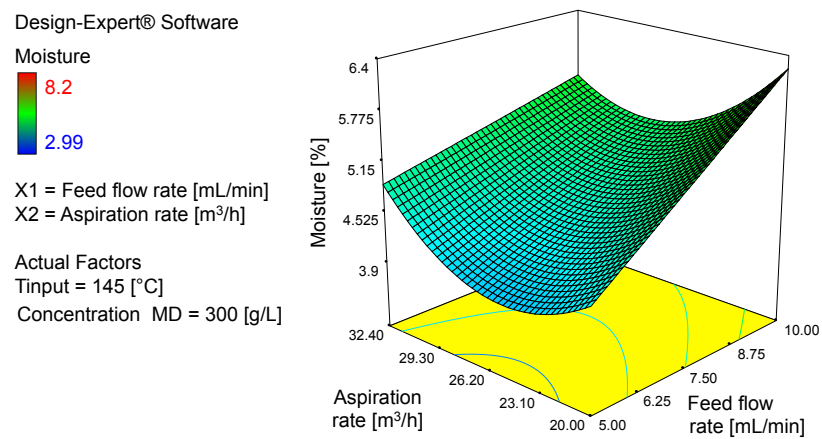


Figure 7.14: 3D response surface plot with T input e Concentration fixed.

Table 7.11: *Diagnostic Report Response 2 (Run 1-10).*

Run Order	Actual Value	Predicted Value	Residual	Leverage	Internally Studentized Residual	Externally Studentized Residual	Cook's Distance	Influence on Fitted Value DFFITS	Standard Order
1	5,74	5,75	-7,51e-003	0,775	-0,052	-0,050	-0,092	0,001	20
2	4,25	4,28	-0,026	0,775	-0,177	-0,169	-0,313	0,012	2
3	5,47	5,47	1,49e-003	0,775	0,010	0,010	0,018	0,000	13
4	2,99	3,04	-0,054	0,775	-0,374	-0,359	-0,666	0,054	8
5	5,42	5,23	0,19	0,775	1,306	1,354	2,51	0,652	1
6	8,20	8,23	-0,027	0,775	-0,187	-0,179	-0,332	0,013	11
7	4,08	4,12	-0,036	0,775	-0,249	-0,238	-0,443	0,024	4
8	6,08	5,92	0,16	0,775	1,108	1,121	2,08	0,470	17
9	4,36	4,69	-0,33	0,200	-1,194	-1,220	-0,610	0,040	7
10	4,10	4,54	-0,44	0,200	-1,613	-1,759	-0,880	0,072	3

Table 7.12: Diagnostic Report for Response 2 (Run 11-20).

Run Order	Actual Value	Predicted Value	Residual	Leverage	Internally Studentized Residual	Externally Studentized Residual	Cook's Distance	Influence on Fitted Value DFFITS	Standard Order
11	5,09	5,57	-0,48	0,200	-1,763	-1,985	-0,992	0,086	12
12	3,62	3,65	-0,034	0,200	-0,125	-0,119	-0,060	0,000	19
13	3,93	3,98	-0,046	0,200	-0,169	-0,161	-0,081	0,001	14
14	5,54	5,25	0,29	0,200	1,073	1,081	0,540	0,032	18
15	5,20	5,30	-0,100	0,600	-0,519	-0,501	-0,614	0,045	10
16	5,11	5,21	-0,100	0,600	-0,519	-0,501	-0,614	0,045	15
17	4,97	4,61	0,36	0,100	1,240	1,274	0,425	0,019	5
18	4,69	4,61	0,078	0,100	0,270	0,258	0,086	0,001	9
19	4,95	4,61	0,34	0,100	1,171	1,193	0,398	0,017	6
20	4,87	4,61	0,26	0,100	0,893	0,885	0,295	0,010	16

- **Response 3: T outlet**

Table 7.13: ANOVA for Response Surface Reduced Linear Model, analysis of variance.

Source	Sum of Squares	df	Mean Square	F Value	p-value Prob >F
Model	1,045e-003	2	5,226e-004	9,63	0,0016
C-Feed flow rate	7,019e-004	1	7,019e-004	12,94	0,0022
D-Aspiration rate	3,432e-004	1	3,432e-004	6,33	0,0222
Residual	9,222e-004	17	5,424e-005	-	-
Lack of Fit	8,019e-004	14	5,728e-005	1,43	0,4323
Pure Error	1,202e-004	3	4,009e-005	-	-
Cor Total	1,967e-003	19	-	-	-

The “Model F-value” of 9,63 implies the model is significant. There is only a 0,16 % chance that a “Model F-Value” this large could occur due to noise. Values of “Prob > F” less than 0,0500 indicate model terms are significant. In this case C, D are significant model terms. The “Lack of Fit F-value” of 1,43 implies the “Lack of Fit” is not significant relative to the pure error. There is a 43,23 % chance that a “Lack of Fit F-value” this large could occur due to noise. Non-significant “Lack of Fit” is good to fit the model.

The “Pred R-Squared” of 0,2775 is in reasonable agreement with the “Adjusted R-Squared” of 0,4761. “Adeq Precision” measures the signal to noise ratio. A ratio of 9,982 indicates an adequate signal, in fact, a ratio greater than 4 is desirable. This model can be used to navigate the design space.

The final equation in terms of Coded Factors is:

Table 7.14: Post-ANOVA statistics for Response 3.

Standard Deviation	7,365e-003	R-Squared	0,5312
Mean	0,13	Adj. R-Squared	0,4761
C.V.%	5,62	Pred. R-Squared	0,2775
PRESS	1,421e-003	Adeq. Precision	9,982

Table 7.15: Model's coefficients for Response 3.

Factor	Coefficient Estimate	df	Standard Error	95% CI Low	95% CI High	VIF
Intercept	0,13	1	1,647e-003	0,13	0,13	-
C-Feed flow rate	8,378e-003	1	2,329e-003	3,464e-003	0,013	1
D-Aspiration rate	-5,858e-003	1	2,329e-003	-0,011	-9,445e-004	1

$$\frac{1}{\text{Sqrt}(T_{out})} = +0,13 + 8,378e^{-003} \cdot C - 5,858e^{-003} \cdot D. \quad (7.3)$$

The Diagnostic Plots are shown in Figs.7.15-7.18.

Design-Expert® Software
1.0/Sqrt(Tout)

Color points by value of
1.0/Sqrt(Tout):

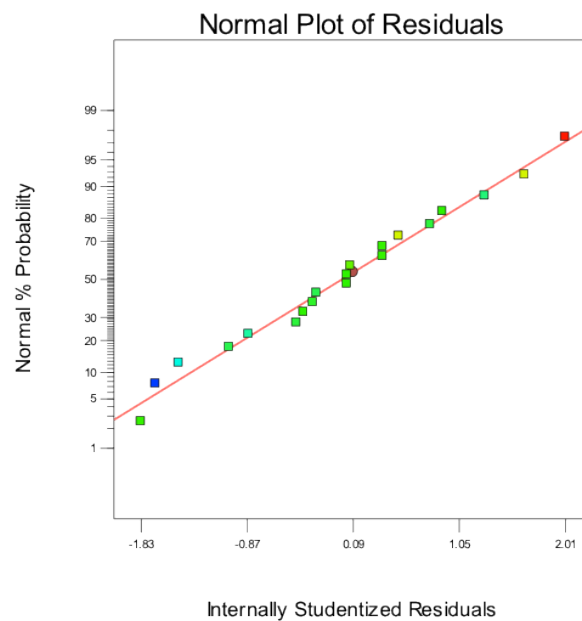
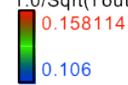


Figure 7.15: Normal probability plot of the residuals for Response 3.

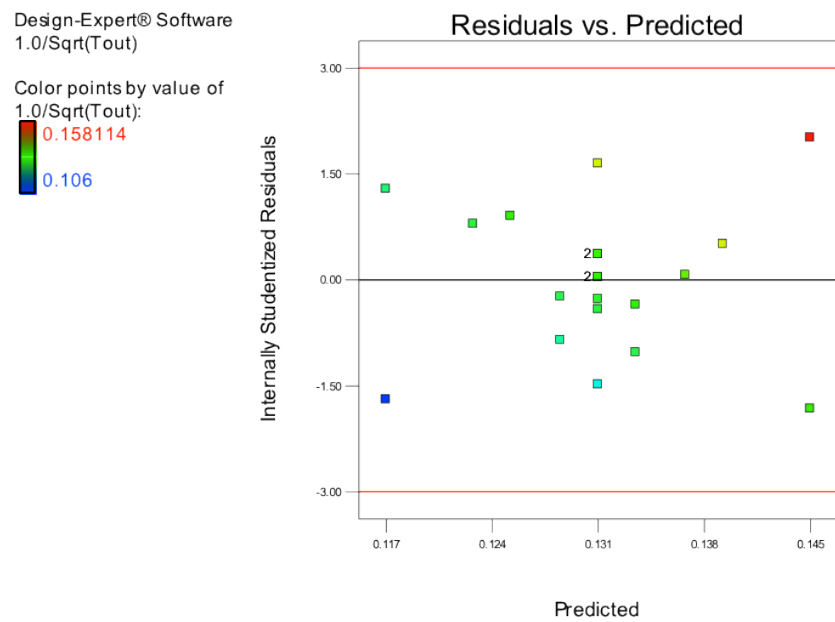


Figure 7.16: Internally Studentized Residuals versus predicted values for Response 3.

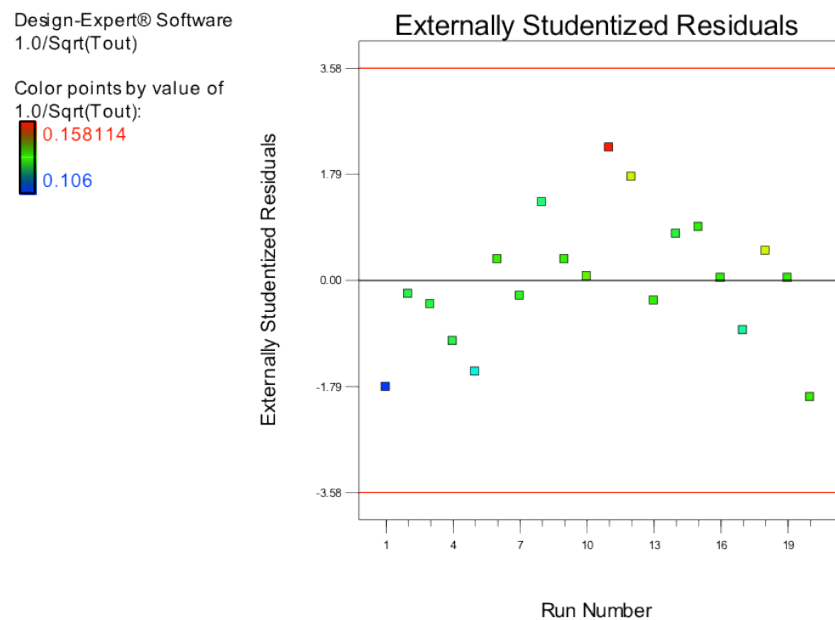


Figure 7.17: Externally Studentized Residuals versus run for Response 3.

Design-Expert® Software
1.0/Sqrt(Tout)

Lambda
Current = -0.5
Best = -0.23
Low C.I. = -1.88
High C.I. = 1.37

Recommend transform:
None
(Lambda = 1)

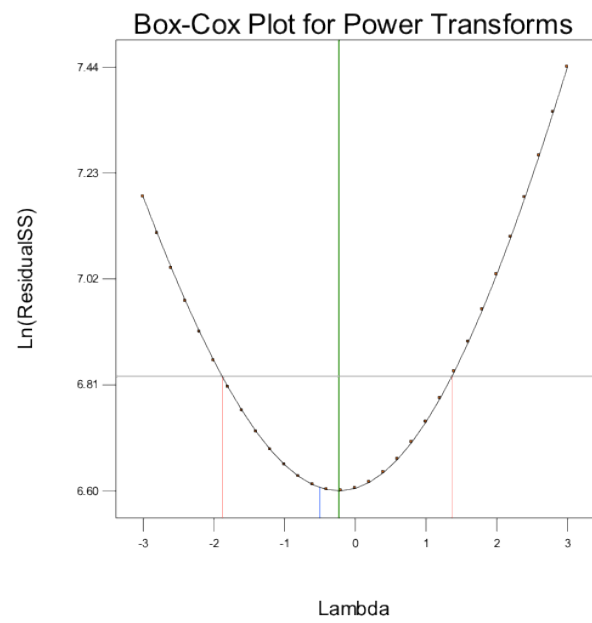


Figure 7.18: *Box-Cox plot for Response 3.*

Table 7.16: *Diagnostic Report for Response 3 (Run 1-10).*

Run Order	Actual Value	Predicted Value	Residual	Leverage	Internally Studentized Residual	Externally Studentized Residual	Cook's Distance	Influence on Fitted Value DFFITS	Standard Order
1	0,13	0,15	-0,012	0,250	-1,827	-1,977	-1,142	0,371	20
2	0,13	0,13	-1,528e-003	0,250	-0,240	-0,233	-0,314	0,006	2
3	0,13	0,13	-2,261e-003	0,250	-0,354	-0,345	-0,199	0,014	13
4	0,13	0,12	8,189e-003	0,250	1,284	1,311	0,757	0,183	8
5	0,11	0,12	-0,011	0,250	-1,695	-1,804	-1,042	0,319	1
6	0,16	0,15	0,013	0,250	2,011	2,235	1,291	0,450	11
7	0,13	0,13	-6,567e-003	0,250	-1,030	-1,032	-0,596	0,118	4
8	0,12	0,13	-5,437e-003	0,250	-0,852	-0,845	-0,488	0,081	17
9	0,13	0,13	-1,948e-003	0,050	-0,271	-0,264	-0,610	0,001	7
10	0,13	0,13	-3,011e-003	0,050	-0,419	-0,409	-0,094	0,003	3

Table 7.17: Diagnostic Report for Response 3 (Run 11-20).

Run Order	Actual Value	Predicted Value	Residual	Leverage	Internally Studentized Residual	Externally Studentized Residual	Cook's Distance	Influence on Fitted Value DFFITS	Standard Order
11	0,14	0,13	0,012	0,050	1,645	1,740	0,399	0,047	12
12	0,13	0,13	2,586e-004	0,050	0,036	0,035	0,008	0,000	19
13	0,13	0,12	5,367e-003	0,150	0,790	0,781	0,328	0,037	14
14	0,14	0,14	3,431e-003	0,150	0,505	0,494	0,208	0,015	18
15	0,14	0,14	4,543e-004	0,150	0,067	0,065	0,027	0,000	10
16	0,13	0,13	6,117e-003	0,150	0,901	0,896	0,376	0,048	15
17	0,12	0,13	-0,011	0,050	-1,485	-1,545	-0,354	0,039	5
18	0,13	0,13	2,583e-003	0,050	0,360	0,350	0,080	0,002	9
19	0,13	0,13	2,583e-003	0,050	0,360	0,350	0,080	0,002	6
20	0,13	0,13	2,586e-004	0,050	0,036	0,035	0,008	0,000	16

- **Response 4: Mean Diameter**

Table 7.18: *ANOVA for Response Surface Reduced Mean Model, analysis of variance.*

Source	Sum of Squares	df	Mean Square	F Value	p-value Prob >F
Model	0,000	0	-	-	-
Residual	3,43	19	0,18	-	-
Lack of Fit	3,06	16	0,19	1,54	0,4042
Pure Error	0,37	3	0,12	-	-
Cor Total	3,43	19	-	-	-

Values of “Prob > F” less than 0,0500 indicate model terms are significant. In this case there are no significant model terms. Values greater than 0,1000 indicate the model terms are not significant. The “Lack of Fit F-value” of 1,54 implies the “Lack of Fit” is not significant relative to the pure error. There is a 40,42 % chance that a “Lack of Fit F-value” this large could occur due to noise. “Lack of fit” is non-significant so is good to fit the model.

A negative “Pred R-Squared” implies that the overall mean is a better predictor of this response.

Table 7.19: *Post-ANOVA statistics for Response 4.*

Standard Deviation	0,42	R-Squared	0,0000
Mean	2,79	Adj. R-Squared	0,0000
C.V.%	15,25	Pred. R-Squared	-0,1080
PRESS	3,80	Adeq. Precision	-

Table 7.20: *Model’s coefficients for Response 4.*

Factor	Coefficient Estimate	df	Standard Error	95% CI Low	95% CI High
Intercept	2,79	1	0,095	2,59	2,99

The final equation 7.4 in terms of Coded Factors shows that the average diameter is a constant parameter.

$$\text{MeanDiameter} = 2,79\mu\text{m} \quad (7.4)$$

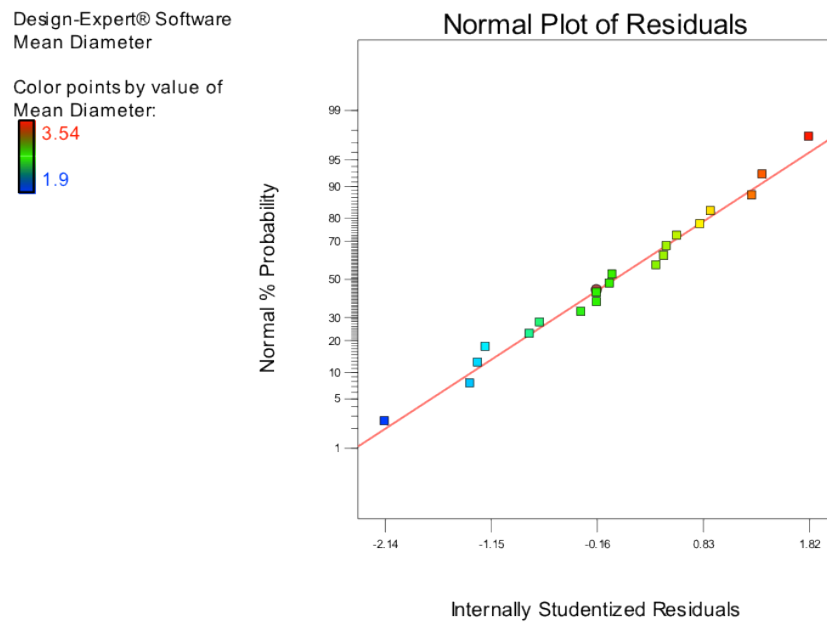


Figure 7.19: Normal probability plot of the residuals for Response 4.

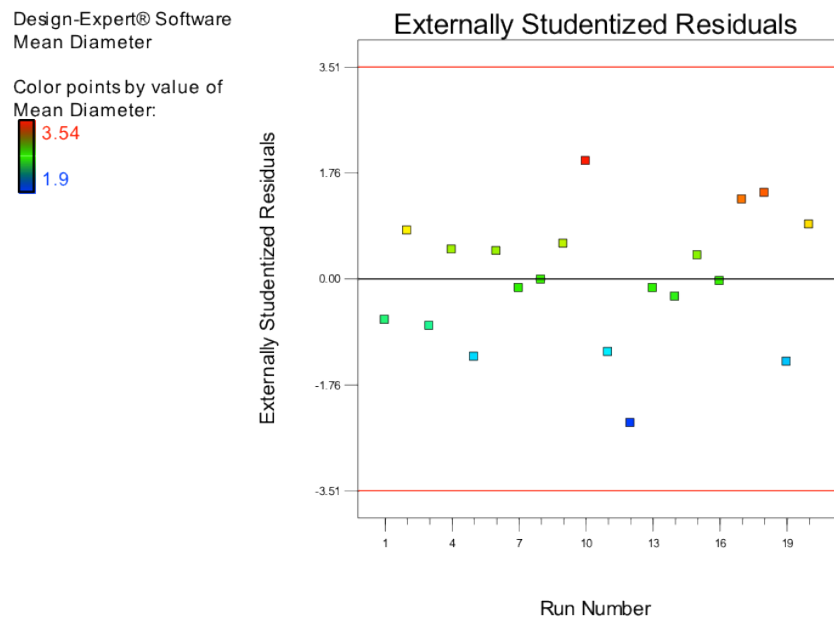


Figure 7.20: *Externally Studentized Residuals versus predicted values for Response 4.*

Table 7.21: Diagnostic Report for Response 4 (Run 1-10).

Run Order	Actual Value	Predicted Value	Residual	Leverage	Internally Studentized Residual	Externally Studentized Residual	Cook's Distance	Influence on Fitted Value DFFITS	Standard Order
1	3,16	2,79	0,37	0,050	0,901	0,896	0,206	0,043	20
2	3,12	2,79	0,33	0,050	0,804	0,796	0,183	0,034	2
3	2,72	2,79	-0,067	0,050	-0,162	-0,158	-0,036	0,001	13
4	2,78	2,79	-7,000e-003	0,050	-0,017	-0,016	-0,004	0,000	8
5	2,50	2,79	-0,29	0,050	-0,693	-0,683	-0,157	0,025	1
6	2,29	2,79	-0,50	0,050	-1,200	-1,215	-0,279	0,076	11
7	2,99	2,79	0,20	0,050	0,490	0,480	0,110	0,013	4
8	3,32	2,79	0,53	0,050	1,287	1,311	0,301	0,087	17
9	2,72	2,79	-0,067	0,050	-0,162	-0,158	-0,036	0,001	7
10	2,46	2,79	-0,33	0,050	-0,790	-0,781	-0,1790	0,033	3

Table 7.22: Diagnostic Report for Response 4 (Run 11-20).

Run Order	Actual Value	Predicted Value	Residual	Leverage	Internally Studentized Residual	Externally Studentized Residual	Cook's Distance	Influence on Fitted Value DFFITS	Standard Order
11	1,90	2,79	-0,89	0,050	-2,142	-2,394	-0,549	0,241	12
12	2,23	2,79	-0,56	0,050	-1,345	-1,376	-0,316	0,095	19
13	2,66	2,79	-0,13	0,050	-0,307	-0,299	-0,069	0,005	14
14	3,36	2,79	0,57	0,050	1,384	1,420	0,326	0,101	18
15	3,54	2,79	0,75	0,050	1,818	1,947	0,447	0,174	10
16	2,95	2,79	0,16	0,050	0,394	0,385	0,088	0,008	15
17	2,26	2,79	-0,53	0,050	-1,273	-1,295	-0,297	0,085	5
18	3,03	2,79	0,24	0,050	0,587	0,576	0,132	0,018	9
19	2,98	2,79	0,19	0,050	0,466	0,456	0,105	0,011	6
20	2,77	2,79	-0,017	0,050	-0,041	-0,040	-0,009	0,000	16

As regards the measurement of diameters, as mentioned in paragraph 5.5, the ImageJ software, to analyze the photos taken with optical microscope, was used. The following Fig.7.21 shows two examples related to experiment number 1 and 8 that have different inlet parameters. In particular the figure shows two images taken from the sample of maltodextrins and its cumulative functions.

From experiment number 1 solid particles have been obtained with a diameter between 1 and 28 μm , the highest concentration of particles fell in the 2-4 μm range, for which a mean diameter of 3,32 μm has been obtained. While from experiment number 8, the total range was 1-9 μm with the highest concentration between 4-5 μm and a mean diameter of 4,02 μm . Averaging all the mean diameters obtained for the 22 experiments a mean diameter of the maltodextrin particles of 2,97 μm was obtained; these measures are however subject to uncertainty.

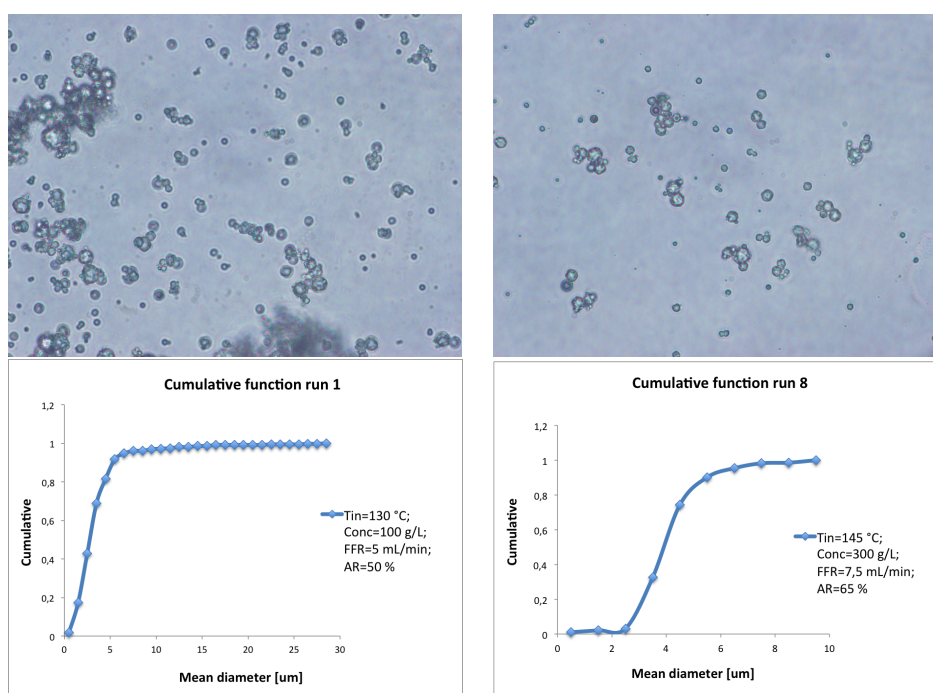


Figure 7.21: *Particles produced by experiment 1 and 8 and related cumulative functions.*

7.1.1 Optimization tests Results

As already mentioned in the paragraph 5, explicating the desire to maximize product recovery and minimize the moisture content, it was been discussed how the most significant parameters are the concentration of solid and the feed flow rate and, in this way, a new set of experiments was obtained. Tables 7.23-7.24 and Tables 7.25-7.26 report the results obtained for the new series of experiments conducted both on the solution and, this time, on the suspension of calcium carbonate.

Table 7.23: *Product recovery and T out obtained as functions of the input variables for new experimental plan with solution.*

Runs	T in [°C]	Maltodextrin [g/L]	Feed flow rate [mL/min]	Aspiration rate [m³/h]	Product Recovery [%]	T out [°C]
1	160	100	5	68	76,6	84
2	160	100	7,5	68	66,8	72
3	160	100	10	68	73,8	68
4	160	300	5	68	77,2	82
5	160	300	7,5	68	76	74
6	160	300	10	68	61,66	73
7	160	500	5	68	71	91
8	160	500	7,5	68	61,67	85
9	160	500	10	68	57	77

As the analysis of the previous data set showed that the average particle diameter was not a significant parameter for the optimization of moisture content and yield, for this new data set the measurement was made only for cases used in simulations, i.e. 25g/50ml, 15g/50ml, 5g/50ml and feed flow rate 5ml/min. The average diameter of calcium carbonate particles was also investigated before being processed, in order to have an estimate of the initial size of the solid, an estimate that, in the future, could be used to determine a more realistic droplet size compared to 50 μm used in simulations, for more details, refer to 6.3. For the case 25g/50ml the mean diameter is resulted 2,95 μm ; for the case 15g/50ml: 4 μm ; for the case 5g/50ml: 2,79 μm .

Table 7.24: *Moisture content obtained as function of the input variables for new experimental plan with solution.*

Runs	T in [°C]	Maltodextrin [g/L]	Feed flow rate [mL/min]	Aspiration rate [%]	Moisture content [%]
1	160	100	5	68	4,63
2	160	100	7,5	68	3,47
3	160	100	10	68	4,54
4	160	300	5	68	2,18
5	160	300	7,5	68	2,36
6	160	300	10	68	1,94
7	160	500	5	68	1,53
8	160	500	7,5	68	1,80
9	160	500	10	68	1,69

Table 7.25: *Product recovery and T out obtained as functions of the input variables for new experimental plan with suspension.*

Runs	T in [°C]	CaCO ₃ [g/L]	Feed flow rate [mL/min]	Aspiration rate [m ³ /h]	Product Recovery [%]	T out [°C]
1	160	100	5	68	78,4	85
2	160	100	7,5	68	76,6	78
3	160	100	10	68	76,8	78
4	160	300	5	68	70	86
5	160	300	7,5	68	62,66	79
6	160	300	10	68	62,46	83
7	160	500	5	68	71	87
8	160	500	7,5	68	62,64	79
9	160	500	10	68	69	75

Table 7.26: *Moisture content obtained as function of the input variables for new experimental plan with solution.*

Runs	T in [°C]	CaCO₃ [g/L]	Feed flow rate [mL/min]	Aspiration rate [%]	Moisture content [%]
1	160	100	5	68	0,13
2	160	100	7,5	68	0,12
3	160	100	10	68	0,22
4	160	300	5	68	0,20
5	160	300	7,5	68	0,13
6	160	300	10	68	0,18
7	160	500	5	68	0,11
8	160	500	7,5	68	0,14
9	160	500	10	68	0,20

Calcium carbonate showed an initial mean diameter of 4,70 μm .

7.2 Flow case

In this section we present the results obtained from the numerical model. To ensure that the solution is independent from the grid resolution, two different meshes have been tested, a coarse and a fine, respectively. A convergence study is always needed for CFD simulations but it can involve high computational costs, especially for cases similar to the one studied in this work where the physical simulated time is long. In the present case the flow is highly three-dimensional, time dependent and turbulent, see Fig. 7.22. For this reason a stationary solutions will not be found. We define, instead, a converge solution when the mean values of the velocity and temperature fields do not change. To have an idea of the order of magnitude of the computational time, the case with the coarser mesh needed 20 days to reach convergence, but with the finest mesh it took almost 3 months. To test the effect of grid refinement, we present velocity contours in Fig.7.23 realized by taking a section at $z = 0,3$ m. We note that the z -component of the velocity is an order of magnitude large than the other two components. This is the central jet coming from the inlet and this causes the large dynamics of the current setup. Since the other two velocity components are tranverse to the first one, they will have smaller scales and smaller magnitudes. For this reason it will take a longer time for the x - and y components of the velocity to converge. Indeed, it can be seen in Fig. 7.23 that the z -components computed using the course and fine grids are similar while the other two are not. In Fig.7.24 a vertical cut, in the x - z plane, is shown for both grids. Here, the vertical jet is evident.

However the background fluid flow is not the main objective of this work and, also because of the high computational costs, we decided not to further refine the mesh and to take the last solution with the coarse one as the starting point for the simulation with particles.

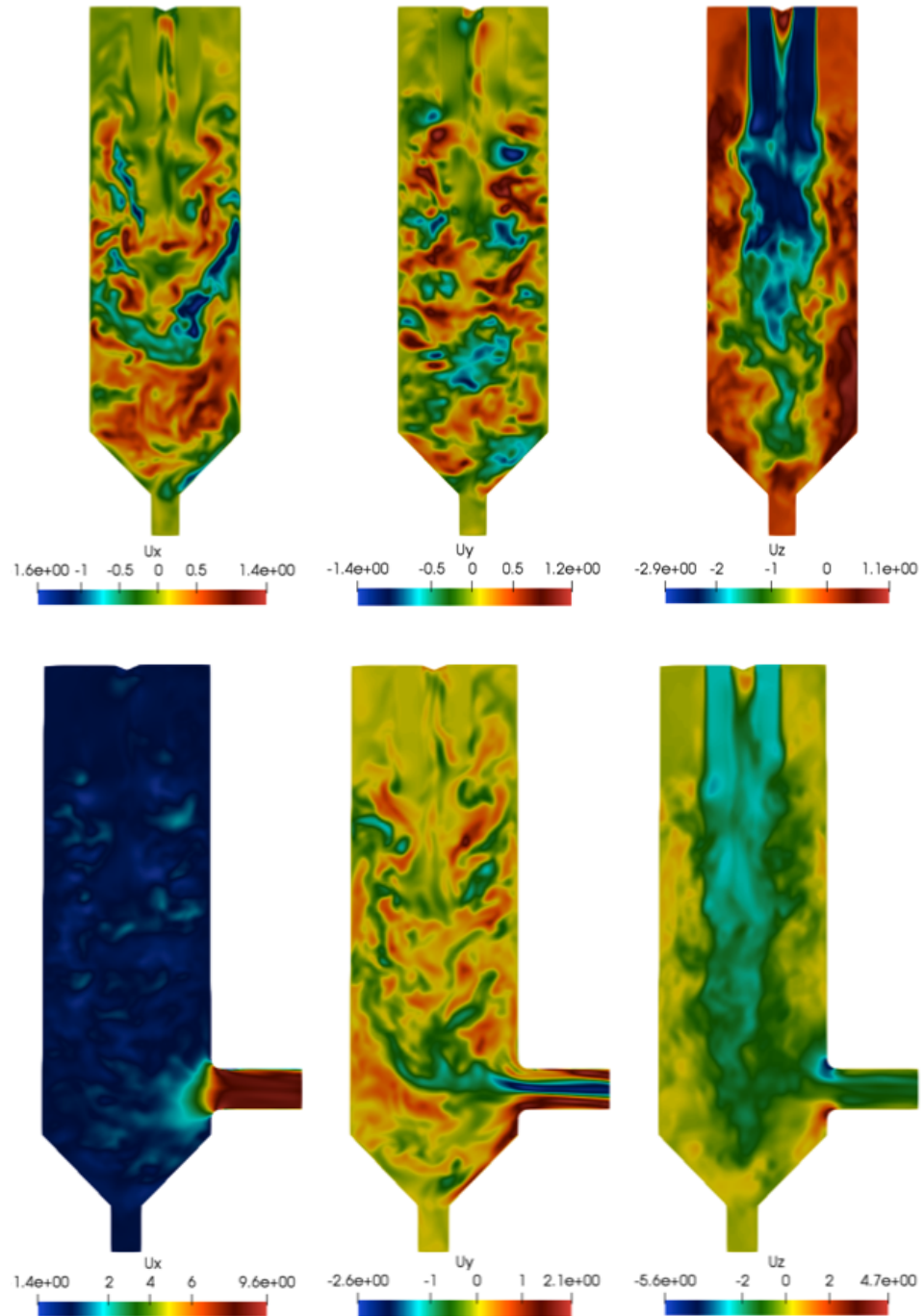


Figure 7.22: *Instantaneous velocity contours in $x-z$ and $y-z$ planes.*

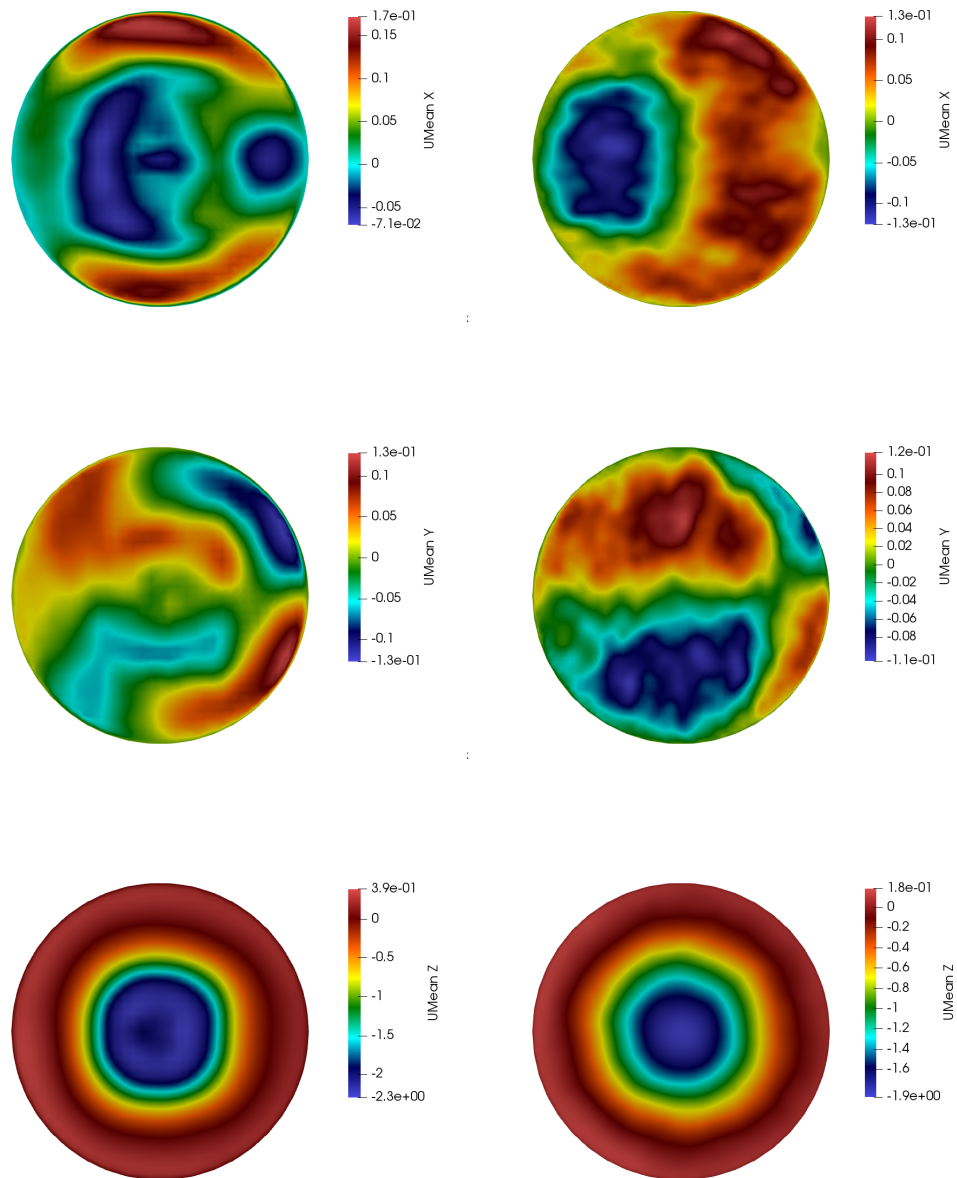


Figure 7.23: From top to bottom; U_x , U_y , U_z . Results from the coarse mesh on the left, and from the fine mesh on the right. The cross section is taken at $z = 0.3$ m.

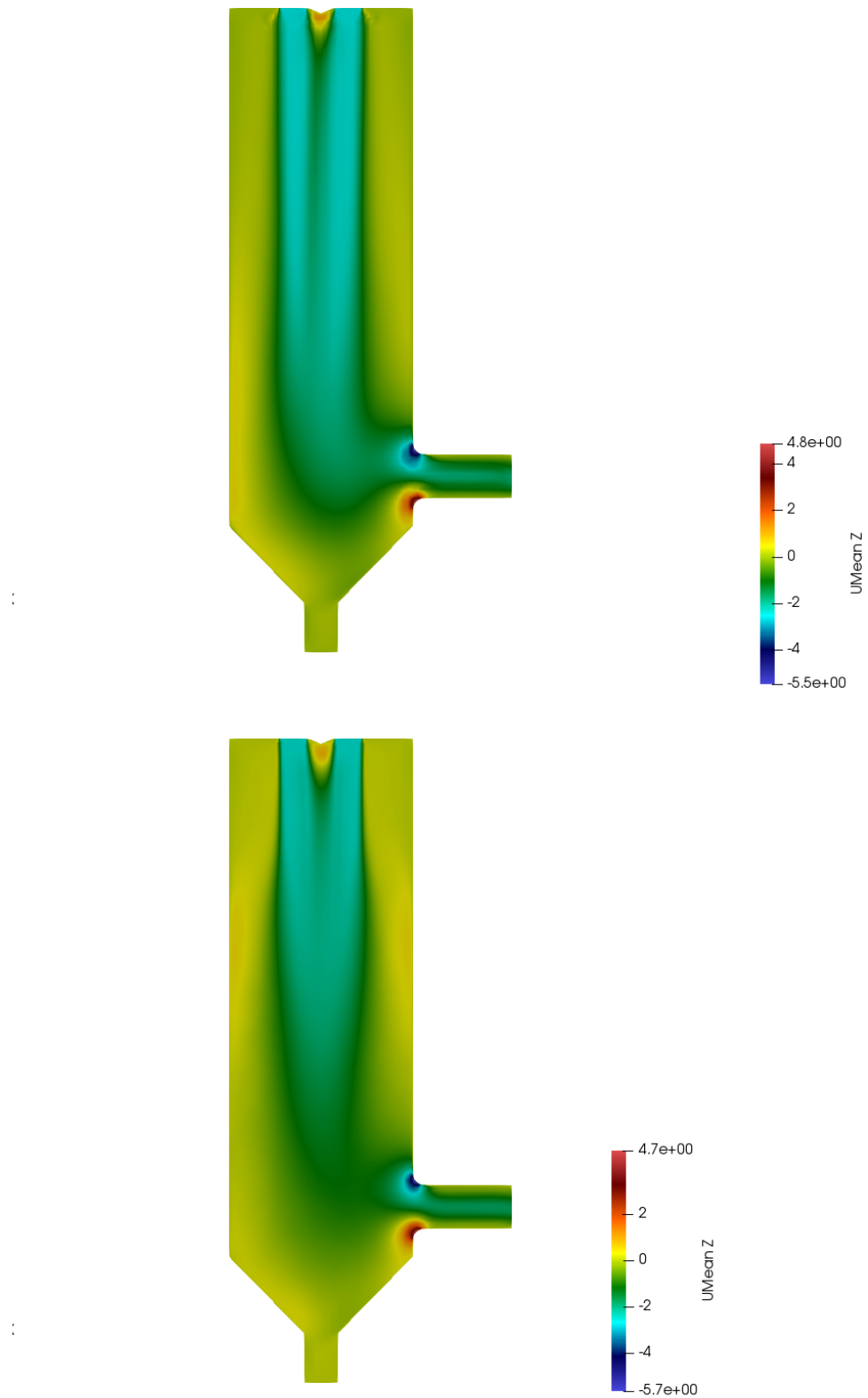


Figure 7.24: A vertical cross section of the mean value of U_z from the coarse mesh in the top and from fine mesh at the bottom.

7.3 Particle flow

The insoluble solid dispersed in droplets is the calcium carbonate (CaCO_3), while the soluble solid chosen for the solution is the maltodextrin. There are a lot of thermophysical properties for air, water and solid and some of which are not easy to extrapolate from the literature. For example, for maltodextrins one should consider the dextrose equivalence (DE), a parameter that expresses the degree of hydrolysis of starches and carbohydrates. The maltodextrins used for the experimental tests had DE 16,5-19,5 but in the literature it was possible to find the data only relative to DE 16-19,9 for the density and DE 12 for the specific heat [7] [25]. The main choices for this model are listed in Table 7.27.

To save computational time a simplified two-phase evaporation model has been used for the droplets. The main assumption in this model is that the droplet temperature is not a function of the radius and it can vary only with time. This approximation leads to the well known lumped model, and is here applied both for the first and second stage. Indeed there is no possibility to have information about the droplet centre temperature and this could be a problem for large drops for which it might exist a consistent difference.

The simulations were launched for three cases: 25g/50mL, 15g/50mL and 5g/50mL with fixed feed flow rate 5 mL/min regarding the suspension with calcium carbonate, while for the solution with maltodextrins, two simulations have been launched for the cases: 25g/50mL and 5g/50mL with feed flow rate 5 mL/min.

The volume fraction defined in chapter 3 was calculated to be $3 \cdot 10^{-6}$ meaning that we are dealing with a dilute mixture. Another important parameter that was calculated by equation 3.62 is the Stokes number that resulted < 0.35 . This means that it is reasonable to assume a one-way coupling can be assumed. Finally, a Reynolds number of 55000 was calculated by equation $\text{Re} = \text{UD}/\nu$ (where U =flow velocity [m/s], D =cylinder diameter [m] and ν =kinematic viscosity of the fluid [m^2/s]), this means that the flow is turbulent.

Table 7.27: *Input parameters for droplets used during simulations.*

Droplet	
Initial droplet diameter:	(micron)
25g/50ml	50
15g/50ml	50
5g/50ml	50
Initial droplet mass:	(grams)
25g/50ml	$8.39 \cdot 10^{-8}$
15g/50ml	$7.83 \cdot 10^{-8}$
5g/50ml	$6.96 \cdot 10^{-8}$
Initial solid content:	(mass of solid/total mass)
25g/50ml	0.33
15g/50ml	0,23
5g/50ml	0,09
Air	
Aspiration rate	$27 \text{ m}^3/\text{h}$
Temperature	433,15 K
Density	$1 \text{ Kg}/\text{m}^3$
Thermal diffusivity	$36,94 \cdot 10^{-6} \text{ m}^2/\text{s}$
Kinematic viscosity	$1 \cdot 10^{-5} \text{ m}^2/\text{s}$
Thermal conductivity	0,033 W/mK
Water	
Specific heat	4187 J/KgK
Density	$1000 \text{ Kg}/\text{m}^3$
Calcium carbonate	
Specific heat	834 J/KgK
Density	$2930 \text{ Kg}/\text{m}^3$
Maltodextrins	
Specific heat	1500 J/KgK
Density	$600 \text{ Kg}/\text{m}^3$

Case: CaCO₃ 25g/50mL, feed flow rate 5 mL/min

Here, results are presented for the case in which the feed flow rate is 5 ml/min and the concentration of CaCO₃ is 25g/50ml. The particle feed is 100000 particles per second, all having an initial diameter of 50 μm. In Figs.7.25-7.26 the particle clouds are presented at four different instants. In each sub figure the temperature, diameter and age is given for each droplet. The diameter range shown corresponds to the initial (large) and completely evaporated (small) stages. We can note at the early stage, before the particles first reach the bottom of the spray dryer, the particle cloud follow the central jet where the velocity is high. At the initial instant the diameter is fairly similar to the initial one, while already at the second instant almost all particles are completely evaporated. Further, it can be noted that the particle cloud in the central jet remains at a fairly low temperature. At the later instants the particles turn upwards following the re-circulation of the flow and their temperature increases almost to the surrounding one. Moreover, we can see that almost all particles in the cloud have diameters corresponding to the evaporated state.

In Fig.7.27 we present the trends, starting from the top, of the diameter, temperature and humidity of the particles as a function of the age. Looking at the temperature, during a short initial period (almost negligible), the drop is heated at constant diameter. When the evaporation temperature is reached the diameter starts to decrease, and does so until a critical moisture content, calculated from $X_{cr} = \frac{\rho_w \epsilon}{\rho_s(1-\epsilon)}$, is reached. At this point, the model imposes the diameter to be constant, as well as the moisture content ($X = X_{cr}$). At this point the drop is considered a solid. Then the temperature starts to increase due to convective thermal exchange with the surrounding air, until the solid gets the temperature of the surrounding air. In this case the diameter reached and which remains constant is 30 μm.

The graph reported in Fig.7.28 shows the mass injected over time (blue line) which, by definition, is a linear function; the mass present in the system (red line) and the output mass (black line), after a certain instant, have a linear tendency. The difference between the injected mass and the sum of the other two gives the quantity of evaporated mass.

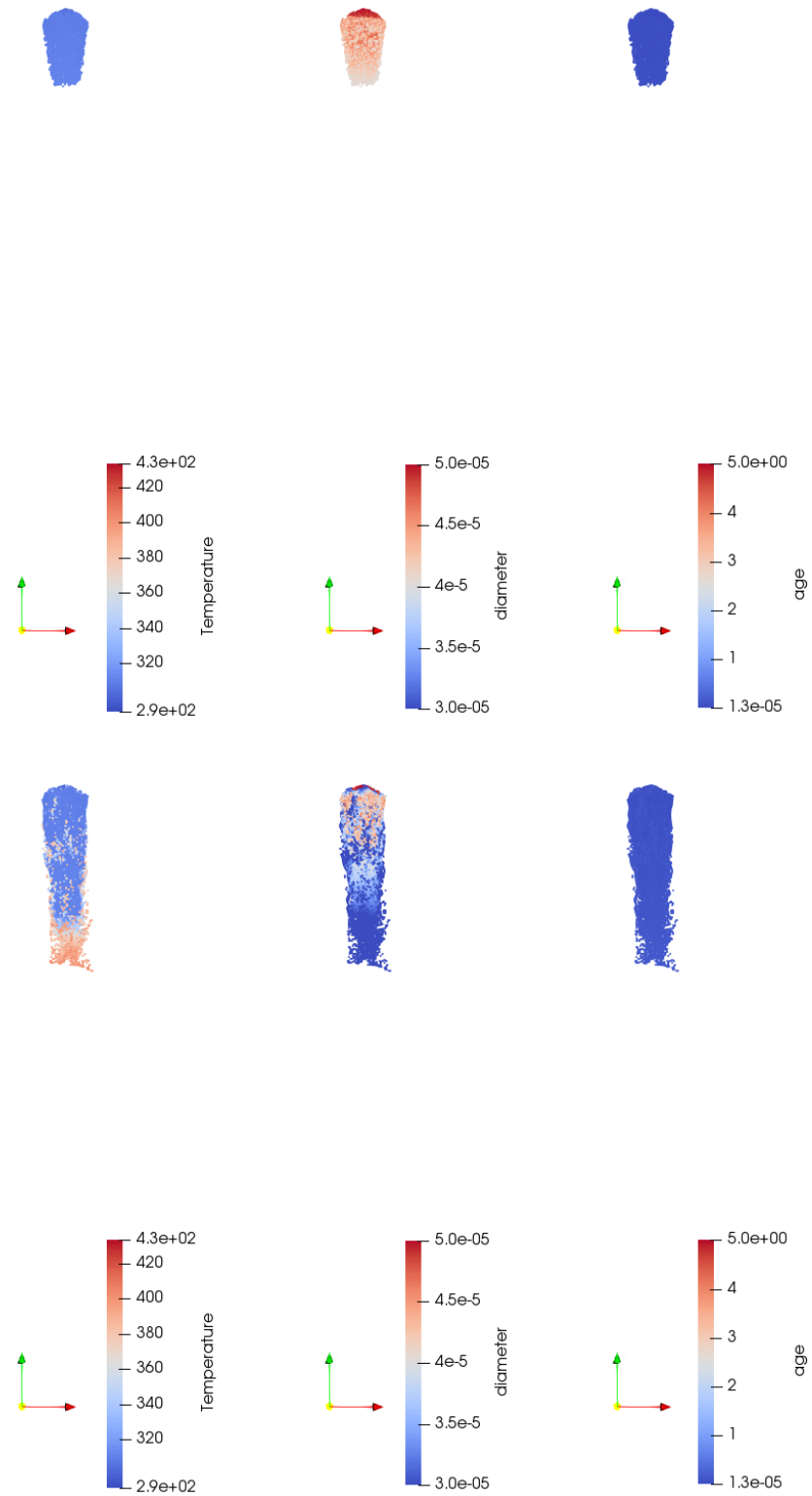


Figure 7.25: Variation of the temperature, diameter and age of the particles respectively, at $t = 0.06, 0.16$ seconds.

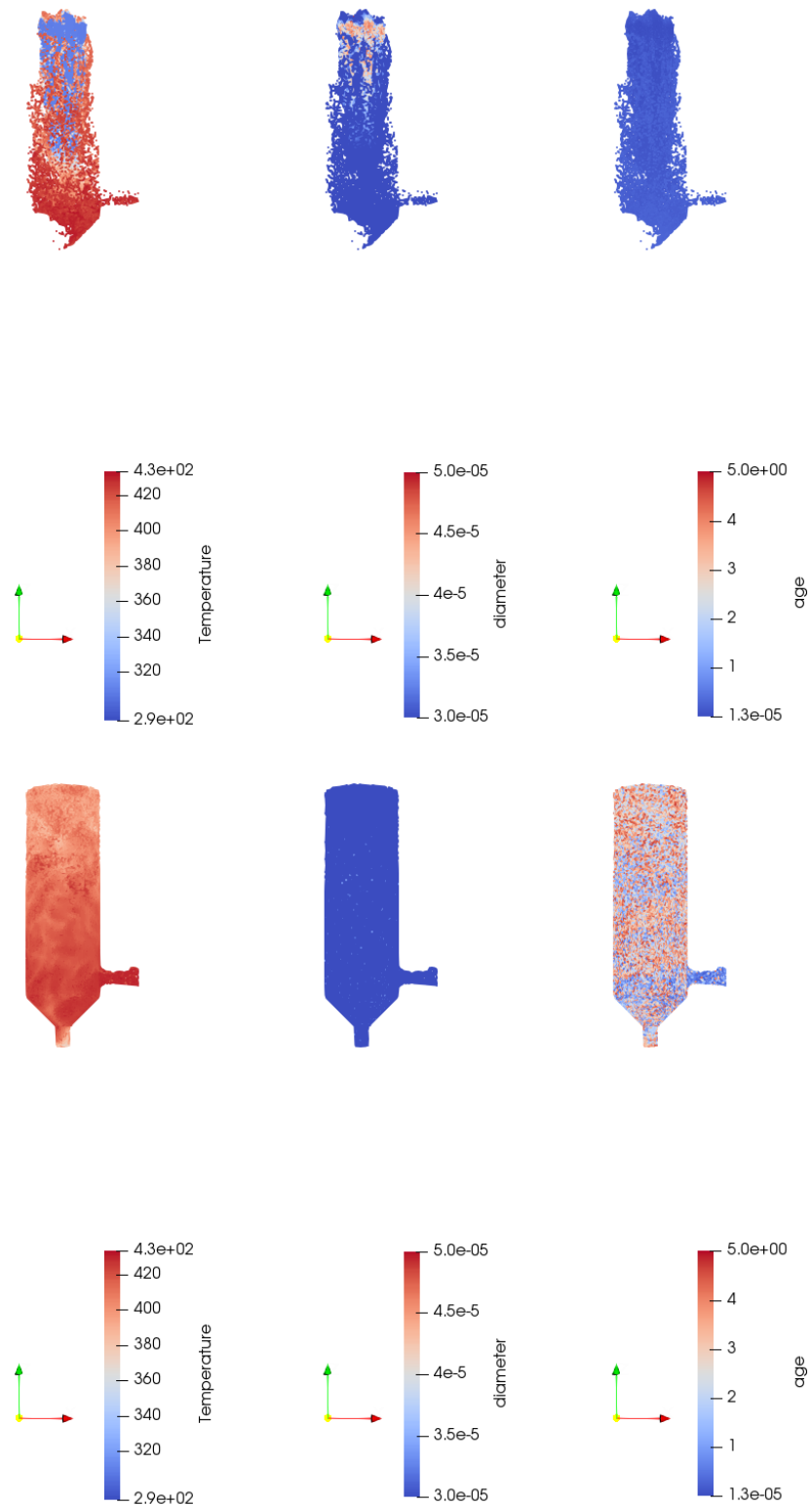


Figure 7.26: Variation of the temperature, diameter and age of the particles respectively, at $t = 0.3, 4.7$ seconds.

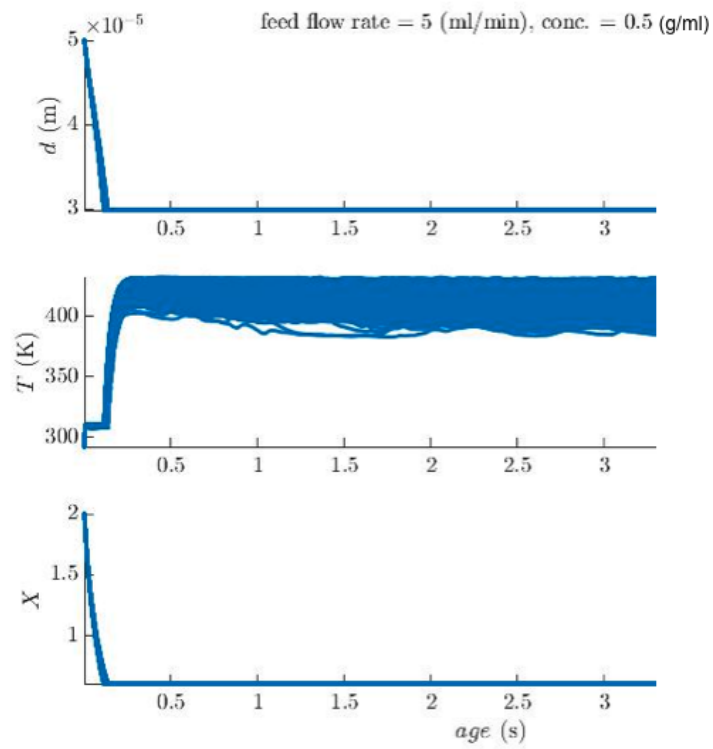


Figure 7.27: Trends of the diameter, temperature and humidity of the particles according to age, starting from the top for the case: calcium carbonate 25g/50ml.

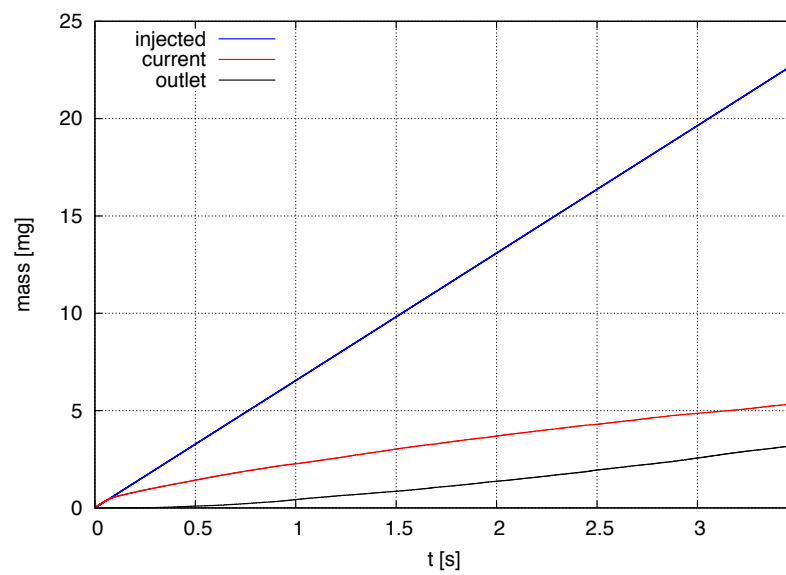


Figure 7.28: mass VS time for calcium carbonate 25g.

Case: CaCO₃ 15g/50mL, feed flow rate 5 mL/min

Here, results are presented for the case in which the concentration of CaCO₃ is 15g/50ml and feed flow rate is always 5 ml/min. The particle feed is 100000 particles per second, all having an initial diameter of 50 μm .

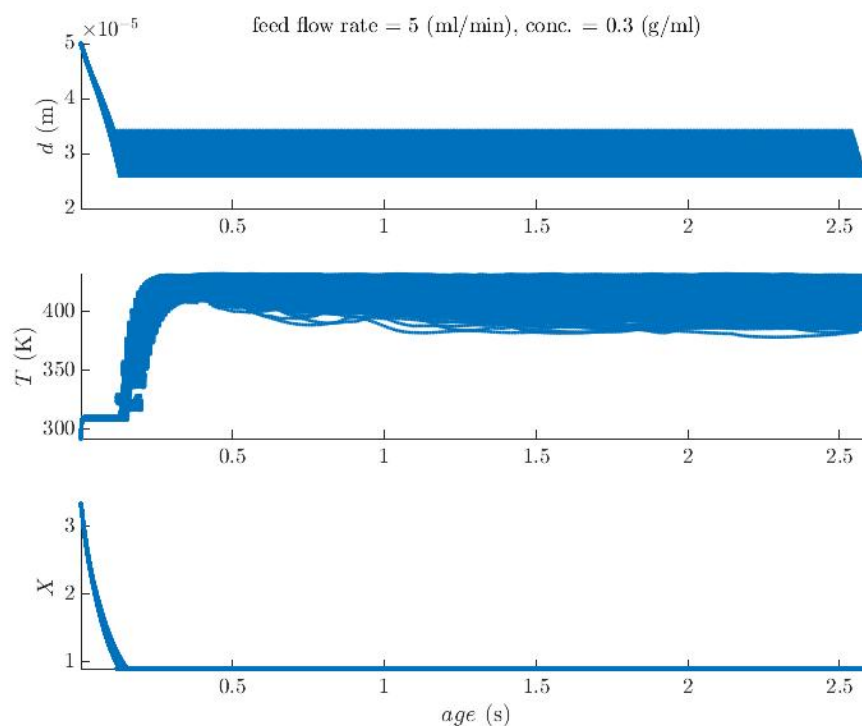


Figure 7.29: Trends of the diameter, temperature and humidity of the particles according to age, starting from the top for the case: calcium carbonate 15g/50ml.

In Fig.7.29 the trends, starting from the top, of the diameter, temperature and humidity of the particles as a function of the age are reported. Also in this case, looking at the temperature, the initial period, in which the drop is heated at constant diameter, is short. When the evaporation temperature is reached the diameter starts to decrease, and it can be seen that it reaches a value that oscillates around 30 μm .

In the graph reported in Fig.7.30 it can be seen that, having a lower solid concentration, with the same feed flow rate, the quantity of injected mass is obviously less than the case with 25g/50ml.

Case: CaCO₃ 5g/50mL, feed flow rate 5 mL/min

Here, results are presented for the case in which the concentration of CaCO₃ is 5g/50ml and feed flow rate is always 5 ml/min. The particle feed is 100000 particles per second, all having an initial diameter of 50 μm .

In Fig.7.31 we present the trends, starting from the top, of the diameter, temperature and humidity of the particles as a function of the age. In this case, the diameter starting from the usual 50 μm reaches a diameter of about 20 μm which corresponds to the achievement of the critical moisture content for which it is then kept constant.

In Fig.7.32 it is possible to see that the mass present in the chamber goes to saturation. In this case the evaporated mass is much greater than the two cases described above.

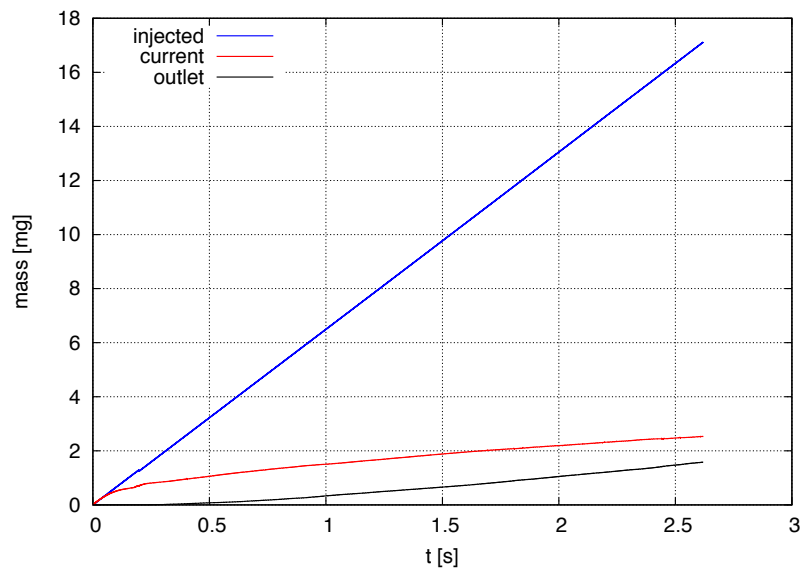


Figure 7.30: *mass VS time for calcium carbonate 15g.*

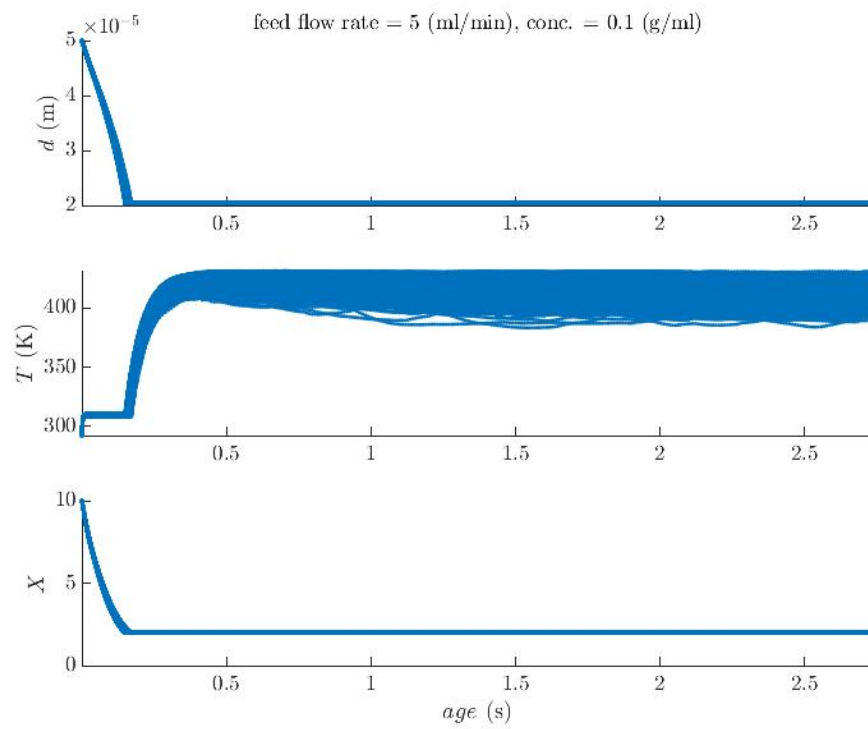


Figure 7.31: Trends of the diameter, temperature and humidity of the particles according to age, starting from the top for the case: calcium carbonate 5g/50ml.

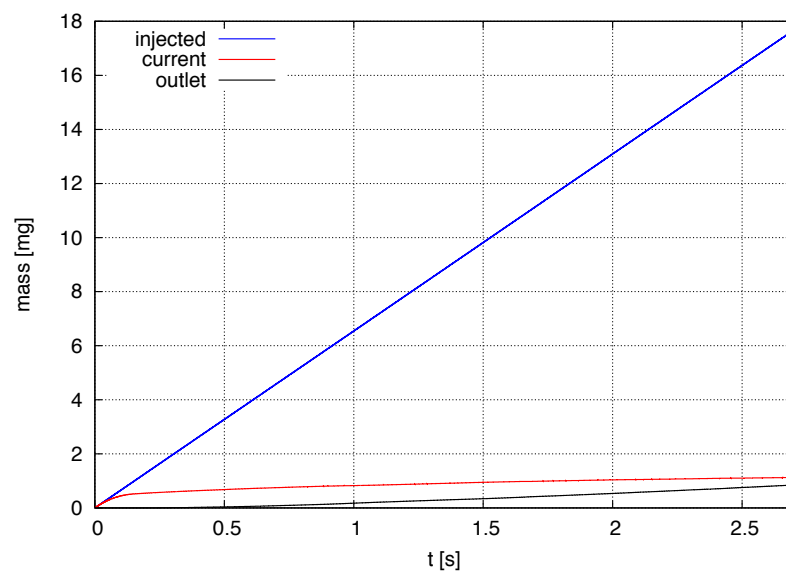


Figure 7.32: mass VS time for calcium carbonate 5g.

Case: Maltodextrins 25g/50mL, feed flow rate 5 mL/min

Here, results are presented for the case in which the concentration of Maltodextrins is 25g/50ml and feed flow rate is, also in this case, 5 ml/min. The particle feed is 100000 particles per second, all having an initial diameter of 50 μm .

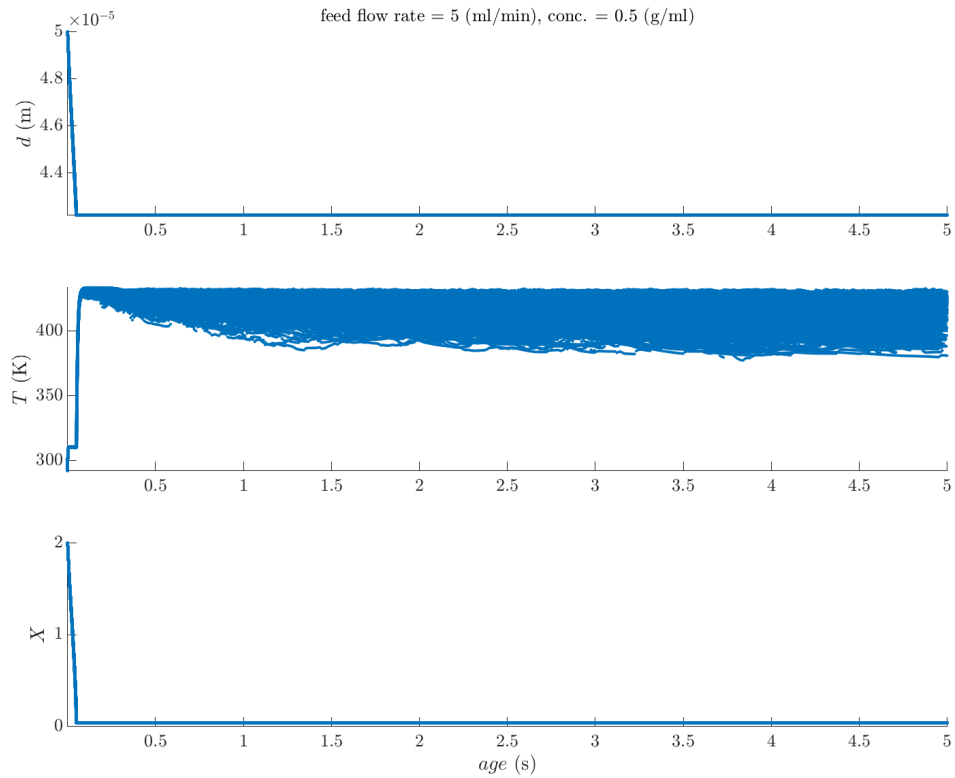


Figure 7.33: Trends of the diameter, temperature and humidity of the particles according to age, starting from the top for the case: maltodextrin 25g/50ml.

Fig.7.33 shows that the diameter decreases rapidly to a value of 40 μm that corresponds to the critical moisture content. In Fig.7.34 it can be seen that the current mass in the system goes to saturation, then, after a certain period of time it tends to a constant value.

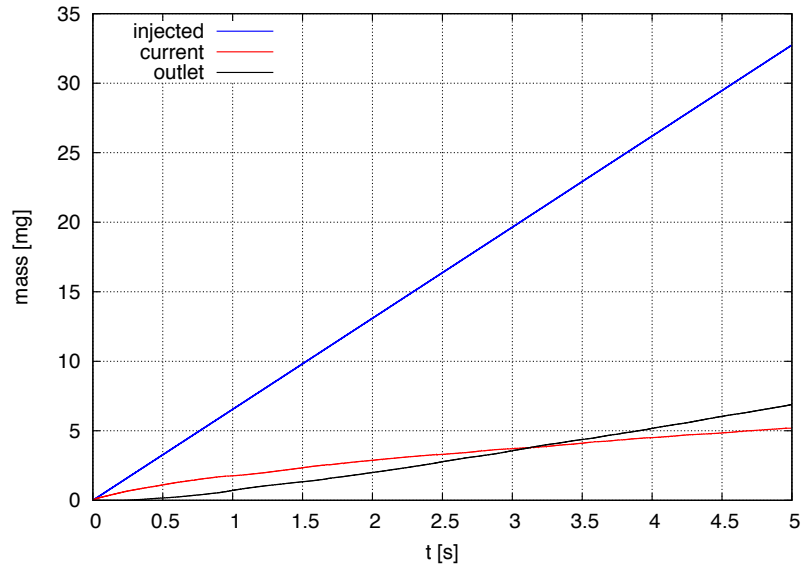


Figure 7.34: *mass VS time for maltodextrins 25g.*

Case: Maltodextrins 5g/50mL, feed flow rate 5 mL/min

Here, results are presented for the case in which the concentration of Maltodextrins is 5g/50ml and feed flow rate is 5 ml/min. The particle feed is 100000 particles per second, all having an initial diameter of 50 μm .

In Fig.7.35 it can be seen that, the diameter reached, has a value less than 40 μm . Fig.7.41 shows that the current mass is starting to tend to a constant value and, then, to reach saturation condition.

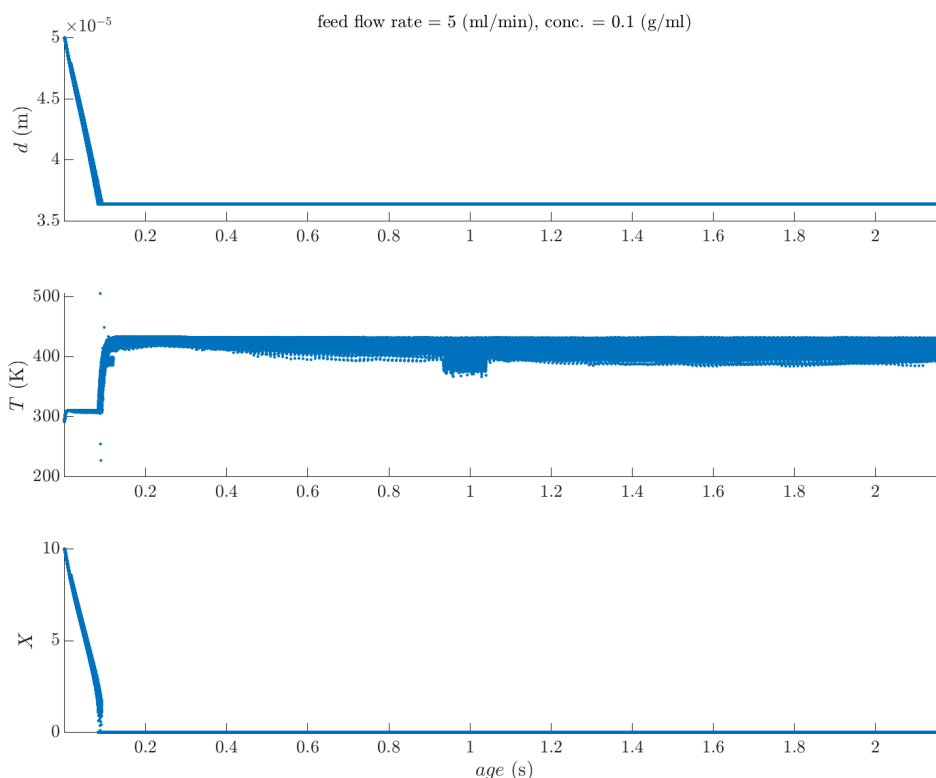


Figure 7.35: Trends of the diameter, temperature and humidity of the particles according to age, starting from the top for the case: maltodextrin 5g/50ml.

7.4 Comparison with experimental data

As regards the comparison between the experimental data and those of the simulations, some consideration must first be made. First of all a laboratory test takes about 10 minutes, the value of the product recovery that is experimentally obtained (see Tables 7.23 and 7.25) is therefore linked to this time interval. The simulations have been launched for about 5 seconds, therefore, the experimental data we have is an approximation given the difference in the duration of the process. To make a comparison we decided to express the product recovery as mass obtained per second (Kg/sec). Moreover, there is not the same feed flow rate because, in the laboratory tests, the number of particles injected can be calculated as the feed flow rate, which is 5ml/min, divided by the initial drop volume, for which the diameter is known to be $50\mu\text{m}$. The resulting number of particles, assuming that they are all of the same size, in the experiment is 1272200 particles per second, while for the simu-

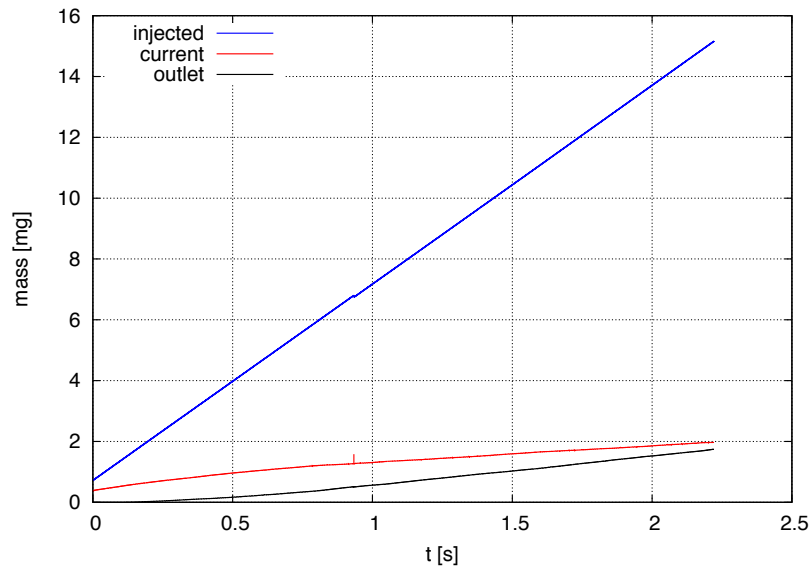


Figure 7.36: *mass VS time for maltodextrins 5g.*

lations we have set 100000 particles per second. The approximation made for the comparison is the following: if the yield with 100000 particles is a certain value, if the number of drops injected increases, the yield per second will increase linearly. At this point the yield from the numerical simulation is multiplied with the ratio, $1272200/100000=12.722$. Furthermore, it is also necessary to distinguish the cases in which calcium carbonate was used from those for which maltodextrins were used. For calcium, the yield shown in the red curve in Figs.7.37-7.38-7.39 is greater than the experimental value, so we can deduce that our linear approximation is perhaps exaggerated, but we are sure of the carbonate density value, while for maltodextrins we do not have a real solid but a porous shell and it is difficult to know what is the right density, if we had an exact value maybe the two curves (Figs.7.40-7.41) could also fit together. Finally, the experimental tests concerning the measurement of the average diameter of the particles are affected by uncertainty. Not knowing, at the beginning of the work, that the initial diameter of the carbonate is about $5 \mu\text{m}$, we chose, based on the data found in the literature, a value of $50 \mu\text{m}$ for the diameter of the drops. Once this data was known it was clear that we could have chosen a drop diameter lower than that used to bring us closer to the real conditions. To conclude,

the one on which we can rely on this stage of work is that we can see that the order of magnitude is the same, therefore, notwithstanding all the approximations, we can say that we are on the right way.

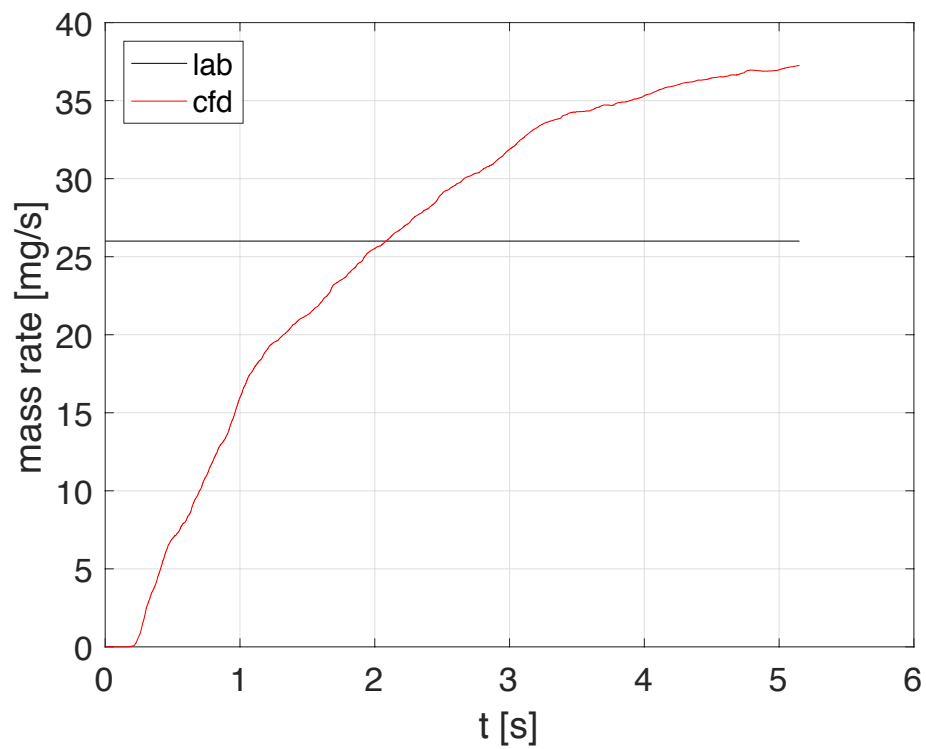


Figure 7.37: *mass VS time for calcium carbonate 25g.*

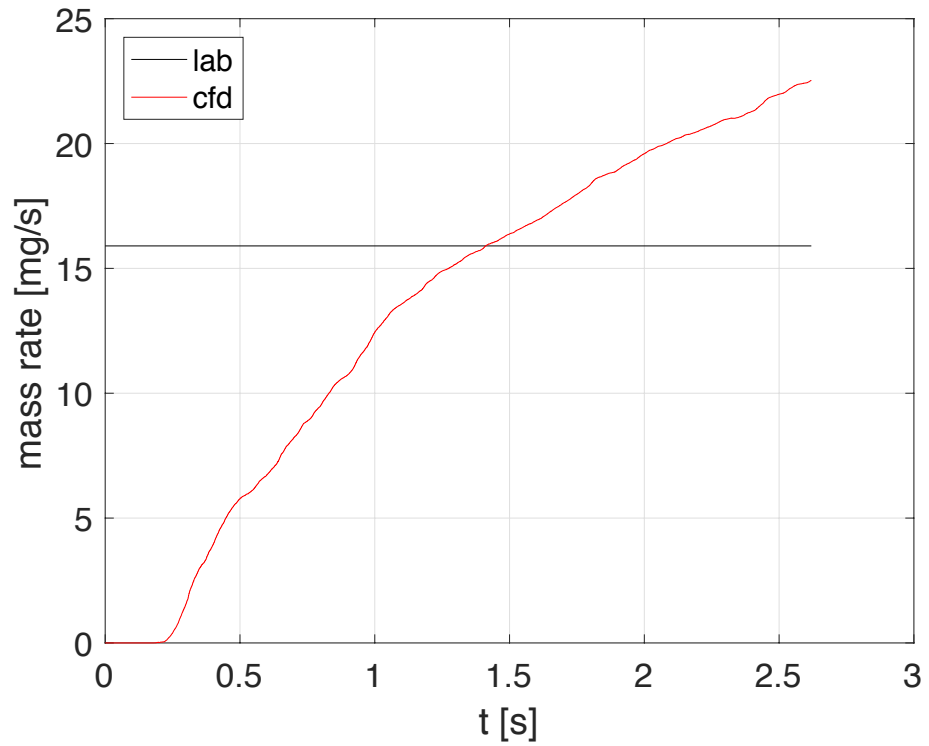


Figure 7.38: mass VS time for calcium carbonate 15g.

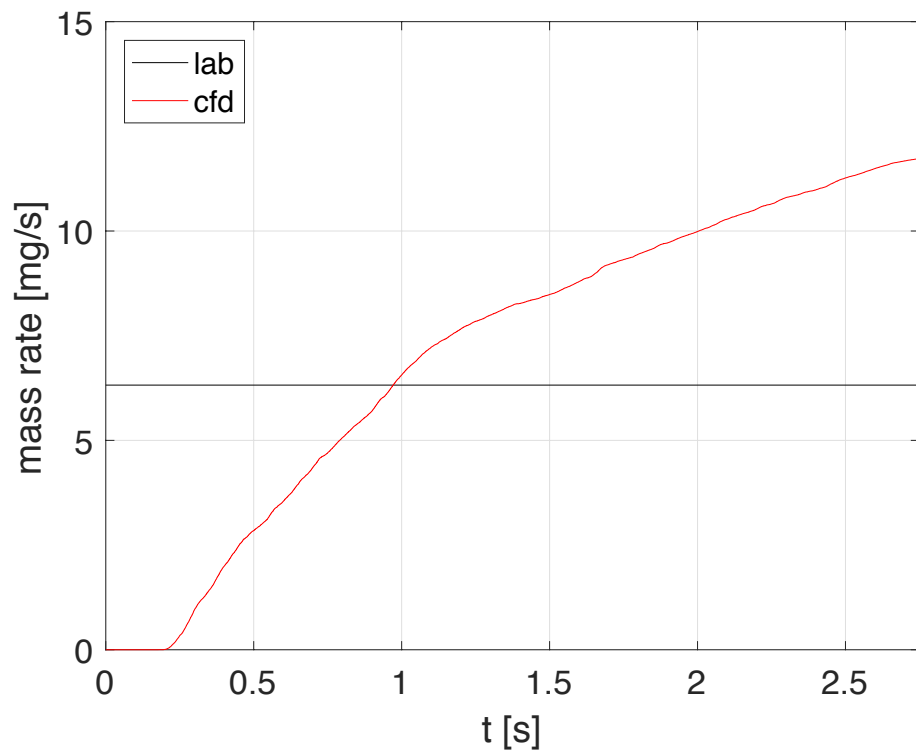


Figure 7.39: mass VS time for calcium carbonate 5g.

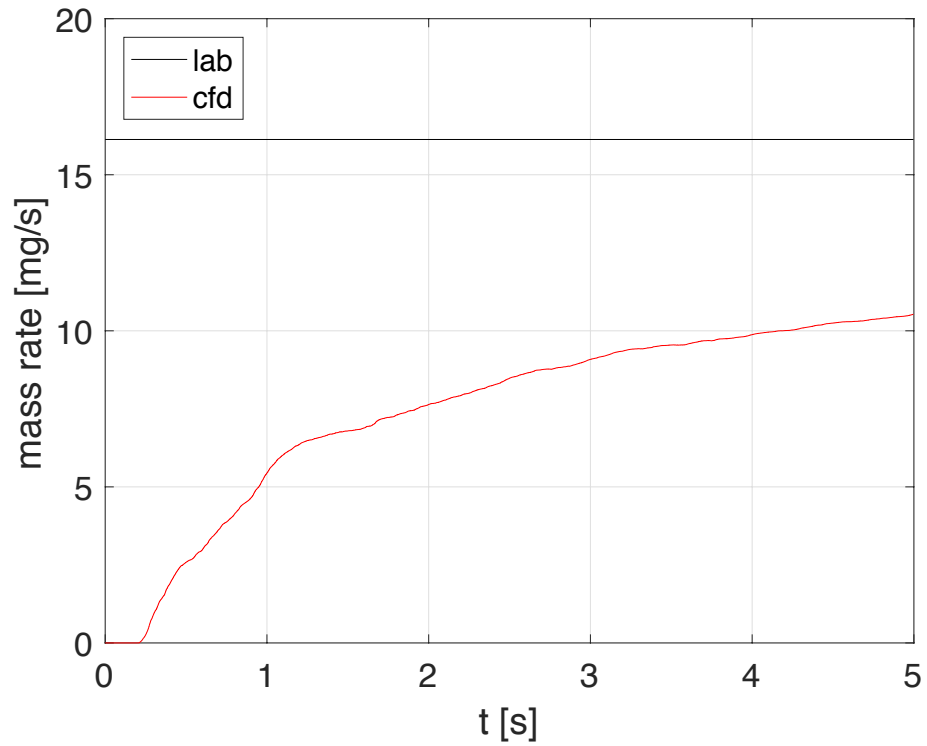


Figure 7.40: *mass VS time for calcium maltodextrins 25g.*

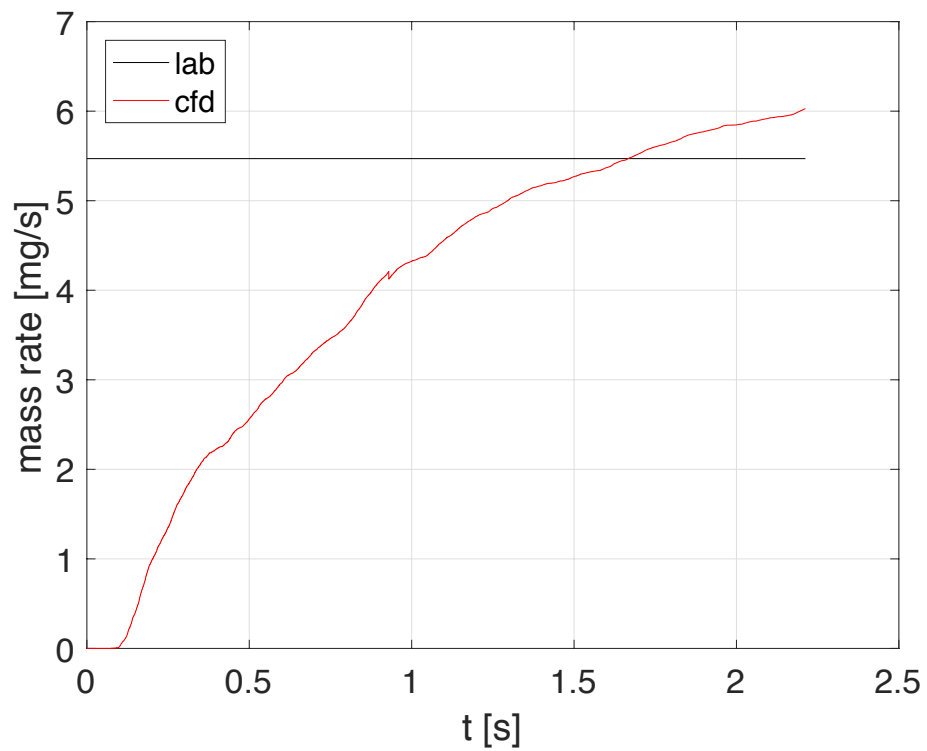


Figure 7.41: *mass VS time for calcium maltodextrins 5g.*

Conclusions and Future Developments

During this thesis a two stage drying model for droplets containing insoluble solids and soluble solid has been used. The specific cases of concentration and feed flow rate, used as parameters in the simulations, was treated because of the possibility of an experimental data comparison.

The first part of the results concerns the statistical analysis of the experimental data initially obtained in the laboratory, to assess which are the parameters that most influence the spray drying process and find optimal sets of input variables to maximize the yield, i.e. the recovery of product. The most significant parameters were found to be the concentration of the solid and the feed flow rate. From this analysis a new set of experiments was obtained, testing three values of the two most significant parameters for a total of 9 combinations. The tests, in this second part of the work, were carried out both with the maltodextrins solution in water and with the suspension of calcium carbonate in water.

Once the experimental data were obtained, these were used for CFD simulations. Some dimensions could not be obtained directly from the spray dryer, so we had to make approximations based on the data found in the literature. In particular the parameters relating to the size of the drops that are atomized in the chamber, consequently, the number of drops injected per second (that depends on the diameter). Furthermore, the inlet air velocity could not be experimentally obtained. Moreover, as regards the simulations with maltodextrins, there is a great uncertainty about the density value used, due to the lack of data in the literature, and this has definitely negatively affected the results obtained.

The work done with this thesis is an important step forward compared to the work that had been done until now because, for the first time, the model used was adapted to the geometry of the spray dryer used in the laboratory of the University of Genoa.

From the experimental tests it was not possible to understand exactly what happened inside the chamber, i.e. with which trajectories the particles moved, if there were re-circulation, accumulation in certain areas of the chamber, while thanks to the results of the simulations we could see in detail the behavior of the particles.

The comparison between the experimental data and the simulations was made possible in terms of mass of solid output per second. Despite these approximations, the results of the simulations satisfactorily describe the spray drying process.

Further developments will certainly be necessary, especially regarding the study of the true diameter of the injected drops, now that it is known how much the diameter of the initial solid is. Moreover, it would be useful to investigate the real density of the maltodextrin recovered from the spraydryer. Finally, it will certainly be right to carry out a study by setting, in the simulations, a number of drops injected per second much greater than that used in this work, to see how the yield varies with the injection.

Bibliography

- [1] Web page. www.wolfdynamics.com.
- [2] Web page. <https://cfd.direct/>.
- [3] C. Anandharamakrishnan. Experimental and computational fluid dynamics studies on spray-freeze-drying and spray-drying of proteins, 2008.
- [4] C. Anandharamakrishnan. Computational fluid dynamics applications in food processing. *SpringerBriefs in Food, Health, and Nutrition*, 2013.
- [5] Giovanni Beati. Implementation of a two-stage drying model for liquid drops containing insoluble solids in openfoam for spray drying applications, 2017.
- [6] Rinil Kuriakose C. Anandharamakrishnan. Computational fluid dynamics (cfd) applications in spray drying of food products. *Trends in Food Science & Technology*, 21:383–398, 2010.
- [7] C. Y. Takeiti, T. G. Kieckbusch and F. P. Collares-Queiroz. Morphological and Physicochemical Characterization of Commercial Maltodextrins with Different Degrees of Dextrose-Equivalent. *International Journal of Food Properties*, 13:2:411–425, 2010.
- [8] Valeria Caia. “utilizzo della tecnica di spray drying per migliorare la solubilita di una bevanda a base di cacao”, November 2014.
- [9] C.D. Argyropoulos and N.C. Markatos. *Recent advances on the numerical modelling of turbulent flows. Applied Mathematical Modelling*, 39:693–732, 2015.
- [10] Y. Cengel. *Heat transfer, A pratical approach*. Mcgraw-Hill, 2004.

- [11] <https://cfd.direct/openfoam/user-guide/> Christopher J. Greenshields. *OpenFOAM User Guide*.
- [12] Clayton T. Crowe. *Multiphase flow handbook*. CRC Press, Taylor & Francis Group, 2006.
- [13] T. A. G. Langrish D. J. E. Harvie and D. F. Fletcher. A computational fluid dynamics study of a tall-form spray dryer. *IChemE*, 80, September 2002.
- [14] D. K. Lilly. *The representation of small-scales turbulence in numerical simulation experiments*. National Center for Atmospheric Research, 1966.
- [15] Irene Borde David Levi-Hevroni, Avi Levy. Mathematical modelling of drying of liquid solid slurries in steady state one-dimensional flow. *Drying Technology*, 13:1187–1201, 1995.
- [16] D.J.E. Harvie T.A.G. Langrish J.J. Nijdam D.F. Fletcher, B. Guo and J. Williams. What is important in the simulation of spray dryer performance and how do current cfd models perform? *Applied Mathematical Modelling*, 30:1281–1292, 2006.
- [17] S. E. Elghobashi. On predicting particle-laden turbulent flows. *Applied Scientific Research*, 52:309–329, 1994.
- [18] GEA Process Engineering. *GEA Niro spray drying. Small-scale solutions for RD and production*.
- [19] M. Darwish F. Moukalled, L. Mangani. *The Finite Volume Method in Computational Fluid Dynamics, An Advanced Introduction with OPENFOAM[®] and MATLAB[®]*. Springer, 2016.
- [20] P. J. Fellows. *"Food processing technology-Principles and practice"*. Woodhead Publishing Limited, Cambridge, 1998.
- [21] J. H. Ferziger and M. Perić. *Computational Methods for Fluid Dynamics*. Springer, third edition edition, 2002.

- [22] J. Smagorinsky. *General circulation experiments with the primitive equations. Monthly Weather Review*, 91, 1963.
- [23] K. Masters. *Spray drying handbook*, volume fourth edition. 1985.
- [24] F.G. Kieviet. *Modelling quality in spray drying*, 1997.
- [25] Klaus Schittkowski. *Modeling of Maltodextrin DE12 Drying Process in a Convection Oven*. Dept. of Mathematics, University of Bayreuth, 1999.
- [26] T.A.G. Langrish and D.F. Fletcher. Spray drying of food ingredients and applications of cfd in spray drying. *Chemical Engineering and Processing*, 40:345–354, 2001.
- [27] E. Loth. Numerical approaches for motion of dispersed particles, droplets and bubbles. *Progress in Energy and Combustion Science*, 26(3):161–223, 2000.
- [28] P.J. Heggs M.Ghadiri V.F. Gracia A. Bayly D. Djurdjevic H. Ahamadian M. Ali, T. Mahmud and L. Martin de Juan. Cfd modelling of a counter-current spray drying tower. *8 International Conference on Multiphase Flow*, pages 26–31, May 2013.
- [29] M. L. Shur, P. R. Spalart, M. K. Strelets and A. K. Travin. *A hybrid RANS-LES approach with the delayed-DES and wall-modelled LES capabilities. International Journal of Heat and Fluid Flow*, 29:1638–1649, 2008.
- [30] I. Borde M. Mezhericher, A. Levy. Theoretical drying model of single droplets containing insoluble or dissolved solids. *Drying Technology*, 25(6):1035–1042, 2007.
- [31] I. Borde M. Mezhericher, A. Levy. Heat and mass transfer of single droplet/wet particle drying. *Chemical Engineering and Processing*, 63:12–23, 2008.
- [32] I. Borde M. Mezhericher, A. Levy. Modelling of particle breakage during drying. *Chemical Engineering and Processing*, 47:1404–1411, 2008.

- [33] Avi Levy Maksim Mezhericher and Irene Borde. Three-dimensional spray-drying model based on comprehensive formulation of drying kinetics. *Drying Technology: An International Journal*, 30:11–12:1256–1273,, 2012.
- [34] M. Mezhericher. Drying of slurries in spray dryers, September 2008.
- [35] Peter John Heggasa Mojtaba Ghadiria Andrew Baylya Hossein Ahmadianb Muzammil Alia, Tariq Mahmuda and Luis Martin de Juan. Cfd simulation of a counter-current spray drying tower with stochastic treatment of particle-wall collision. *Procedia Engineering*, 102:1284–1294, 2015.
- [36] M. Necati Ozisik. *Heat conduction*. John Wiley Sons, 1993.
- [37] P. R. Spalart and S. R. Allmaras. *A one-equation turbulence model for aerodynamic flows*. *30th AIAA Aerospace Sciences Meeting and Exhibit*, 1992.
- [38] P. R. Spalart, S. Deck, M. L. Shur, K. D. Squires, M. Kh. Strelets and A. Travin. *A new version of detached-eddy simulation, resistant to ambiguous grid density*. *Theoretical Computation Fluid Dynamics*, 20:181–195, 2006.
- [39] P. R. Spalart, W-H. Jou, M. Strelets and S. R. Allmaras. *Comments of feasibility of LES for wings, and on a hybrid RANS/LES approach*. *International Conference on DNS/LES, 1997, Ruston, Louisiana*, 1997.
- [40] Berger L. Razilov I. Schaldach, G. and Berndt H. Computer simulation for fundamental studies and optimisation of icp spray chambers, 2000.
- [41] Shayantharan Sivaramalingam. Modelling and control of a spray drying process, November 2009.
- [42] Stephen B. Pope. *Turbulent Flows*. Cambridge University Press, 2000.
- [43] Stephen B. Pope. *Ten questions concernin the large-eddy simulation of turbulent flows*. *New Journal of Physics*, 6, 2004.
- [44] H. Tennekes and J. L. Lumley. *A first course in turbulence*. MIT Press, 1972.

- [45] Thomas B. Gatski, M. Yousuff Hussaini and John L. Lumley. *Simulation and Modeling of Turbulent Flows*. Oxford University Press, 1996.
- [46] Uriel Frish. *Turbulence*. Cambridge University Press, 1995.
- [47] <http://cfd.direct/openfoam/user-guide/thermophysical/>. *OpenFOAM User Guide: 7.1: Thermophysical models*.
- [48] David C. Wilcox. *Turbulence modelling for CFD*. DCW Industries, 2006.
- [49] Huang L.X. Mujumdar A.S. Daud W.R.W. Woo, M.W. *CFD simulation of spray dryers*. 2010.